



DISSERTATION

# Assessing Vegetation Dynamics from Spaceborne Active Microwave Backscatter Observations

Ausgeführt zum Zwecke der Erlangung des akademischen Grades eines

**Doktorin der Naturwissenschaften**

unter der Leitung von

Univ.Prof. Dipl.-Ing. Dr.techn. Wolfgang Wagner  
Department für Geodäsie und Geoinformation  
Forschungsgruppen Photogrammetrie und Fernerkundung

eingereicht an der Technischen Universität Wien  
Fakultät für Mathematik und Geoinformation

von

**Mariette Vreugdenhil M.Sc.**

Matrikelnummer 1228883  
Alserbachstrasse 15/13  
A-1090, Wien  
Österreich

Wien, am October 23, 2016

.....





VIENNA UNIVERSITY OF TECHNOLOGY  
DEPARTMENT FOR GEODESY  
AND GEOINFORMATION  
RESEARCH GROUPS  
PHOTOGRAMMETRY & REMOTE SENSING



Vienna Doctoral Programme on  
**Water Resource Systems**

DISSERTATION

# **Assessing Vegetation Dynamics from Spaceborne Active Microwave Backscatter Observations**

A thesis submitted in fulfilment of the academic degree of

## **Doctor of Natural Sciences**

under the supervision of

Prof.Dr. Wolfgang Wagner  
Department of Geodesy and Geoinformation  
Research Group Remote Sensing and Photogrammetry

Research conducted at TU Wien  
Faculty of Mathematics and Geoinformation

by

## **Mariette Vreugdenhil M.Sc.**

Student number 1228883  
Alserbachstrasse 15/13  
A-1090, Vienna  
Austria

Vienna, October 23, 2016

.....

Gutachter: Univ.Prof. Dipl.-Ing. Dr. techn. Wolfgang Wagner  
 Institut für Geodäsie und Geoinformation  
 TU Wien  
 Gusshausstrasse 27-29, A-1040, Vienna .....

Gutachter: Univ.Prof. Dipl.-Ing. Dr. techn. Günter Blöschl  
 Institut für Wasserbau und Ingenieurhydrologie  
 TU Wien  
 Karlsplatz 13, A-1040, Vienna .....

Gutachter: Prof. Dr. Steven de Jong  
 Department of Geosciences  
 Utrecht University  
 Heidelbergstraat 2, NL-3584CS, Utrecht .....

Co-Supervisor: Dr. Wouter Dorigo  
 Institut für Geodäsie und Geoinformation  
 TU Wien  
 Gusshausstrasse 27-29, A-1040, Vienna

**Parts of the present work have been accepted or published in peer-reviewed journals:**

**Vreugdenhil, M.**, W. A. Dorigo, W. Wagner, R. A. M. de Jeu, S. Hahn, and M. J. E. van Marle (2016). Analyzing the Vegetation Parameterization in the TU-Wien ASCAT Soil Moisture Retrieval. *IEEE Transactions on Geoscience and Remote Sensing* 54(6): 3513–31. doi:10.1109/TGRS.2016.2519842.

**Vreugdenhil, M.**, S. Hahn, T. Melzer, B. Bauer-Marschallinger, C. Reimer, W. A. Dorigo and W. Wagner (2016). Assessing Vegetation Dynamics over Mainland Australia using Metop ASCAT. Accepted in *IEEE Journal on Selected Topics in Earth Observation and Remote Sensing*.

**Vreugdenhil, M.**, S. Hahn, C. Reimer, T. Melzer, W. A. Dorigo, R. Quast, R.A.M. de Jeu, R. van der Schalie, F. Greifeneder, E. Santi, C. Notarnicola, S. Paloscia and W. Wagner (2016). Inter-comparison of Vegetation Variables Derived from ASCAT, Aquarius and AMSR2 Microwave Instruments. Submitted.

**During the PhD I contributed to the following papers which were published in peer-reviewed journals and conference proceedings but are not included in this thesis:**

Blöschl, G., A. P. Blaschke, M. Broer, ..., **M. Vreugdenhil**, W. Wagner and M. Zessner (2016). The Hydrological Open Air Laboratory (HOAL) in Petzenkirchen: A Hypotheses Driven Observatory. *Hydrology & Earth System Sciences*, 20: 227-255.

Franz, T.E., A. Wahbi, **M. Vreugdenhil**, G. Weltin, L. Heng, M. Oismueller, P. Strauss, G. Dercon, D. Desilets (2016). Using Cosmic-Ray Neutron Probes to Monitor Landscape Scale Soil Water Content in Mixed Land Use Agricultural Systems. *Applied and Environmental Soil Science 2016*

**Vreugdenhil, M.**, R. A. M. de Jeu and J.P. Walker (2013). Identification of clay pans from AMSR-E Passive Microwave Observations. *International Journal of Remote Sensing* 34(14): 5201-5212.

**Vreugdenhil, M.**, W. Dorigo, M. Broer, P. Haas, A. Eder, P. Hogan, G. Bloeschl and W. Wagner (2013). Towards a high-density soil moisture network for the validation of SMAP in Petzenkirchen, Austria (2013). *Proceedings of IGARSS 2013*: 1865-1868.

Dorigo, W. A. Xaver, **M. Vreugdenhil**, A. Gruber, A. Hegiyova, A. Sanchis-Dufau, D. Zamojski, C. Cordes, W. Wagner and M. Drusch (2013). Global automated quality control of in situ soil moisture data from the International Soil Moisture Network. *Vadose Zone Journal* 12(3): -.

**The work has been conducted as part of the following research projects:**

Doctoral Programme on Water Resource Systems (DK-Plus W1219-N22) of the Austrian Science Funds FWF

ESA's Climate Change Initiative for Soil Moisture (contract 4000104814/11/I-NB)

"Use of SCA cross-polarisation information for soil moisture retrieval", funded through EUMETSAT ITT 14/208518



# Erklärung zur Verfassung der Arbeit

## Author's Statement

Hiermit erkläre ich, dass ich diese Arbeit selbstständig verfasst habe, dass ich die verwendeten Quellen und Hilfsmittel vollständig angegeben habe und dass ich die Stellen der Arbeit - einschliesslich Tabellen, Karten und Abbildungen -, die anderen Werken oder dem Internet im Wortlaut oder dem Sinn nach entnommen sind, auf jeden Fall unter Angabe der Quelle als Entlehnung kenntlich gemacht habe.

I hereby declare that I independently drafted this manuscript, that all sources and references are correctly cited, and that the respective parts of this manuscript - including tables, maps, and figures - which were included from other manuscripts or the internet either semantically or syntactically are made clearly evident in the text and all respective sources are correctly cited.

Mariette Vreugdenhil  
Alserbachstrasse 15/13  
A-1090 Wien  
Österreich

.....



## Acknowledgements

Many people deserve thanks here for supporting me during my PhD and making my time in Vienna so enjoyable. First of all, my thanks go out to Wolfgang, for his support and inspiration. I feel very lucky to have been able to complete my PhD under your supervision and with the opportunity to learn from you. I could not have wished for a better supervisor. I would also like to show my great appreciation to Wouter. Your optimism, willingness to always help and knowledge of vegetation remote sensing have helped me greatly! Also thanks to Professor Blöschl for his valuable input on soil moisture and to look at things from a different perspective than remote sensing. Richard, thank you for everything! You have inspired me throughout my studies, motivated me to pursue a PhD in remote sensing and have been there for me throughout the whole adventure! All the other contributors to the manuscripts are thanked for their contributions and discussion on the earlier versions of the manuscript. And many thanks to Steven de Jong for accepting the responsibility of evaluating my thesis.

Many people have helped me during my fieldwork in Petzenkirchen. First of all I would like to thank Markus. You made my stays in Petzenkirchen very enjoyable and you were the best companion in the field! Many many thanks to Monika for all the help in the lab and teaching me everything I needed to know. I am also very grateful to Thomas, Matthias, Silvia, Aziza and Ricarda for taking care of my samples and for the nice time I spent with you. Xandl, thank you for the nice breakfasts after a morning in the field and for all your efforts in teaching me soil physics and Mundart! And thank you, Peter, for being a great host in Petzenkirchen and for your expert knowledge on soil moisture networks!

Many thanks to all my colleagues at the remote sensing group. You made my stay at the TU lots of fun with having lunch, chats and occasionally beers! Many thanks to all of you who have helped me in the field digging holes! Special thanks go out to my two office mates, Sebastian and Thomas, for making me feel at home, letting me talk to myself during work and listen to all my chaotic stories. And I am especially grateful to Sebastian for all his help. Your knowledge of python and the algorithm has helped me at least once a week! I also want to thank all DK colleagues for the great time I had during my PhD. I enjoyed the symposia, courses and social activities. Inge, Linda, Martine en Rick, bedankt voor alle gezelligheid en Sinterklaas zal nooit meer hetzelfde zijn! Special thanks go out to Margreet for the discussions on VOD and the nice lunch breaks.

I always had a lot of support from the Netherlands and I am very grateful to have such an amazing family and great friends. Thanks to all of you I have been able to do this! Special thanks go out to my wonderful parents, my brother Tristen and Lisa, who have always supported me and visited me in every place I have worked! Thanks Quinten and Fam. van der Meer for being there for me especially during the first years of this adventure. And thank you Anouk, Isis, Inge and Laura for being the best friends I could wish for!

Last but not least, thank you José for everything. Your support and help with everything during my PhD made it possible. Luckily, you know exactly how to deal with my stress and craziness. I love you and I really couldn't have done it without you!



# Abstract

Microwave observations of the Earth's surface are sensitive to various environmental variables, including the water content in the soil and vegetation. Since vegetation and soil moisture influence the global carbon-, energy-, and hydrological cycle, their monitoring and mapping is pivotal to provide accurate input in global circulation and climate models. The advantage of microwave remote sensing, compared to well known visible near-infrared (VNIR) remote sensing, is that it is not impeded by cloud cover or dependent on solar illumination. For vegetation monitoring, optical depth ( $\tau$ ) is often used, which is an attenuation parameter in the microwave domain and is related to the water content of the vegetation. So far  $\tau$  has mainly been retrieved from passive microwave observations using radiative transfer models. However, long-term active microwave observations are available from a series of scatterometers, which were originally developed for monitoring ocean winds, making them valuable instruments for monitoring land surface parameters. Although active microwave observations are more sensitive to surface roughness and vegetation geometry, their advantage over passive microwave observations is their better spatial resolution, radiometric accuracy and independence of surface temperature. Consequently, the aim of this thesis is to retrieve  $\tau$  from backscatter observations in order to improve our understanding of vegetation dynamics.

Chapter I starts with the motivation for this research. This is followed by a paragraph describing the research questions and objectives and the thesis outline. In Chapter II an introduction to microwave theory is presented. This chapter first deals with the radar equation and scattering properties of natural media. After that follows a literature review focused on previous studies which have assessed the sensitivity of backscatter observations to vegetation dynamics and other land surface parameters.

Chapter III presents the retrieval of vegetation optical depth from Metop Advanced Scatterometer (ASCAT) backscatter observations using model parameters of the vegetation correction term within the TU Wien soil moisture retrieval algorithm. A first comparison between vegetation optical depth derived from passive microwave observations ( $\tau_p$ ) and vegetation optical depth from ASCAT ( $\tau_a$ ) is performed. Global spatial patterns of  $\tau_a$  and  $\tau_p$  are qualitatively compared to each other. A temporal comparison is performed by calculating the Spearman Rank Coefficient between climatologies of  $\tau_a$  and  $\tau_p$ . The strong spatial and temporal correspondence between  $\tau_a$  and  $\tau_p$  suggest that  $\tau_a$  is sensitive to vegetation dynamics in most regions. However, in boreal forests low mean values for  $\tau_a$  are found compared to  $\tau_p$ . A low temporal correlation is found in deserts and tropical forests, which is attributed to the low natural variability of vegetation in these regions. Furthermore, the retrieval of  $\tau_a$  enables the investigation of the effect of the vegetation parameterization in the TU Wien soil moisture retrieval algorithm. Overall, the vegetation parameterization as implemented in the TU Wien algorithm improves the soil moisture retrievals. However, in regions with high inter-annual variability in vegetation dynamics the soil moisture retrieval is degraded, most likely due to the fixed climatology of the correction term.

A comprehensive inter-comparison of vegetation products is performed and described in Chapter IV. The inter-comparison is done between  $\tau_a$  from Metop ASCAT observations, a cross-ratio (CR) from VH and VV observations from SAC-D Aquarius,  $\tau_p$  from AMSR2 observations and

Leaf Area Index (LAI) from SPOT VEGETATION. Spatial patterns of the different products are compared and all products follow the expected patterns according to land cover and climate class. Low values for  $\tau_a$  are found in high latitude boreal forests and these are attributed to low backscatter values during frozen conditions. It is suggested that these low values in  $\tau_a$  are likely to cause a bias in the TU Wien soil moisture product. A temporal comparison between the products shows that the seasonal trajectories of  $\tau_a$  are able to follow vegetation dynamics as found in LAI and  $\tau_p$ . In deciduous broadleaf forests a disparity is found between the products derived from scatterometers and the other products. This brings to light a different response of scatterometers compared to radiometers, which is possibly caused by leaf fall and the resulting double-bounce scattering. Lastly, phenological parameters, i.e. start of season (SOS) and peak of season (POS), are calculated for all products and compared with the aim to identify differences in timing. Spatial patterns of SOS and POS are tightly coupled between all products, but lags are found between the microwave and VNIR products which vary with land cover and climate. The study confirms the potential of  $\tau_a$  to monitor vegetation and phenological parameters. More importantly, it presents a first global comparison between  $\tau_a$  and cross-polarized data. The strong coupling between  $\tau_a$  and CR suggests that CR may be used in soil moisture retrieval algorithms to improve vegetation parameterization.

One of the disadvantages of the  $\tau_a$  retrieval was that it is only available as a seasonal product, i.e. 366 values. However, the estimation of the model parameters within the TU Wien soil moisture retrieval algorithm has been improved in a way that  $\tau_a$  can now be calculated for every day. Chapter V investigates if the time series of  $\tau_a$ , and subsequently the TU Wien vegetation correction term, are also sensitive to vegetation dynamics by comparing them to LAI. Furthermore, the ability of  $\tau_a$  to reproduce inter-annual variability in vegetation dynamics is assessed. Time series of  $\tau_a$  are retrieved over Mainland Australia for the period 2007 - 2014. This period contains years with distinct climatic conditions, including the Millennium Drought (2000 - 2009), and two years with large amounts of rainfall as a result of a change in climate modes, due mainly to the El Niño Southern Oscillation. It is found that  $\tau_a$  and LAI are tightly coupled, especially over sparsely vegetated regions and grasslands. Over croplands they start to deviate, which is a result of a lag between the two products. In deciduous broadleaf forests negative correlations between the two products are found, as is also found in the previous two chapters, Chapter III and IV. Significant differences between the mean values of drier years and the anomalously wet years are found. Patterns of increased  $\tau_a$  correspond to those of LAI and surface soil moisture. Especially in central Australia large changes in  $\tau_a$  and LAI are found, where the flush of grasses in a normally barren region affects both products.

This thesis developed and validated the retrieval of  $\tau_a$  from spaceborne active microwave observations and assesses its ability to monitor vegetation dynamics. It also identifies and analyses differences that arise between VNIR, passive and active microwave remote sensing, especially in boreal and deciduous forests. Overall, the  $\tau_a$  satisfactorily follows vegetation patterns and dynamics as observed in VNIR and passive microwave vegetation products. Therefore, missions like Metop's European Polar System - Second Generation and Sentinel-1 could retrieve or use  $\tau_a$  for vegetation mapping and algorithmic improvements.

# Contents

<b>Acknowledgements</b>	<b>vii</b>
<b>Abstract</b>	<b>ix</b>
<b>List of Figures</b>	<b>xiii</b>
<b>List of Tables</b>	<b>xvii</b>
<b>List of Acronyms</b>	<b>xix</b>
<b>List of Symbols</b>	<b>xxi</b>
<b>I Introduction</b>	<b>1</b>
1 Rationale . . . . .	3
2 Thesis research questions and objectives . . . . .	5
3 Thesis Outline . . . . .	5
<b>II Microwave Theory</b>	<b>7</b>
1 Active Microwave Remote Sensing Background . . . . .	9
2 Radar Equation . . . . .	9
3 Scattering properties of natural media . . . . .	9
3.1 Scattering mechanisms . . . . .	10
3.2 Soils . . . . .	10
3.3 Vegetation . . . . .	11
3.4 Scattering from vegetated surfaces . . . . .	11
4 Relating backscatter observations to land surface parameters . . . . .	13
4.1 Early field experiments . . . . .	13
4.2 Vegetation Monitoring with Airborne and Spaceborne Sensors . . . . .	14
4.3 Summary . . . . .	16
<b>III Analyzing the Vegetation Parameterization in the TU Wien ASCAT Soil Moisture Retrieval.</b>	<b>19</b>
1 Introduction . . . . .	21
2 Datasets . . . . .	25
2.1 Metop-A ASCAT and TU Wien soil moisture retrieval . . . . .	25
2.2 AMSR-E and the LPRM Vegetation Optical Depth ( $\tau_p$ ) retrieval . . . . .	26
2.3 Ancillary Data . . . . .	27
3 Methods and Metrics . . . . .	27
3.1 Vegetation optical depth retrieval ( $\tau_a$ ) from ASCAT observations . . . . .	27
3.2 Bare soil backscatter estimation and sensitivity analysis . . . . .	28
3.3 Metrics used for assessing $\tau_a$ and $\Theta_a$ . . . . .	31
4 Results and Discussion . . . . .	33
4.1 Effect of bare soil backscatter on $\tau_a$ retrievals . . . . .	33
4.2 Comparing $\tau_a$ and $\tau_p$ . . . . .	37
4.3 Effect of $\tau_a$ on soil moisture retrievals . . . . .	44
5 Conclusions . . . . .	45
<b>IV Inter-comparison of Vegetation Variables Derived from Microwave Instruments.</b>	<b>47</b>
1 Introduction . . . . .	49
2 Data and Methods . . . . .	51

2.1	Aquarius - Cross Ratio (CR) . . . . .	51
2.2	ASCAT - vegetation optical depth ( $\tau_a$ ) . . . . .	51
2.3	AMSR2 - vegetation optical depth ( $\tau_p$ ) . . . . .	52
2.4	SPOT-VEGETATION - Leaf Area Index (LAI) . . . . .	53
2.5	Additional Datasets . . . . .	53
2.6	Data preparation . . . . .	54
2.7	Comparison Metrics . . . . .	55
3	Global comparison of vegetation products . . . . .	55
3.1	Spatial comparison . . . . .	55
3.2	Temporal comparison . . . . .	57
3.3	Phenology comparison . . . . .	61
4	Conclusions . . . . .	66
<b>V</b>	<b>Assessing Vegetation Dynamics over Australia using Metop ASCAT.</b>	<b>67</b>
1	Introduction . . . . .	69
2	Data . . . . .	71
2.1	Metop-A ASCAT Vegetation optical depth ( $\tau_a$ ) and Surface Soil Moisture . .	71
2.2	Leaf Area Index (LAI) . . . . .	72
3	Methods . . . . .	74
4	Results and Discussion . . . . .	74
4.1	Quality Assessment of $\tau_a$ . . . . .	74
4.2	Inter-annual variability in $\tau_a$ . . . . .	77
5	Conclusions . . . . .	79
<b>VI</b>	<b>Conclusions and Outlook</b>	<b>81</b>
1	General . . . . .	83
2	Scientific implications . . . . .	83
2.1	Implications for backscatter modeling of vegetation . . . . .	83
2.2	Implications for vegetation monitoring . . . . .	84
2.3	Implications for the TU Wien soil moisture retrieval algorithm . . . . .	84
3	Future studies . . . . .	84
4	Applications of $\tau_a$ . . . . .	85
	<b>Bibliography</b>	<b>87</b>

# List of Figures

I.1	Conceptual relation between backscatter and incidence angle with relation to soil moisture and vegetation (taken from Naeimi et al. (2009)) . . . . .	4
II.1	Specular and diffuse scattering for surfaces with increasing roughness, after Ulaby et al. (1986). . . . .	10
II.2	Backscatter from a vegetated surface, consisting of three constituents: a. surface scattering attenuated by vegetation ( $\sigma_s^\circ$ ), volume scattering from vegetation ( $\sigma_v^\circ$ ) and multi-bounce scattering, interaction between soil and vegetation ( $\sigma_{int}^\circ$ ), after Ulaby et al. (1986). . . . .	12
II.3	Comparison ( $r_s$ ) between <i>in situ</i> measured soil moisture and $\sigma^\circ$ from the TU Wien retrieval algorithm, binned to three ranges of the original $\theta$ of observation. . . . .	16
III.1	The three components of the backscatter signal, the dry reference, wet reference and observed backscatter from the TU Wien change detection algorithm for a grid point in Queensland, Australia. . . . .	23
III.2	Map of Koeppen Geiger climate classes with the gridpoint locations. . . . .	24
III.3	The top two graphs (a and b) show $\Delta\sigma_s^\circ$ in dB calculated using IEM and the lower two graphs (c and d) show the $\sigma_{dry}^\circ$ . Where $\sigma_{dry}^\circ$ and $\Delta\sigma_s^\circ$ are calculated using the IEM for smooth (a and c) and rough (b and d) soil surfaces given by two root mean square heights: $s = 0.5$ cm and $s = 2.5$ cm. Data is displayed according to the global occurrence of soil properties: sand content (depicted on the x-axis) and clay content (depicted on the y-axis) by the size of the circles. The colorbar depicts the $\sigma_{dry}^\circ$ and $\Delta\sigma_s^\circ$ with low values in blue and high values in red. . . . .	30
III.4	Sensitivity of $\tau_a$ to a change in surface scattering $\Delta\sigma_s^\circ$ as given by (III.14), with the ratio of change on the x-axis. . . . .	32
III.5	Global map of mean $\tau_a$ (a) and $\tau_p$ (b) calculated over the period from 2007 to 2011. . . . .	34
III.6	Boxplots of $\tau_a$ (a) and $\tau_p$ (b) per Koeppen Geiger climate class. . . . .	34
III.7	Global $r_s$ between $\tau_a$ and $\tau_p$ . . . . .	36
III.8	Boxplot of the $r_s$ per Koeppen Geiger climate class for $\tau_a$ and $\tau_p$ . . . . .	39
III.9	Timeseries plots for $\tau_a$ (solid line), $\tau_p$ (dotted line) and GLDAS-Noah precipitation (grey bars) sorted after Koeppen Geiger climate classes; Tropical (a-c), Arid (row d-f), Temperate (g-i), Cold (j-l). Where the $\tau_p$ shows a climatology based on data over the period 2007-2011. The locations of the plots can be found in Figure III.2. The numbers above the plots represent the gridpoints and the Koeppen Geiger climate classes and R gives the $r_s$ . . . . .	41
III.10	Global Mean Square Error between $\tau_a$ and $\tau_p$ . . . . .	42
III.11	The difference in $r_s$ between $\Theta_a$ and $\Theta_{ERA}$ and $\sigma^\circ(40)$ and $\Theta_{ERA}$ , where positive values indicate areas where $r_s$ between $\Theta_a$ and $\Theta_{ERA}$ is higher than between $\sigma^\circ(40)$ and $\Theta_{ERA}$ , i.e. areas with positive impact of the vegetation correction. . . . .	42
III.12	The $\Delta PC$ over the normalized monthly differences of $\tau_p$ , where red areas represent high inter-annual variability. . . . .	43
III.13	Difference in $r_s$ between $\Theta_a$ and $\Theta_{ERA}$ and $\Theta_{\tau_p}$ and $\Theta_{ERA}$ where $\tau_a$ is substituted by $\tau_p$ . Negative values (in red) indicate areas where $r_s$ between $\Theta_{\tau_p}$ and $\Theta_{ERA}$ is higher than between $\Theta_a$ and $\Theta_{ERA}$ . . . . .	43

III.14	The relative frequency of $\Delta PC$ for points where when compared to ERA-Land $\Theta_{\tau_p}$ outperforms $\Theta_a$ ( $\Delta r_s < -0.1$ ) in pink-purple and where $\Theta_a$ outperforms $\Theta_{\tau_p}$ ( $\Delta r_s > 0.1$ ) in blue. . . . .	44
IV.1	CCI Land Cover map resampled to $1^\circ$ . Locations of gridpoint used in Fig. IV.3 and in Fig. IV.6 are indicated with white diamonds. . . . .	53
IV.2	Mean values for the four vegetation products: a. CR, b. $\tau_a$ , c. $\tau_p$ , d. LAI. . . . .	56
IV.3	Distribution of backscatter and the dry reference for the 23 different areas in evergreen needleleaf forests (top). The two lower plots depict the relation between the difference in summer (June, July, August (JJA)) and winter (December, January, February (DJF)) backscatter values compared to winter (DJF) air temperatures (left) and the bias between $\tau_a$ and $\tau_p$ in relation to winter (DJF) air temperatures (right). The color of the markers indicates the percentage of tree cover for the specific pixel, according to Hansen's tree cover map. The colorbar is depicted on the right side of the two plots. . . . .	57
IV.4	Global spearman correlation coefficients $r_s$ between the different products: a. $\tau_a - \tau_p$ , b. CR - LAI, $\tau_a - LAI$ , d. $\tau_p - LAI$ , e. $\tau_a - CR$ , f. $\tau_p - CR$ . Red areas indicate negative correlation coefficients and blue indicate positive correlation coefficients. . . . .	58
IV.5	Boxplot of $r_s$ for different land cover classes based on the CCI Land Cover dataset the colors depict the following combinations: green: $\tau_a - \tau_p$ , yellow: $\tau_a - LAI$ , purple: $\tau_a - CR$ , pink: CR - LAI, blue: $\tau_p - LAI$ and orange: $r\tau_p - CR$ . The acronyms can be found in Table IV.2 . . . . .	59
IV.6	Time series of climatologies of all four vegetation products, ASCAT VV, Aquarius VH and VV and precipitation for one $1^\circ$ pixel over Central African Republic at longitude 20.00 and latitude 7.00. The top barplot depicts the average precipitation per month over the period 2007 - 2013. The middle plot depicts the seasonalities of vegetation products in yellow: LAI, green: $\tau_p$ , pink: CR, blue: $\tau_a$ . The lower plot depicts the backscatter data over the year 2013 of Aquarius (VV in purple squares, VH in red triangles) and ASCAT VV (blue squares). . . . .	60
IV.7	Timing of SOS in month of the year for the four vegetation products: a. CR, b. $\tau_a$ , c. $\tau_p$ , d. LAI. . . . .	63
IV.8	The timing of POS in month of the year for the four vegetation products: a. CR, b. $\tau_a$ , c. $\tau_p$ , d. LAI. . . . .	64
IV.9	Difference in days between the three microwave products, $\tau_a$ , $\tau_p$ and CR, and LAI for SOS (left column) and POS (right column). Red colors represent areas where LAI is later than the respective product and blue colors represent areas where LAI is earlier than the respective microwave product. . . . .	65
V.1	A land cover map based on the European Space Agency's Climate Change Initiative Land Cover map of 2010. The map includes the location of the time series plots from Fig. V.5. . . . .	71
V.2	Spearman Rank Correlation between Leaf Area Index from SPOT-VGT and $\tau_a$ from ASCAT-A. . . . .	72
V.3	Spearman Rank Correlation between anomalies from Leaf Area Index from SPOT-VGT and $\tau_a$ from ASCAT-A. . . . .	73
V.4	Spearman Rank Correlation between GEOV1-LAI and $\tau_a$ from ASCAT-A for original time series and anomalies grouped per CCI Land Cover Class. . . . .	73
V.5	Time series for $\tau_a$ , LAI and $\Theta$ (left figure) and monthly averages of $\tau_a$ (right figure) for: a, b. interior Australia, c, d. Western Australia - croplands, e, f. Western Australia - Deciduous Broadleaf Forest. The locations of the gridpoints are depicted in Fig. V.1. . . . .	75
V.6	Lag in months based on Spearman Rank Correlation between Leaf Area Index from SPOT-VGT and $\tau_a$ from ASCAT-A. Red to orange colors indicate that $\tau_a$ lags behind LAI. . . . .	76

---

V.7	These plots depict the yearly differences from the mean over 2008 to 2014 for $\tau_a$ (left column), LAI (middle column) and $\Theta$ (right column). Higher (lower) than the ensemble average values are depicted in blue (red). . . . .	78
V.8	Areas where a significant difference (three standard deviations above the ensemble mean) between the annual mean of 2010 - 2011 compared to the ensemble mean is found are indicated in green. Areas that are two standard deviations above the ensemble mean are depicted in yellow. Plots show: a. $\tau_a$ , b. LAI, c. $\Theta$ . . . . .	79
V.9	Difference between normalized $\tau_a$ between the year 2008 and 2010 (2010-2008) per gridpoint, binned to their respective percentage forest cover. . . . .	79



# List of Tables

III.1	Koeppen Geiger climate classes after <a href="#">Kottek et al. (2006)</a> . . . . .	24
III.2	Bare soil backscatter and roughness measurements from literature . . . . .	29
III.3	Bare soil backscatter and $\Delta\sigma_s^\circ$ from data and modeling . . . . .	35
IV.1	Overview of the characteristics of all datasets used in the study. . . . .	50
IV.2	Median values per CCI Land Cover Class for $r_s$ between the different products. . .	59



## List of Acronyms

AMI	Advanced Microwave Instruments
AMSR-E	Advanced Microwave Scanning Radiometer - Earth
AMSR2	Advanced Microwave Scanning Radiometer 2
ASCAT	Advanced Scatterometer on-board Metop series
ASCAT-A	Advanced Scatterometer on-board Metop-A
ASCAT-B	Advanced Scatterometer on-board Metop-B
CCI	Climate Change Initiative
CYCLOPES	Carbon cYcle and Change in Land Observational Products from an Ensemble of Satellites
dB	Decibel
DBF	Deciduous Broadleaf Forest
DGG	Discrete Global Grid
DNF	Deciduous Needleleaf Forest
DOY	Day of Year
ECMWF	European Centre for Medium-Range Weather Forecasts
ECV	Essential Climate Variables
EBF	Evergreen Broadleaf Forest
ENF	Evergreen Needleleaf Forest
ENSO	El Niño Southern Oscillation
ERA	ECMWF Reanalysis
ERS	European Remote Sensing Satellites
ESA	European Space Agency (EU)
FAO	Food and Agriculture Organization of the United Nations
FaPAR	Fraction of Absorbed Photosynthetically Active Radiation
FWF	Austrian Science Foundation
GEOV1	Geoland-2 BioPar Version 1
GLDAS	Global Land Data Assimilation System
GPCC	Global Precipitation Climatology Centre
HWSD	Harmonized World Soil Database
IEM	Integrated Equation Model
IOD	Indian Ocean Dipole
JRC	Joint Research Centre (European Commission)
KGC	Koepfen Geiger Class
LAI	Leaf Area Index
LPRM	Land Parameter Retrieval Model
MFS	Mixed Forest/Shrublands
MIMICS	Michigan Microwave Canopy Scattering model
MODIS	Moderate Resolution Imaging Spectroradiometer
MSE	Mean Square Error
NASA	National Aeronautics and Space Administration (USA)
NDVI	Normalized Difference Vegetation Index
NWA	North West Australia
POS	Peak of Season
RFI	Radio Frequency Interference
RVI	Radar Vegetation Index

SAC-D	Satélite de Aplicaciones Científicas-D
SAM	Southern Annular Mode
SAR	Synthetic Aperture Radar
SEA	South Eastern Australia
SIR-C	Spaceborne Imaging Radar-C
SMAP	Soil Moisture Active Passive
SMOS	Soil Moisture Ocean Salinity
SOS	Start of Season
SPOT-VGT	Satellite Pour l'Observation de la Terre / VEGETATION
SST	Sea Surface Temperature
TU Wien	Technische Universität Wien (AT)
VNIR	Visible Near Infrared
VUA	VU University Amsterdam (NL)
VWC	Vegetation Water Content
WARP	Water Retrieval Package
WMO	World Meteorological Organization

# List of Symbols

$\gamma^2$	two-way transmissivity
$\epsilon$	dielectric constant
$\theta$	incidence angle
$\theta_r$	reference incidence angle
$\Delta\sigma^\circ$	difference between the wet and dry reference
$\Delta\sigma_s^\circ$	difference between the bare soil wet and dry reference
$\Delta PC$	Parde Coefficient
$\delta\tau_a$	change in $\tau_a$ as a function of a perturbation
$\kappa_e$	extinction coefficient
$\kappa_s$	scattering coefficient
$\lambda$	wavelength
$\sigma_b$	backscattering cross-section for a single particle
$\sigma_e$	extinction cross-section for a single particle
$\sigma^\circ$	normalized backscatter
$\sigma_{dry}^\circ$	dry reference
$\sigma_{s,dry}^\circ$	dry reference for bare soils
$\sigma_{wet}^\circ$	wet reference
$\sigma^\circ(40)$	normalized backscatter at incidence angle of 40°
$\sigma_{int}^\circ$	normalized backscatter interaction term between soil and vegetation
$\sigma_r^\circ$	normalized backscatter at reference incidence angle
$\sigma_s^\circ$	normalized bare soil backscatter
$\sigma_v^\circ$	normalized backscatter from vegetation
$\sigma_r'$	slope of the normalized backscatter - incidence angle curve
$\sigma_r''$	curvature of the normalized backscatter - incidence angle curve
$\sigma^\circ - \theta$	relationship between backscatter and incidence angle
$\Theta$	soil moisture
$\Theta_a$	soil moisture retrieved from ASCAT
$\Theta_{\tau_p}$	soil moisture retrieved from ASCAT using $\tau_p$ as vegetation correction
$\Theta_{ERA}$	soil moisture from ERA-Land
$\tau$	vegetation optical depth
$\tau_a$	vegetation optical depth from ASCAT active microwaves
$\tau_p$	vegetation optical depth from AMSR-E passive microwaves
$\tau - \omega$	vegetation optical depth - single scattering albedo
$\sigma_{dry}^\circ(t, \tau_p)$	dry reference based on $\tau_p$
$\omega$	single scattering albedo
$A_r$	effective receiving area of antenna
$d$	depth of vegetation layer
$G_t$	total gain
$I$	Intensity
$I_0$	initial intensity
$I_s$	intensity backscattered from surface
$I_v$	intensity backscattered from vegetation
$l$	correlation length
$N$	number of scattering particles per unit volume

$P_r$	total power received in Watt
$P_t$	power transmitted
$R$	reflectivity of the surface
$r_s$	Spearman Rank Correlation Coefficient of absolute values
$r_{sa}$	Spearman Rank Correlation Coefficient of anomalies
$s$	root mean square height of random soil roughness

# **Chapter I**

## **Introduction**



## 1 Rationale

Vegetation is a highly dynamic land surface parameter, and plays an important role in regional and global hydrological-, energy- and carbon cycles (Ahlström et al., 2015; Foley et al., 2005; Richardson et al., 2013). For example, leaf phenology directly influences evaporation and carbon assimilation. Timing of phenological parameters is highly affected by climate, where increasing temperatures can lead to an earlier onset of vegetation activity in spring (Linderholm, 2006). Model studies show that a lengthening of the growing season in northern high latitudes increases carbon uptake. On the other hand, in tropical regions, increasing temperatures lead to reduction in soil water content through increased evaporation, which in turn leads to a reduction of carbon uptake up to 80% (Berthelot et al., 2002). Also human impact causes changes in land use, for example by deforestation. Cramer et al. (2004) found from modelling studies that anthropogenic deforestation of tropical forests are likely to play a large role in the global carbon cycle. The authors also stated that better estimates of deforestation are needed for estimating tropical carbon sources and sinks. And with the increasing stress on food supply due to the growing world population and changing climate, vegetation monitoring becomes also more important in agricultural areas. By closely tracking crop conditions, droughts and subsequent crop losses could be identified early on allowing for adequate time to undertake mitigation measures. All these studies underwrite the great importance of vegetation monitoring in order to ensure the sustainable use and preservation of the Earth's surface and biomes.

To monitor vegetation on a global scale Visible Near Infrared (VNIR) remote sensing is a widely used tool. With the large absorption of light in the visible spectrum and the reflection of near infrared during photosynthesis, VNIR ratios can be exploited to monitor important vegetation canopy parameters. However, a disadvantage of VNIR remote sensing is its dependence on illumination, and its sensitivity to cloud cover and aerosols. In the last years spaceborne microwave observations have been used to develop vegetation datasets for vegetation monitoring (Owe et al., 2001; Liu et al., 2011; Jones et al., 2009). Microwave remote sensing monitoring has the advantage that it is not hindered by cloud cover, smoke, aerosol contamination and low solar illumination, unlike VNIR remote sensing. Microwaves are sensitive to a number of land surface parameters, including, but not limited to, water content in soil and vegetation and vegetation structure. Since a combination of soil and vegetation characteristics can lead to the same observation, the challenge is to link the microwave observations to the respective land surface parameter of interest.

Many studies have investigated the sensitivity of microwave sensors to soil and vegetation parameters (Owe et al., 2008; Liu et al., 2011; Paloscia et al., 2013; Jones et al., 2011; McColl et al., 2014; Jackson et al., 1982; Pulliainen et al., 1998; Kirdiashev et al., 1979; Wagner et al., 1999b,a). Well-known soil moisture and vegetation products are retrieved from passive microwave observations using the VUA-NASA Land Parameter Retrieval Model. This model, developed by Owe et al. (2001), uses a radiative transfer model to solve for vegetation optical depth ( $\tau_p$ ) and soil moisture simultaneously. Both the soil moisture and vegetation product have been validated in a number of studies (Liu et al., 2011; Andela et al., 2013; Draper et al., 2009; Rüdiger et al., 2009). Comparing 20 years of  $\tau_p$  data to AVHRR NDVI demonstrated that both datasets show similar seasonal cycles and correlate strongly, especially over grasslands (Liu et al., 2011). Studies also found that  $\tau_p$  was sensitive to both the crown of the canopy as well as the woody part of the vegetation. This is attributed to the longer wavelength of microwaves which enables them to penetrate the vegetation deeper than VNIR. This makes  $\tau_p$  complementary to well-known vegetation products like the Normalized Difference Vegetation Index (NDVI) (Andela et al., 2013; Jones et al., 2011). Recently, van Marle et al. (2016) applied  $\tau_p$  to estimate forest loss in the Amazon and confirmed a decrease of forest loss in Brazil. However, one of the disadvantages stated by the researchers is the coarse resolution of the dataset, which creates difficulties in capturing small-scale forest loss.

An important advantage of active microwave observations compared to passive microwave observations is their better spatial resolution. For example, soil moisture retrievals from ASCAT

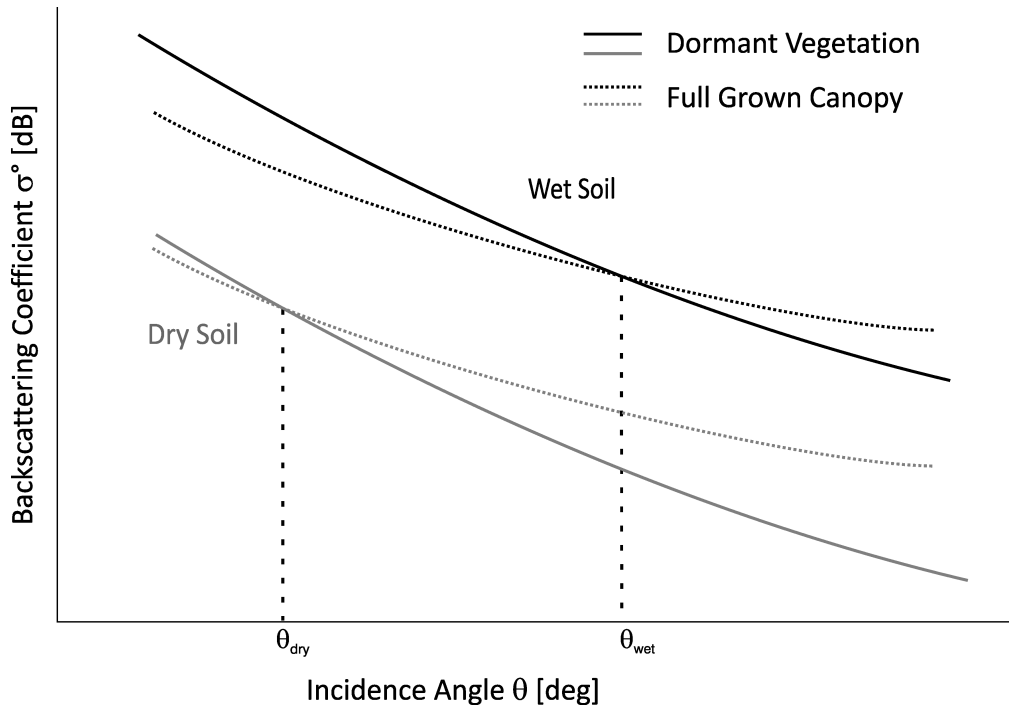


**Figure I.1:** Conceptual relation between backscatter and incidence angle with relation to soil moisture and vegetation (taken from Naeimi et al. (2009))

observations from Metop-A and Metop-B are available on a 12.5 km sampling. And ESA's new Sentinel 1 series provide backscatter observations at a 5 by 20 m resolution, enabling the retrieval of land surface parameters at a high spatial and temporal resolution. Several studies have suggested methods for retrieving soil moisture, and in some cases vegetation parameters, from active microwave observations (Magagi and Kerr, 1997; Pulliainen et al., 1998; Woodhouse and Hoekman, 2000). Wagner et al. (1999b) developed the TU Wien backscatter model used for operational soil moisture retrieval from the European Remote Sensing Satellites (ERS-1 and -2) Advanced Microwave Instruments (AMI) and the Advanced Scatterometers (ASCAT) on-board Metop-A and Metop-B. This model is a semi-empirical change detection method, which uses the multi-viewing capabilities of AMI and ASCAT to correct for vegetation effects. The main assumption in the algorithm is that a change in soil moisture moves the backscatter - incidence angle curve up and down in its entirety, whereas a change in vegetation changes the slope and curvature of this curve (Fig. I.1). Numerous studies have showed that this method provides global soil moisture time series which are comparable to model estimates and *in situ* measured soil moisture (Brocca et al., 2011; Rüdiger et al., 2009; Al-Yaari et al., 2014; Su et al., 2013; Paulik et al., 2014). Applications of the operational soil moisture product have increased in the last years, varying from predicting run-off (Scipal et al., 2005), estimating rainfall (Brocca et al., 2014), to improving flood and weather prediction (Wanders et al., 2014; de Rosnay et al., 2013).

Whether using active or passive microwave observations, a crucial step in any soil moisture retrieval algorithm is the accurate estimation of vegetation effects. Errors in parameterization of vegetation can propagate an error into the soil moisture products, which means that the quality of the vegetation parameterization can determine the quality of the soil moisture product. Nevertheless, the sensitivity of microwaves to water content in the soil and vegetation does not only challenge soil moisture retrieval, it also provides an opportunity to retrieve information on vegetation, as demonstrated by the retrieval of  $\tau_p$  in LPRM.

## 2 Thesis research questions and objectives

The aim of this thesis is to better understand backscatter response to vegetation dynamics. The first objective is to develop a methodology to estimate vegetation optical depth ( $\tau_a$ ) on a global basis by using active microwave observations and vegetation model parameters from the TU Wien backscatter model. Secondly,  $\tau_a$  is compared to other vegetation products to investigate their differences in sensitivity to vegetation dynamics. In addition, phenological parameters from  $\tau_a$  are estimated and compared to other products and the sensitivity to inter-annual variability in vegetation dynamics is assessed.  $\tau_a$  is directly related to the vegetation correction term within the TU Wien soil moisture retrieval algorithm, and provides an opportunity to validate the vegetation correction. Therefore, the last objective of this thesis is to identify weaknesses in the vegetation correction and provide improvements.

This thesis will deal with four key research questions concerning vegetation and soil moisture active microwave remote sensing:

1. How to retrieve vegetation optical depth from model parameters within the TU Wien algorithm?
2. How does the newly retrieved  $\tau_a$  correspond to existing vegetation products?
3. Can  $\tau_a$  be used to detect phenology parameters and inter-annual variability in vegetation dynamics?
4. In what way do errors in the vegetation model parameters propagate to the soil moisture estimate?

## 3 Thesis Outline

The thesis consists of six chapters of which three chapters are based on manuscripts that have been published in or submitted to scientific peer-reviewed journals. Chapter II of this thesis provides a general introduction in active microwave remote sensing theory. Also a more detailed overview of previous studies that have used active microwave observations to monitor and map vegetation is given. In Chapter III  $\tau_a$  is retrieved from active microwave observations using model parameters from the TU Wien soil moisture retrieval algorithm. Furthermore, the effect of vegetation on the soil moisture retrieval is investigated. Chapter IV will deal with an inter-comparison of vegetation products retrieved from active microwave sensors, i.e.  $\tau_a$  and a cross-ratio between co- and cross-polarized data, with existing vegetation products from VNIR and passive microwave observations. The products are compared in terms of spatial and temporal characteristics and phenological parameters, start and peak of season, derived from them. In Chapter V the sensitivity of  $\tau_a$  to inter-annual variability in vegetation is investigated over Mainland Australia. Finally, Chapter VI will present the main conclusions and the scientific impact of this thesis.



# **Chapter II**

## **Microwave Theory**



## 1 Active Microwave Remote Sensing Background

This chapter gives a general overview on microwave remote sensing and is based on work published by Woodhouse (2005), Ulaby et al. (1982, 1986) and text I contributed to the World Meteorological Organization Commission for Instruments and Methods of Observations (CIMO) Soil Moisture report.

## 2 Radar Equation

Active microwave remote sensing is based on the transmission of pulses of electromagnetic energy and the recording of the reflected signal at the sensor from the area of interest. In the case that the same antenna transmits and receives the signal, the radar equation is given as :

$$P_r = \frac{P_t G_t A_r}{(4\pi)^2 r^4} \sigma, \quad (\text{II.1})$$

where  $P_r$  is the total power received in Watt,  $P_t$  the power transmitted,  $G_t$  the antenna transmitting gain,  $A_r$  the effective receiving area of the antenna,  $r$  the distance between the antenna and target and  $\sigma$  is the radar cross section in  $\text{m}^2$  for the observed target.  $\sigma$  is the ratio between the power which is backscattered from the target and the power incident on the target. Since spaceborne active microwave sensors observe the Earth's surface, the amount of backscatter does not originate from a single object or target, but from an observed area, the instrument footprint. In order to compare measurements from different sensors to each other,  $\sigma$  is normalized for the area observed, which gives us the normalized backscatter coefficient or  $\sigma^\circ$ :

$$\sigma^\circ = \frac{\sigma}{A} = P_r \frac{(4\pi)^3 r^4}{P_t G_t^2 \lambda^2 A} \sigma, \quad (\text{II.2})$$

where  $\lambda$  is the wavelength.  $\sigma^\circ$  is unitless ( $\text{m}^2 \text{m}^{-2}$ ) and is usually expressed in decibels (dB).

## 3 Scattering properties of natural media

Microwave sensors operate at frequencies between 0.3 and 300 GHz, where the wavelength varies from 1 m to 1 mm (Ulaby et al., 1986). As an important quality, microwaves can travel through the Earth's atmosphere often undisturbed and thus allow observations independent from cloud coverage. Furthermore, since not bound to illumination by the Sun, microwave measurements are operable all-day-round. An important characteristic of microwaves is that the electromagnetic waves incident on the Earth's surface excite water molecules. The dipole character of water makes the water molecules continuously reorient in electromagnetic radiation's oscillating electric field, resulting in a high dielectric constant ( $\epsilon$ ) below the relaxation frequency of 17GHz (at a temperature of 20°C). The  $\epsilon$  of water can be described according to the Debye formulation, where it is dependent on frequency, the relaxation frequency and temperature.  $\epsilon$  is a complex number comprising a real and imaginary part, where the real part ( $\epsilon'$ ) determines the propagation characteristics of the energy, while the imaginary part ( $\epsilon''$ ) determines the absorption coefficient.

In microwave remote sensing of the land surface, scattering can originate from the soil, the vegetation or an interaction between the two. Soil and vegetation produce two different scattering mechanisms, namely surface scattering and volume scattering. In both scattering mechanisms the  $\epsilon$  of the medium plays an important role in the amount of backscattered energy. Microwave

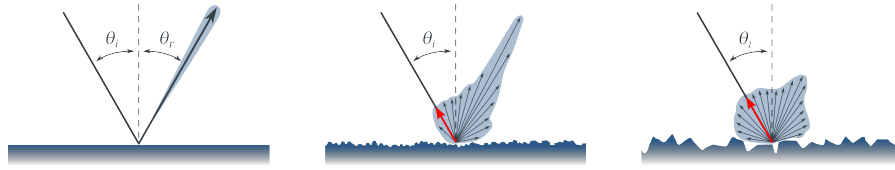


Figure II.1: Specular and diffuse scattering for surfaces with increasing roughness, after Ulaby et al. (1986).

remote sensing of vegetation and soil moisture follows from the large difference in the  $\epsilon$  of water ( $\epsilon = 80$ ) and soil ( $2 < \epsilon < 4$ ) and dry vegetation matter ( $1.5 < \epsilon < 2$ ) (Ulaby and El-Rayes, 1986). With these physical relations, it is possible to retrieve soil moisture and vegetation water content of the Earth's surface from active microwave remote sensing systems.

Kirchhoff's Radiation Law states that the emission of a body is equal to one minus its reflectivity. This means, emission and reflection are complementary, yielding that surfaces that are good scatterers are weak emitters, and vice versa. As a result, active and passive microwaves systems are influenced inversely by  $\epsilon$ .

### 3.1 Scattering mechanisms

If a medium is homogeneous, an electromagnetic wave is scattered at the boundary of two dielectric surfaces. Depending on the surface roughness of the dielectric surface, a mixture of specular and diffuse scattering exists. Fresnel's Reflection Law describes the relationship between  $\epsilon$  and reflectivity ( $R$ ) for smooth surfaces, where a higher  $\epsilon$  yields a higher rate of  $R$ . For a smooth dielectric surface, the incoming radiation is reflected forward in the same angle ( $\theta_r$ ) as the incoming angle ( $\theta_i$ ), so-called specular reflection (Fig. II.1). With increasing surface roughness, the diffuse component increases, i.e. the surface redirects the energy in all directions (Fig. II.1). If a surface is considered rough depends on the wavelength and is given by the Fraunhofer criterion, where a surface is rough if the phase difference due to the height difference of the surface between two reflected rays ( $h$ ) is less than a sixteenth of a wavelength:

$$h_{smooth} < \frac{\lambda}{32 \cos \theta} \quad (\text{II.3})$$

Volume scattering occurs if a medium is inhomogeneous and electromagnetic waves penetrate the lower medium. In the medium the scatterers, dielectric inhomogeneities, are randomly distributed across the medium. Energy is equally scattered in all directions regardless of  $\theta$  and only part of the energy is scattered backwards. The amount of backscattered energy is proportional to the number of dielectric inhomogeneities and the difference in  $\epsilon$  between them and the medium. Since in volume scattering the energy is equally scattered in all directions backscatter does not change with  $\theta$ .

### 3.2 Soils

Soil is a mixture of solid particles of mineral and organic matter, water and air. The  $\epsilon$  of soil is greatly influenced by the amount of water present in the pores since the  $\epsilon$  of water is an order of magnitude higher than that of soil particles. The relationship between soil moisture and the soil's  $\epsilon$  is almost linear, except at very low moisture values. Water in the soil can be either free or bound. Free water is able to be excited to their rotational energy states, which causes the high  $\epsilon$  of 80. However, at low soil moisture values a thin layer of water is strongly bounded to the surface of the soil particles. This bond is so strong that the free movement of the water is impeded. Hence in dry soils the water contributes less to the total  $\epsilon$  of the soil-water mixture. The amount of bound

water in soils depends on the particle size of the soil particles. Soils with a high clay content will have a lower  $\epsilon$  since the large surface area of clay particles can hold more water in the bound water phase. When the water in the soil freezes the  $\epsilon$  decreases strongly, since the water can no longer move freely.

Radiation incident on soils is partly reflected directly at the surface and a part is transmitted forward in the soil. The penetration depth of the wave varies from millimetres to decimetres depending on the soil moisture content. Due to the small penetration depth, volume scattering only occurs in a small layer and is often negligible. Hence, soils mainly display surface scattering which is mainly controlled by the dielectric properties and the geometry of the topsoil. Because of the combination of specular and diffuse backscatter from soils, the amount of backscatter decreases with increasing  $\theta$ . Since penetration depth depends on soil moisture content, very dry soils can potentially act as volume scatterers. This occurs mainly in sandy soils. Over extremely dry sandy deserts, microwaves can penetrate the soil for tens of metres until a boundary is met, for example bedrock, or will attenuate within the sand. With bedrock, bare rock and stony deserts scattering occurs at the rock-air boundary (or boundary with extremely dry sand as discussed before). In this case surface roughness is the parameter controlling the signal. Roughness of these surfaces can vary dramatically, from desert pavements to alluvial fans to fine, well-sorted aeolian deposits.

### 3.3 Vegetation

The dielectric constant of dry vegetation content is low, but since vegetation consists mainly of water,  $\epsilon$  of the total vegetation increases with vegetation water content. From this it can be inferred that backscatter increases with increasing vegetation water content. However, scattering from vegetation is not only dependent on water content, which makes vegetation backscatter modelling relatively complicated. The first problem arises with specifying the model parameters to adequately describe the vegetation, e.g. the size of the leaves and orientation. Secondly, vegetation mostly consists of three constituents, leaves, stalks and fruits. And each constituent has different characteristics, e.g. size, orientation and  $\epsilon$ . Taking all this into account, a scattering model would be very complicated and difficult to use. Hence, most vegetation scattering models are simplified in a way that they are usable but still represent realistic assumptions.

### 3.4 Scattering from vegetated surfaces

Usually, a vegetation canopy is not completely closed and radiation can penetrate through the vegetation. Hence, total backscatter from vegetation does not only comprise scattering from the vegetation itself, it also includes the backscatter originating from the underlying surface attenuated by the vegetation, and interaction between soil and vegetation (Fig. II.2). The total backscatter can be represented in a radiative transfer equation with three constituents:

$$\sigma^{\circ} = \sigma_s^{\circ} + \sigma_v^{\circ} + \sigma_{int}^{\circ} \quad (\text{II.4})$$

To simplify backscatter from vegetated surfaces, the vegetation is often regarded as a cloud of randomly distributed water droplets which are structurally held in place by dry matter. This way the predominant mechanism responsible for the backscatter from vegetation is volume scattering. The most well-known model, which is also used in this thesis, is the water-cloud model developed by [Attema and Ulaby \(1978\)](#). The model represents the total backscatter in  $\text{m}^2 \text{m}^{-2}$  as the incoherent sum of the vegetation contribution,  $\sigma_v^{\circ}$  and the contribution of the underlying soil  $\sigma_s^{\circ}$ , which is attenuated by the vegetation through the transmissivity  $\gamma$ . Since the error incurred as a result of ignoring  $\sigma_{int}^{\circ}$  rarely exceeded 1 dB, it was ignored in this formulation.

Scattering and extinction from vegetation are controlled by the volume scattering coefficient

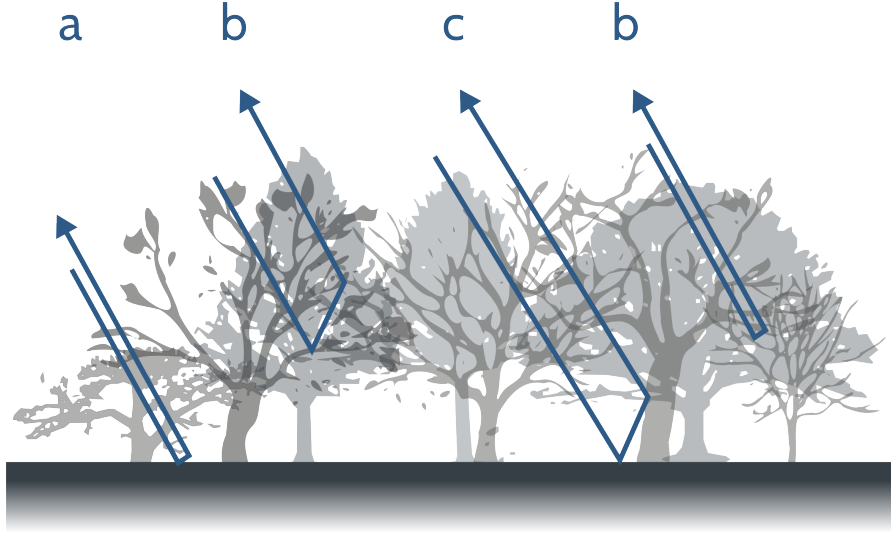


**Figure II.2:** Backscatter from a vegetated surface, consisting of three constituents: a. surface scattering attenuated by vegetation ( $\sigma_s^\circ$ ), volume scattering from vegetation ( $\sigma_v^\circ$ ) and multi-bounce scattering, interaction between soil and vegetation ( $\sigma_{int}^\circ$ ), after Ulaby et al. (1986).

( $\kappa_s$ ) and extinction coefficient ( $\kappa_e$ ), which depend on the number of water droplets, and the scattering and extinction cross-section of each particle:

$$\kappa_s = N\sigma_b \quad (\text{II.5})$$

$$\kappa_e = N\sigma_e \quad (\text{II.6})$$

, where  $N$  is the number of scattering particles per unit volume and  $\sigma_b$  and  $\sigma_e$  the backscattering and extinction cross-section for one single particle. Generally,  $\kappa_s$  and  $\kappa_e$  depend on plant geometry and water content of the canopy (Attema and Ulaby, 1978) and were empirically accounted for by fitting observed data to the model equation for different crop types. Intensity of radiation incident perpendicular to the surface travelling through the vegetation and reaching the soil surface is a function of the thickness of the vegetation layer ( $d$ ) and attenuated by the vegetation as follows:

$$I(d) = I_0 e^{-\kappa_e d} \quad (\text{II.7})$$

Where  $I_0$  is the the initial intensity. The intensity of the backscattered part of this radiation depends on the reflectivity of the surface ( $R$ ) and travels a second time through the vegetation and is attenuated again, giving us:

$$I_s = R I_0 e^{-2\kappa_e d} \quad (\text{II.8})$$

$\kappa_e d$  can be described as the vegetation optical depth ( $\tau$ ) and  $e^{-2\kappa_e d}$  is  $\gamma^2$ , the two-way attenuation factor, which accounts for the loss of energy due to absorption and scattering. Since backscatter from vegetation is the relation between incident and received intensity, in this case  $I_0$  and  $I_s$ , attenuated backscatter from the surface ( $\sigma_s$ ) can be described as:

$$\sigma_s = \frac{I_s}{I_0} = R\gamma^2 \quad (\text{II.9})$$

Intensity of backscattered radiation from the vegetation is the sum of the contributions of the particles in the vegetation taking into account the attenuation:

$$I_v = \int_0^d \kappa_s I_0 e^{-2\kappa_e z} dz = \frac{\kappa_s}{2\kappa_e} I_0 (1 - e^{-2\kappa_e d}) \quad (\text{II.10})$$

$\sigma_v$  can then be described as the ratio between  $I_v$  and  $I_0$ :

$$\sigma_v = \frac{I_v}{I_0} = \frac{\kappa_s}{2\kappa_e} \left(1 - e^{-2\kappa_e d}\right) = \frac{\omega}{2} \left(1 - e^{-2\kappa_e d}\right) \quad (\text{II.11})$$

where  $\omega$  presents the single scattering albedo which is given as the fraction between the scattering coefficient and extinction coefficient:

$$\omega = \frac{\kappa_s}{\kappa_e} \quad (\text{II.12})$$

For a rough surface, a side-looking geometry where  $\theta$  is between  $0^\circ$  and  $90^\circ$  and describing the canopy as a Rayleigh scattering medium, a more general formulation of the water-cloud model is available which only uses two parameters,  $\omega$  and  $\tau$ :

$$\sigma^\circ(\theta) = \frac{3\omega \cos(\theta)}{4} (1 + \gamma^2) + \sigma_s^\circ \gamma^2 \quad (\text{II.13})$$

where  $\sigma_s^\circ$  is the bare soil backscatter coefficient. Since the travel-path through the vegetation increases with increasing  $\theta$ ,  $\gamma^2$  is dependent on  $\theta$  as:

$$\gamma^2 = e^{-\frac{2\tau}{\cos(\theta)}} \quad (\text{II.14})$$

Based on these equations it becomes clear that the volume scattering component of the vegetation becomes more important at larger  $\theta$ , since the soil scattering is more attenuated by the longer travel length through the vegetation.

However, the uniform canopy which is assumed in the water-cloud model is not always adequate. Especially, not accounting for the contribution of interaction between soil and vegetation might affect  $\sigma^\circ$ . The effect of each major plant constituent, i.e. leaves, stalks, and fruits, on backscatter at 5.1 GHz was investigated by defoliating corn. For  $\theta > 30^\circ$ ,  $\sigma^\circ$  is bigger from stalks and cobs than from the whole plant. The backscatter from stalks or interaction between soil and stalks is very significant, but is strongly attenuated by the presence of leaves. These observations suggest that separate contributions of leaves and stalks should be taken into account. Another reason for the higher backscatter from defoliated corn could also be the contribution of  $\sigma_{int}^\circ$  to the total backscatter. When comparing the  $\sigma_{int}^\circ$  contribution to the contributions of  $\sigma_v^\circ$  and  $\sigma_s^\circ$ , [Ulaby et al. \(1986\)](#) found that at  $\theta > 20^\circ$  and low  $\tau$ ,  $\sigma_{int}^\circ$  may become important. For L-band HH polarized data at  $\theta = 30^\circ$ , [Dobson and Ulaby \(1986b\)](#) found that backscatter was strongly related to soil moisture. Using a backscatter model, the authors found that when senescent leaves in corn provide little attenuation, the dominant term is the forward scattering from the soil via the wet corn stalks. [Dobson and Ulaby \(1986a\)](#) concluded that at higher incidence angles the loss of sensitivity to soil moisture due to higher values of  $\tau$  is reduced by the interaction term. Especially at the beginning of vegetation growth, for wet soil conditions,  $\sigma_{int}^\circ$  compensates the attenuation of vegetation leading to higher total backscatter. In addition, for VH polarized backscatter,  $\sigma_{int}^\circ$  was usually the dominant contributor to  $\sigma^\circ$  ([Ulaby et al., 1986](#)). To account for these issues, [Ulaby et al. \(1990\)](#) developed a multi-layer, multi-scattering canopy scattering model, the Michigan Microwave Canopy Scattering model (MIMICS). MIMICS is often used to model the backscatter from a vegetation surface, although the detailed input needed on plant geometry makes it difficult to apply on a large scale.

## 4 Relating backscatter observations to land surface parameters

### 4.1 Early field experiments

Field experiments in the 1970s, based largely on truck-mounted scatterometer measurements, investigated the dependence of microwave backscatter on surface roughness, soil moisture (⊙),

texture and vegetation. One of the most well-known series of experiments was performed by Ulaby et al. (Ulaby and Batlivala, 1976; Ulaby et al., 1978, 1979) for backscatter from bare soils and vegetated soils. Co- and cross-polarized backscatter was measured from 1-8 GHz at  $\theta$  varying between  $0^\circ$  and  $40^\circ$  over soils with different soil moisture, surface roughness and vegetation. The first experiment demonstrated that the highest sensitivity to soil moisture is obtained at a frequency around 5 GHz over a range of  $\theta$  between  $7^\circ$  and  $17^\circ$ . At this frequency and  $\theta$ , the influence of surface roughness on the backscatter is minimized. For a combination of crops the highest correlation between soil moisture and  $\sigma^\circ$  was found at a frequency of 4.25 GHz and  $\theta$  of  $10^\circ$ . At frequencies below 6 GHz and  $\theta < 20^\circ$  minimal vegetation attenuation effects are exhibited. But the sensitivity of  $\sigma^\circ$  to soil moisture decreases rapidly with increasing frequency and  $\theta$ .

Ulaby et al. (1982) also illustrated the role of the soil term,  $\sigma_s^\circ \gamma^2$ , relative to the vegetation term,  $\sigma_v^\circ$ .  $\sigma^\circ$  was measured at 4.25 GHz over corn (height = 2.2 m), milo (height = 1.05 m), soybeans (height = 0.78 m) and wheat (height = 1 m) for dry and wet soil and over a range of  $\theta$ . Curves of  $\sigma^\circ$  and  $\theta$  showed that measured  $\sigma^\circ$  is consistently higher for the wet soil cases than for the dry soil cases, and it was inferred that the soil contribution is certainly significant. For a frequency of 9 GHz the observed  $\sigma^\circ$  was found to be insensitive to soil moisture when  $\theta > 30^\circ$ . From experiment results, Ulaby et al. (1982) argues that even with a combination of  $\theta$  and frequency at which the soil contribution is assumed to be negligible, it can still contribute to the signal since soil can be exposed during early stages of growth and during the stage prior to harvest of crops vegetation water content is often lost making the crops more transparent.

## 4.2 Vegetation Monitoring with Airborne and Spaceborne Sensors

### Co-polarized backscatter

Wegmuller and Werner (1997) used ERS-1 SAR interferometry to map forest and monitor cropland. For mapping forest, accuracies of 90% were obtained. A strong correlation between interferometric correlation and soil cover fraction of young rape seed was found. Low interferometric correlation indicates dense vegetation or farming activity. Over the Italian test site Montespertoli, many airborne SAR campaigns have been conducted. One of the first studies, published by Ferrazzoli et al. (1992) looked at the sensitivity of co-polarized backscatter at different frequencies to vegetation and soil moisture. At  $\theta = 40^\circ$  both C-band and L-band observations related to LAI. However, for thick leaf crops saturation occurred once LAI was in the order of 2 or 3. This was also found by McNairn et al. (2000) for C-band HH backscatter. Ferrazzoli et al. (1992) also found that at  $\theta = 10^\circ$  a sensitivity to soil moisture was found which was comparable to the sensitivity found by Ulaby et al. (1986). While testing the potential of ERS-1 SAR over the Montespertoli test site, Paloscia et al. (1999) found that C-band co-polarized backscatter from ERS-1 SAR was sensitive to vegetation biomass if broad leaf crops are separated from small leaf crops. In addition to the sensitivity to vegetation biomass, a clear soil moisture signal was found in the data, where backscatter was lower during dry soil conditions. The signal of C-band was also found to be well correlated to forest woody volume.

On a larger spatial scale, the sensitivity of ERS-1 scatterometer data to vegetation was investigated in a series of studies by Frison and Mougin (1996) and Prigent et al. (2001). In these studies, backscatter was normalized to incidence angles of  $20^\circ$  and  $45^\circ$  and averaged to monthly values. Frison and Mougin (1996) compared these monthly values to the Global Vegetation Index (GVI) from VNIR observations. Although correlations were not quantified, a substantial agreement was found between backscatter and GVI at  $\theta = 45^\circ$ . At  $\theta = 20^\circ$  it was concluded that backscatter was more sensitive to soil moisture content. In later studies the contributions to total backscatter of different components are investigated over a Saharo-Sahel region in Mali (Frison et al., 1998). Here it was found that monthly averages of backscatter at  $\theta = 45^\circ$  display a seasonality associated to the development and senescence of grasses. The semi-empirical backscatter model showed that the

soil contribution to the total backscatter is always present. A follow up study by Jarlan et al. (2002) over the same site showed a high correlation ( $r^2 = 0.83$ ) between rainfall and the difference in the maximum and minimum backscatter at  $\theta = 45^\circ$ . A weak correlation ( $r^2 = 0.46$ ) was found between herbaceous mass and the difference in maximum and minimum backscatter. It is also found that within the Sahel region the soil contribution always dominates except in the Sudano-Sahelian subzone.

Frolking et al. (2006) compared Seawinds Ku-band scatterometer backscatter data at  $\theta = 54^\circ$  to LAI and modelled backscatter using the Michigan Microwave Canopy Scattering model. Here  $r^2$  was generally higher than 0.5 for sites with relatively low LAI or a large seasonal range in LAI. The modelling with MIMICS suggested that with low values for LAI a strong sensitivity to  $\Theta$  is present. Magagi and Kerr (1997) looked at the sensitivity of backscatter from ERS-1 to soil and vegetation contributions under different incidence angles. Backscatter was modelled using a simple water-cloud model. Results showed that the contribution of vegetation to the total backscatter does not change with  $\theta$ . The contribution of the soil decreases with increasing  $\theta$ , where at the maximum  $\theta$  the soil contributes for ca. 50% to the signal. This behaviour is in agreement with surface and volume scattering theory as described in the previous section. However, this study also found that for  $\tau > 1$  the soil contribution is masked by the canopy and retrieval of soil moisture is not feasible. Using the same monthly averaging method as Frison and Mougin (1996), Prigent et al. (2001) found that backscatter from ERS-1 shows good potential for monitoring vegetation since a dynamic range of 10 dB was found between rain forest and grassland.

Wagner et al. (1999a) developed a soil moisture retrieval algorithm for the ERS-1 scatterometer, where vegetation is parameterized by the slope of the backscatter relationship to  $\theta$ . The vegetation parameterization is based on the assumption that a change in soil moisture moves the  $\sigma^\circ - \theta$  curve up and down, but that a change in vegetation changes the slope of the curve (Fig. I.1). This approach follows the assumption that vegetation is a volume scatterer, and hence backscatter is uniformly distributed over a wide range of  $\theta$ . Soil, however, causes surface reflection, which is sensitive to  $\theta$  in a way that with increasing  $\theta$   $\sigma^\circ$  decreases rapidly. These assumptions are based on surface and volume scattering theory and were confirmed in studies on different scales (Magagi and Kerr, 1997; Ulaby et al., 1986; Wagner et al., 1999a). With this approach the effect of soil moisture is taken out more carefully. A comparison with NDVI and precipitation over the Iberian Peninsula suggested that the backscatter was dominated by changes in soil moisture. The slope parameter was linked to the NDVI. However, the lag between NDVI and the slope parameter was attributed to the fact that NDVI is more sensitive to the photosynthetic activity and the slope parameter more sensitive to the wet biomass and that these two variables do not show the same temporal behaviour. Doubkova et al. (2009) later compared the development of NDVI and the slope derived from ERS-AMI over ten targets exhibiting different land surface phenologies. The slope parameter followed the pattern as observed in NDVI, but also here a lag between the NDVI and slope parameter was found.

The discussed studies show different results in the sensitivity of backscatter to land surface parameters at different  $\theta$ . As a test of backscatter sensitivity to soil moisture, we examined the sensitivity of ASCAT backscatter normalized to  $\theta = 40^\circ$  to soil moisture. Normalized backscatter is compared to *in situ* soil moisture over an area in France with dense vegetation with a mean  $\tau$  of 0.69.  $r_s$  is calculated between observations obtained under three different ranges of  $\theta$  and *in situ* soil moisture. As can be seen from Fig.II.3,  $r_s$  does not visibly decrease with increasing  $\theta$ . This suggests that there is no clear effect of  $\theta$  on the normalized signal and that even over a region with  $\tau = 0.69$ , the sensitivity of  $\sigma^\circ$  to soil moisture is not lost with increasing  $\theta$ . A possible explanation for this could be that the sensitivity to soil moisture is amplified by multiple scattering between soil and vegetation, as was also found in Dobson and Ulaby (1986b,a); Ulaby et al. (1986). It also shows that even at high  $\theta$  soil moisture still contributes to the backscatter signal and that a simple averaging of backscatter observed at a high incidence angle is likely to reflect dynamics in both soil moisture and vegetation.

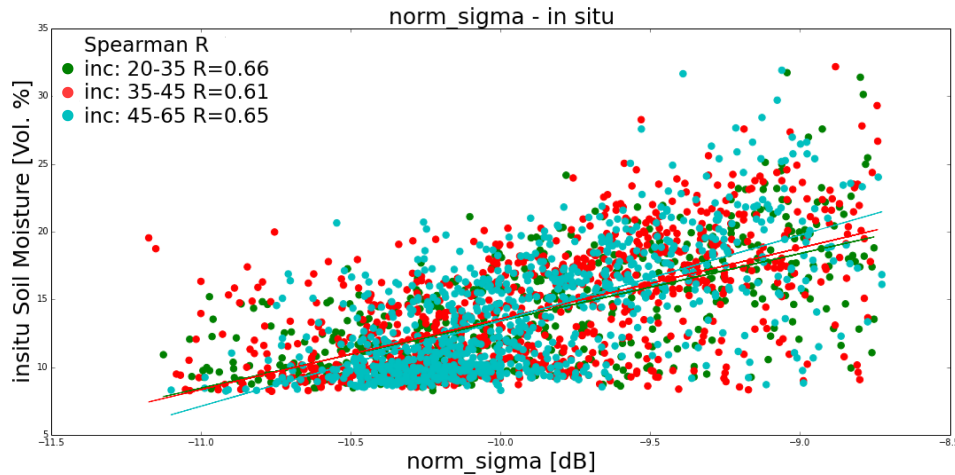


**Figure II.3:** Comparison ( $r_s$ ) between *in situ* measured soil moisture and  $\sigma^\circ$  from the TU Wien retrieval algorithm, binned to three ranges of the original  $\theta$  of observation.

### Cross-polarized backscatter

Other studies, mainly using SAR, have also focused on the use of cross-polarized data for vegetation monitoring. Generally, cross-polarized backscatter increases stronger with volume scattering and soil vegetation interaction than co-polarized backscatter. Since vegetation is considered a volume scatterer, cross-polarized backscatter increases stronger with vegetation than co-polarized backscatter. Using airborne SAR, [Toan et al. \(1992a\)](#) performed a linear regression analysis between backscatter at P- and L-band and forest parameters. The results found in this study confirm the possibility to infer forest above ground biomass from L-band backscatter data. The best results are found for cross-polarized backscatter and for P-band backscatter. [Ferrazzoli et al. \(1997\)](#) found that HV-polarized backscatter at C-band at  $\theta = 35^\circ$  correlated strongly ( $r^2 = 0.75$ ) with crop biomass over colza, wheat and alfalfa, but that saturation occurred in corn, sunflower and sorghum. [Paloscia et al. \(1998\)](#) found high correlations between vegetation biomass and HV backscatter over broad leaf crops such as sunflower. Crops which are characterized by smaller, elliptic constituents, as is the case in wheat and grass, backscatter showed no clear response or even decreased with increasing vegetation biomass. A later study by [Paloscia et al. \(2013\)](#) looked at the cross-ratio between VH and VV data (CR) from SIR-C, X-SAR and ASAR over different sites in Italy. In this study a strong sensitivity of CR to NDVI was found, whereas the sensitivity to soil moisture was negligible. [McNairn et al. \(2004\)](#) even could identify zones of higher crop productivity in a field based on HV-polarized data. Based on field experiments over soybeans and rice, [Kim et al. \(2012b\)](#) found that the Radar Vegetation Index (RVI), calculated from HH, VV and HV polarized data at L-band, correlated well with LAI, NDVI and vegetation water content.

Using spaceborne Aquarius scatterometer L-band data, [McColl et al. \(2014\)](#) calculated RVI on a global scale. It was found that spatial patterns of RVI correspond to expected vegetation patterns. In deserts RVI was found to be too high, and this was attributed to miscalibration of the sensor. Over high northern latitudes freeze-thawing affected RVI.

### 4.3 Summary

This literature review shows different methods which relate backscatter to soil moisture and vegetation dynamics and illustrate some of the difficulties and disagreements that exist. On a field scale, studies agree that the relation between backscatter and vegetation parameters varies per crop type and forest. Mainly the geometry and size of constituents (branches, leaves, trunks)

seem to affect the backscatter. Even though most of the discussed studies focus on the sensitivity to vegetation parameters, many find also a clear sensitivity to soil moisture. Most studies agree that the sensitivity to soil moisture increases with decreasing  $\theta$ . At a larger scale, studies have used monthly averages of ERS-1 scatterometer data at  $\theta = 45^\circ$  to investigate vegetation parameters. With these studies one can argue that calculating monthly averages of backscatter suppresses the more dynamic soil moisture signal, but does not completely remove it as is shown in Fig.II.3. Since soil moisture and vegetation are coupled in many areas one needs to be careful drawing conclusions based on monthly averages. And some of the discussed studies demonstrate the sensitivity of backscatter to soil moisture even at higher  $\theta$ . The studies show that in order to obtain information on vegetation dynamics from backscatter observations, one needs to account for the effect of soil moisture on the signal. The approach presented by [Wagner et al. \(1999a\)](#) provides a method to separate the soil signal from the vegetation signal, which is based on surface and volume scattering theory validated in previous studies.



# Chapter III

## Analyzing the Vegetation Parameterization in the TU Wien ASCAT Soil Moisture Retrieval.

Mariette Vreugdenhil, Wouter Dorigo, Wolfgang Wagner, Richard de Jeu,  
Sebastian Hahn, Margreet van Marle

This chapter is based on a paper which is published in  
*IEEE Transactions on Geoscience and Remote Sensing* Vol. 54 (6), pp.3513–3531, 2016.  
DOI: 10.1109/TGRS.2016.2519842

© 2016 IEEE

*The layout has been revised.*

## Abstract

*In microwave remote sensing of the Earth surface the satellite signal holds information on both soil moisture and vegetation. This necessitates a correction for vegetation effects when retrieving soil moisture. This study assesses the strengths and weaknesses of the existing vegetation correction as part of the TU Wien method for soil moisture retrieval from coarse scale active microwave observations. In this method, vegetation is based on a multi-year climatology of backscatter variations related to phenology. To assess the plausibility of the correction method, we first convert the correction terms for retrievals from the Advanced Scatterometer (ASCAT) into estimates of vegetation optical depth ( $\tau_a$ ) using a water-cloud model. The spatial and temporal behaviour of the newly developed  $\tau_a$  is compared to optical depth retrieved from passive microwave observations with the Land Parameter Retrieval Model ( $\tau_p$ ). Spatial patterns correspond well, although low values for  $\tau_a$  are found over boreal forests. Temporal correlation between the two products is high ( $r_s = 0.5$ ), although negative correlations are observed in drylands. This comparison shows that  $\tau_a$  and thus the vegetation correction method are sensitive to vegetation dynamics. Effects of the vegetation correction on soil moisture retrievals are investigated by comparing retrieved soil moisture before and after applying the correction term to modeled soil moisture. The vegetation correction increases the quality of the soil moisture product. In areas of high inter-annual variability in vegetation dynamics, we observed a negative impact of the vegetation correction on the soil moisture, with a decrease in correlation up to 0.4. It emphasizes the need for a dynamic vegetation correction in areas with high inter-annual variability.*

## 1 Introduction

Spaceborne microwave remote sensing has proven to provide reliable soil moisture observations on a global scale (Dorigo et al., 2015; Su et al., 2013; Albergel et al., 2012; Brocca et al., 2011). Microwaves are mainly sensitive to water content in both the soil and the vegetation, and separating these components from each other is not straightforward. Many efforts have already been undertaken to correct for the impact of vegetation in the soil moisture retrieval in both active and passive microwave remote sensing (Kerr et al., 2012; Owe et al., 2008; Kim et al., 2014, 2012a; Wagner et al., 1999b; Naeimi et al., 2009).

Most microwave retrieval algorithms use a radiative transfer model, so-called  $\tau - \omega$  model, as a basis to retrieve soil moisture. As the name suggests, a  $\tau - \omega$  model is based on two parameters, namely the optical depth  $\tau$  and single scattering albedo  $\omega$ , which describe the attenuation and scattering by the vegetation. For example, the VUA-NASA Land Parameter Retrieval Model (Owe et al., 2008) uses a simple radiative transfer model and a microwave polarization ratio to retrieve both soil dielectric constants and vegetation optical depth ( $\tau_p$ ) simultaneously from brightness temperatures measured by e.g. AMSR-E, AMSR2 or SMOS microwave radiometers (van der Schalie et al., 2015; Parinussa et al., 2014; Owe et al., 2008). The LPRM approach is based on the assumption of polarization independence to  $\tau$  and  $\omega$ , which makes it possible to solve  $\tau_p$  analytically (Meesters et al., 2005). An iterative approach is used to optimize for the dielectric constant. A dielectric mixing model is employed to calculate soil moisture from the dielectric constant, using auxiliary data on soil physical properties such as particle size distribution, porosity and wilting point from soil maps based on the FAO soil map of the world (1974-1981, scale 1:5,000,000). An advantage of this retrieval algorithm is that due to the analytical derivation of the optical depth only one variable needs to be optimized: the dielectric constant.

The official Soil Moisture Ocean Salinity (SMOS) retrieval algorithm uses a decision tree, based on auxiliary land cover data, to select the brightness temperature models and reference values to be used for a certain surface type. Over vegetated areas a  $\tau - \omega$  model is used (Kerr et al., 2012) to retrieve optical depth and soil moisture. The best-suited set of parameters, i.e.  $\tau_p$  and soil moisture, are retrieved by minimizing a cost function between the modeled and measured

brightness temperatures in an iterative approach (Kerr et al., 2012).

For active microwave observations, the available algorithms use diverse approaches. To retrieve soil moisture from ERS-1 Advanced Microwave Instruments (AMI) Pulliainen et al. (1994, 1996) used a least-squares algorithm with a semi-empirical backscatter model, which incorporates a  $\tau - \omega$  model for canopy backscatter and extinction. Promising results for soil moisture and frozen soil monitoring were found. However, a priori data on land cover and vegetation biomass are needed, making it more difficult to apply the method on a global scale. The current retrieval algorithm for the Soil Moisture Active Passive (SMAP) scatterometer employs a time series data cube approach (Kim et al., 2014, 2012a), using an iterative minimization function between modeled and observed backscatter. The data cube approach leaves three unknown variables, soil moisture, roughness and vegetation water content (VWC). Roughness and VWC will be defined using auxiliary data, whereas VWC will be retrieved from either the Radar Vegetation Index, calculated from cross-polarization backscatter data, or from NDVI. As for the SMOS algorithm, the SMAP algorithm uses auxiliary data to select the backscatter model applied to retrieve soil moisture for a certain pixel, in this case a land cover map.

The TU Wien soil moisture retrieval algorithm (Wagner et al., 1999b; Naeimi et al., 2009) employs a change detection method to retrieve soil moisture from scatterometers with multi-incidence angle viewing capabilities, i.e. EUMETSAT's Metop-A and Metop-B Advanced scatterometers (ASCAT), and AMI on-board ERS-1 and ERS-2. One basic assumption for the change detection method is that backscatter ( $\sigma^\circ$ ), expressed in decibels, is linearly related to surface soil moisture content. Furthermore,  $\sigma^\circ$  is strongly dependent on incidence angle ( $\theta$ ) and the slope and curvature of the relationship between backscatter and incidence angle ( $\sigma^\circ(\theta)$ ) are assumed to be affected only by vegetation density, but not by changes in soil moisture (Fig. I.1). Subsequently, the slope and curvature obtained from  $\sigma^\circ$  observations under different incidence angles are used to parameterize the vegetation for every day of the year and for every gridpoint. To account for noise in the backscatter measurements and to ensure that an entire range of incidence angles is covered, 366 slope and curvature pairs (i.e. one for each day of the year) are determined by averaging backscatter observations of several years. Currently, the entire observation period is used, i.e. 15 years for ERS and 8 years for ASCAT. Consequently, the vegetation parameter in the TU Wien retrieval algorithm is based on a climatology which does not take into account inter-annual variability. A more detailed description of the algorithm can be found in section II.

The different algorithms discussed above give a brief overview of the approaches used to account for vegetation in soil moisture retrieval algorithms and their strengths and weaknesses. Apart from the TU Wien retrieval algorithm, most retrieval algorithms use auxiliary data in the form of look-up tables based on land cover maps or additional soil property data to retrieve soil dielectric constants. The TU Wien approach provides soil moisture in relative units between 0% (dry soil surface) and 100% (saturated soil surface). It is evident that the quality of the vegetation parameterization can determine to a large extent the quality of the retrieved soil moisture, since the vegetation correction can propagate an error into the soil moisture product.

Several studies have assessed the vegetation parameterization in the TU Wien change detection method and in the VUA-NASA LPRM by comparing it to other vegetation products and indices. Wagner et al. (1999a) compared backscatter observations and the slope parameter retrieved from ERS Scatterometer observations to precipitation and NDVI over the Iberian Peninsula. They concluded that the temporal variation of the backscatter observations is dominated by changes in soil moisture but the slope parameter is linked to seasonal dynamics in the wet biomass of the vegetation. A lag in the maxima between the slope and NDVI was observed, attributed to the fact that the peak of photosynthetic activity and greenness of the vegetation is in early spring, whereas the peak in overall biomass is in summer. Similar results were found for  $\tau_p$  retrieved from AMSR-E with the VUA-NASA algorithm, where  $\tau_p$  over drylands was found to be more sensitive to long term precipitation variations and NDVI responded more to short-term variations (Andela et al., 2013). This was attributed to the fact that the  $\tau_p$  is more sensitive to woody vegetation, which can absorb water from deeper soil layers, whereas NDVI is more sensitive to canopy cover and

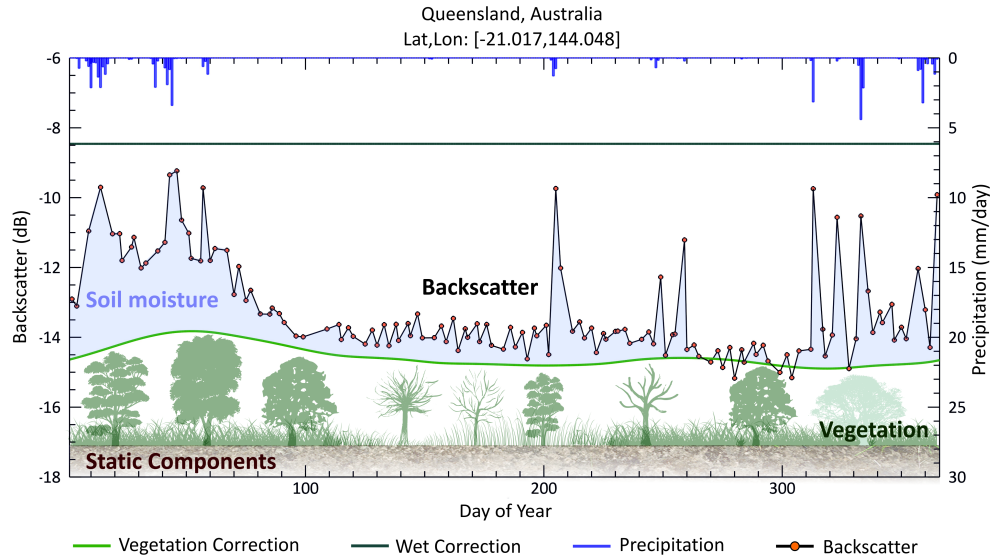


**Figure III.1:** The three components of the backscatter signal, the dry reference, wet reference and observed backscatter from the TU Wien change detection algorithm for a grid point in Queensland, Australia.

variations in leaf foliage. In addition, a preliminary study on comparing the  $\tau_p$  to the NDVI by Liu et al. (2011) found that the  $\tau_p$  and NDVI correspond better to each other over grasslands and croplands and less over shrublands and forests. Jones et al. (2013) looked at boreal forest recovery over Alaska, USA after wild fires. The NDVI indicated initial post-fire forest biomass recovery after 1 to 3 years, whereas this was 3 to 7 years for the  $\tau_p$ . Again the conclusion was that  $\tau_p$  is likely more closely related to the water content in the vegetations' leaves and woody compartment, whereas the NDVI is more sensitive to chlorophyll content and leaf area index. The previous studies demonstrated that  $\tau$  from microwave observations is a valuable parameter to describe vegetation characteristics which are complementary to NDVI and other related vegetation indices.

The use of remote sensing soil moisture products, including those retrieved with the TU Wien algorithm, has increased significantly in the last years, ranging from improved evaporation and rainfall modeling (Miralles et al., 2014; Brocca et al., 2014; Taylor et al., 2012) to trend analysis in droughts (Kuenzer et al., 2008; Dorigo et al., 2012) and land-atmosphere coupling models (Hirschi et al., 2014). Hence, a good understanding of the vegetation parameterization in the retrieval algorithms is imperative. Errors in vegetation parameterization can propagate to the final soil moisture product. Therefore, the aim of this study is to analyse the strengths and weaknesses of the existing vegetation correction in the TU Wien retrieval algorithm and its effect on the final soil moisture product. In order to quantify the ability of the vegetation correction to describe the vegetation, optical depth  $\tau_a$  is analytically retrieved from the vegetation correction using a water-cloud model. To assess the quality and physical meaning of this newly derived  $\tau_a$  it is compared to optical depth from AMSR-E,  $\tau_p$ , both in the spatial and temporal domain. After looking at the quality of the vegetation parameterization and identifying areas where problems with the soil moisture retrieval might arise, the effect of the vegetation correction on the final soil moisture product is assessed. For this, the surface soil moisture product before and after applying the vegetation correction term are compared to modeled soil moisture from ERA-Land, provided by ECMWF. Here, we especially focus on the effect that inter-annual variability in vegetation dynamics can have on the soil moisture retrieval.

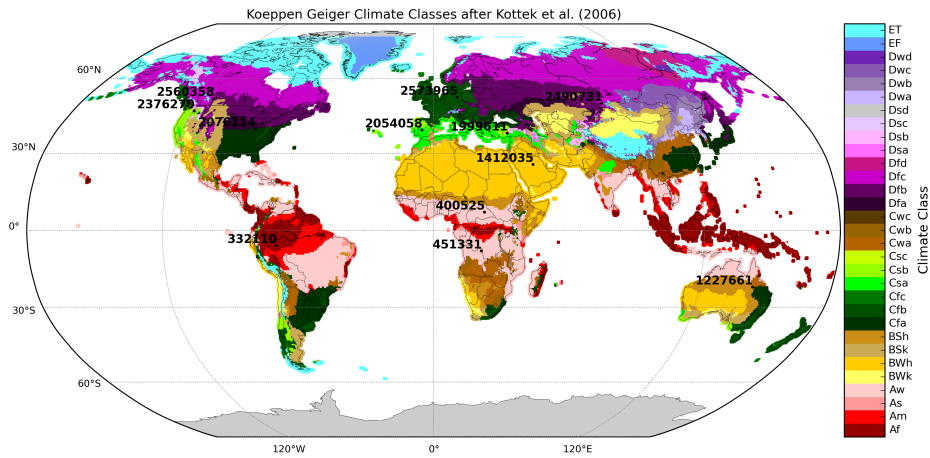


Figure III.2: Map of Koeppen Geiger climate classes with the gridpoint locations.

Table III.1: Koeppen Geiger climate classes after Kottek et al. (2006)

Climate	Type	Class (Precipitation)	Subclass (Temperature)
Equatorial Climate	Af	Rainforest	
	Am	Monsoon	
	As	Savannah with dry summer	
	Aw	Savannah with dry winter	
Arid Climate	BW	Desert	h = Hot arid
	BS	Steppe	k = Cold arid
Warm Temperate Climate	Cs	With dry summer	a = Hot summer
	Cw	With dry winter	b = Warm summer
	Cf	Fully humid	c = Cool summer
Snow Climate	Ds	With dry summer	d = Extremely continental
	Dw	Dry Winter	
	Df	Fully humid	
Polar Climate	ET	Tundra	
	EF	Frost	

## 2 Datasets

This section gives an overview and short summary of the existing datasets that are used in this study. The newly developed products are described in Section 3.

### 2.1 Metop-A ASCAT and TU Wien soil moisture retrieval

ASCAT is a scatterometer on board Metop-A and Metop-B, operative since 2006 and 2012 respectively. It measures vertically co-polarized backscatter at incidence angles ranging from 25° to 65° at a frequency of 5.25 GHz (C-Band). The Metop satellites fly in a sun-synchronous orbit, with morning and evening overpasses at approximately 09:30 and 21:30 local time. The individual ASCAT sensors provide a global coverage approximately every 2 days. The spatial resolution of ASCAT backscatter observations is 25 by 25 km. In the TU Wien retrieval algorithm, soil moisture is retrieved for every land gridpoint on a discrete global grid (WARP5 grid) with a spacing of ca. 12.5 km.

The TU Wien retrieval algorithm retrieves soil moisture time series with a change detection approach. One of the first steps in the algorithm is to normalize all backscatter observations taken over the entire incidence angle range to the reference incidence angle ( $\theta_r$ ) of 40°, resulting in the normalized backscatter  $\sigma^\circ(40)$ . The  $\sigma^\circ(40)$  is used to calculate soil moisture on a relative scale between the historically driest and wettest observed measurements, and during this scaling the vegetation correction of the TU Wien retrieval algorithm is applied. The vegetation in the TU Wien algorithm is described by way of the behaviour of the slope and curvature of the backscatter signature with regard to incidence angle. Backscatter from bare soils, as a result of surface scattering, decreases strongly with increasing incidence angle, whereas volume scattering, from e.g. vegetation, leads to more uniform backscatter values over all incidence angles (Fig. I.1). Hence, seasonal vegetation growth and decay changes the slope of the  $\sigma^\circ - \theta$  curve (Ulaby et al., 1984; Wagner et al., 1999a). The TU Wien algorithm uses this behaviour to account for the impact of vegetation on the backscatter signal: A change in soil moisture tends to shift the curve up and down in its entirety, while a change in vegetation or surface roughness changes the slope of the curve (Fig. I.1). For low incidence angles the vegetation tends to attenuate the signal from the soil surface, resulting in lower total backscatter than for bare soils. At higher incidence angles the backscatter is higher compared to bare soil conditions, due to volume scattering from the vegetation. There are incidence angles where the attenuation of the observed bare soil backscatter and the contribution from the vegetation are in equilibrium, the so-called cross-over angles (Fig. I.1). At the cross-over angles a change in backscatter is mainly a result of a change in soil moisture. These cross-over angles are dependent on the soil moisture being at a lower incidence angle for dry soils than for wet soils. In Wagner et al. (1999a) empirically estimated these cross-over angles to lie at 25° for dry soils and at 40° for wet soils. By converting the normalized backscatter observations to the 25° cross-over angle, the backscatter is only a function of soil moisture variations. To enable the retrieval of the historically driest soil conditions without the effect of vegetation attenuation or contribution, the so-called dry reference ( $\sigma_{dry}^\circ$ ), the normalized backscatter is converted to the 25° cross-over angle where the lowest backscatter observations are related to the historically driest soil conditions. The dry reference is retrieved for every gridpoint, converting all backscatter values from 40° to 25°, i.e.  $\theta = 25^\circ$  using a second-order Taylor expansion function:

$$\sigma^\circ(\theta, t) = \sigma^\circ(40, t) + \sigma_r'(40, DoY)(\theta - 40) + \frac{1}{2}\sigma_r''(40, DoY)(\theta - 40)^2 \quad (\text{III.1})$$

where  $\theta$  represents the incidence angle,  $\sigma_r'$  is the slope and  $\sigma_r''$  the curvature which are both averaged over several years and have one value for each day of the year (DoY). At  $\theta = 25^\circ$  the average over the lowest measurements is taken and this value is converted back to the reference incidence angle  $\theta = 40^\circ$  using the slope and curvature, with the Taylor expansion function. The

use of the cross-over angles and the Taylor expansion function integrate the variation of the slope, which is sensitive to vegetation water content and hence embeds a seasonal vegetation correction in the dry reference. The wet reference ( $\sigma_{wet}^\circ$ ) represents saturated soil conditions and is based on the historically wettest backscatter measurements at  $\theta = 40^\circ$ . Since  $\sigma^\circ$  is already normalized to  $\theta = 40^\circ$ , no conversion is needed to obtain the wet reference. Consequently, the wet reference is a constant value. In deserts it can occur that fully saturated soil conditions are not reached or captured by ASCAT. Hence, for deserts according to the Koeppen Geiger climate classification, the wet reference is corrected based on ASCAT observations in order to provide realistic soil moisture values. Soil moisture ( $\Theta_a$ ) is then calculated by scaling  $\sigma^\circ(40, t)$  between the dry and wet reference which are for this purpose matched from their Day Of Year to the date of the observation, as:

$$\Theta_a(t) = \frac{\sigma^\circ(40, t) - \sigma_{dry}^\circ(DoY)}{\sigma_{wet}^\circ(DoY) - \sigma_{dry}^\circ(DoY)}. \quad (III.2)$$

Soil moisture is retrieved on specific days for specific years, whereas the dry and wet reference are a product of the slope and curvature, for which only 366 values are available, i.e. one value for every day of the year. Consequently, the vegetation correction, which is intrinsically incorporated in the computation of the dry and wet reference and based on the slope and curvature, is not varying on an inter-annual basis. The difference between the  $\sigma_{dry}^\circ$  and  $\sigma_{wet}^\circ$  is the sensitivity ( $\Delta\sigma^\circ$ ) to changes in surface soil moisture content (Fig. III.1):

$$\Delta\sigma^\circ(DoY) = \sigma_{wet}^\circ(DoY) - \sigma_{dry}^\circ(DoY). \quad (III.3)$$

Since backscatter in dB has been found to be linearly related to soil moisture, and backscatter noise is independent of the absolute  $\sigma^\circ$  when expressed in dB, all the calculations within the TU Wien retrieval algorithm are done in the dB domain.

## 2.2 AMSR-E and the LPRM Vegetation Optical Depth ( $\tau_p$ ) retrieval

There are several  $\tau_p$  products available from passive microwave observations. In this research  $\tau_p$  retrieved from AMSR-E (Advanced Microwave Scanning Radiometer-Earth Observing System) passive microwave observations at 6.9 GHz with the VUA-NASA Land Parameter Retrieval Model is used. The VUA-NASA retrieval model is developed by the VU University Amsterdam in collaboration with NASA, and uses a radiative transfer model to solve for soil moisture and  $\tau_p$  simultaneously (Owe et al., 2001). In LPRM the  $T_b$  is represented by the following radiative transfer equation (Mo et al., 1982):

$$T_b = T_s e_r \gamma + (1 - \omega) T_c (1 - \gamma) + (1 - e_r) (1 - \omega) T_c (1 - \gamma) \gamma \quad (III.4)$$

, where  $T_s$  and  $T_c$  give the surface and canopy temperature,  $\omega$  represents the single scattering albedo,  $e_r$  gives the emissivity of the soil, and  $\gamma$  is given by:

$$\gamma = e^{-\frac{\tau}{\cos\theta}} \quad (III.5)$$

In LPRM  $T_s$  and  $T_c$  are assumed to be equal and  $T_s$  is separately retrieved from Ka-band observations according to Holmes et al. (2009).  $\tau_p$  is derived analytically directly from the  $\tau - \omega$  model (Meesters et al., 2005) and is the basis of LPRM. Using Eq. III.4, optical depth and soil emissivity are optimized against  $T_b$ . The soil emissivity is related to soil moisture using soil physical properties from FAO soil maps and a dielectric mixing model. In LPRM both roughness and the single scattering albedo are assumed to be constant.

The  $\tau_p$  is considered to be linearly related to the above-ground biomass water content, i.e. water content in the woody and non-woody components of the vegetation (Liu et al., 2013; Andela et al., 2013). Care needs to be taken when interpreting  $\tau_p$  data over areas with open water (Jones

et al., 2011) and with Radio Frequency Interference (RFI). Only ascending night-time observations are used in order to meet the assumption  $T_s = T_c$ . In addition,  $\tau_p$  is masked when the RFI flag  $> 2$ .  $\tau_p$  data cannot be computed when the soil is snow-covered or frozen.  $\tau_p$  data is available globally approximately every 2 days on a  $0.25^\circ$  grid.

In this study  $\tau_p$  time series from 2007 to 2011 are used. Since  $\tau_a$  is based on a climatology, averaged over several years of data, we computed the climatology of  $\tau_p$  by averaging the data for every Day Of Year (DOY) from 2007 to 2011. In addition, a smoothing with a window of 16 days was applied to better correspond to the  $\tau_a$ , which is calculated with a time window ranging from 2 to 12 weeks. Since the  $\tau_a$  is available on a  $12.5$  km discrete global grid (WARP5 grid) it was resampled to the spatial grid of  $\tau_p$ ,  $0.25^\circ$ , by taking the median of the  $\tau_a$  values of which the center of the gridpoint falls within a  $\tau_p$  gridpoint.

### 2.3 Ancillary Data

ERA-Land surface soil moisture ( $\Theta_{ERA}$ ) data from the European Centre for Medium Range Weather Forecasts (ECMWF) (Dee et al., 2011; Balsamo et al., 2013) is used as a reference to analyse the effect of the vegetation correction on the soil moisture retrieval. Soil moisture of the first soil layer (0-7 cm) was extracted for the period 2007-2011.  $\Theta_{ERA}$  is available every 6-hrs and daily means are calculated by averaging all observations within one day.

In addition, Global Land Data Assimilation System (GLDAS2-Noah) rainfall data at a  $0.25^\circ$  spatial sampling is used (Rodell et al., 2004) in the time series plots. The data is available on a 3-hourly interval and is resampled to daily average rainfall in mm for this study.

Results of the performed analysis are spatially compared to an updated Koeppen Geiger climate classification map from Kottke et al. (2006), based on temperature and precipitation observations for the period 1951-2000. An overview of the different Koeppen Geiger classes (KGC) can be found in Table III.1.

For the modeling of bare soil backscatter, soil data from the Harmonized World Soil Dataset (HWSD) are used (FAO/IIASA/ISRIC/ISSCAS/JRC, 2012). The HWSD provides standardized soil property data on a 1 km grid, based on regional and national data. In addition, percent tree cover data (Hansen et al., 2013) from Landsat images from the year 2000 is used to select non-vegetated areas. All data were resampled to the spatial resolution of AMSR-E,  $0.25^\circ$ .

## 3 Methods and Metrics

This section describes the methods that are used to retrieve new products, i.e. the optical depth from ASCAT observations, and the methods and metrics applied to assess the existing and newly derived products.

### 3.1 Vegetation optical depth retrieval ( $\tau_a$ ) from ASCAT observations

For the retrieval of optical depth from ASCAT backscatter observations we used the TU Wien retrieval algorithm and a water-cloud model (Attema and Ulaby, 1978; Ulaby et al., 1986; Wagner, 1998), which describes the total backscatter, in the power domain, as:

$$\sigma^\circ(\theta) = C \cdot \cos \theta (1 - \gamma^2) + \sigma_s^\circ(\theta) \gamma^2 \quad (\text{III.6})$$

where  $\sigma^\circ(\theta)$  and  $\sigma_s^\circ(\theta)$  represent the total backscatter coefficient and the backscatter coefficient of the soil surface in the power domain,  $C$  is a parameter related to the single scattering albedo  $\omega$ , which for small isotropic scatterers takes the value of  $3\omega/4$ , but in this case can take any value since it does not affect the final calculation of  $\tau_a$ .  $\gamma^2$  the two-way vegetation transmissivity is given as:

$$\gamma^2 = e^{-\frac{2\tau}{\cos\theta}} \quad (\text{III.7})$$

The first term on the right side of Eq. III.6 describes the contribution from the vegetation layer and the second term the soil surface contribution reduced by vegetation attenuation.

Optical depth from active microwave observations is calculated by ingesting the  $\sigma_{dry}^\circ$  and  $\sigma_{wet}^\circ$  (converted from dB to  $\text{m}^2 \text{m}^{-2}$ ), into the water-cloud model. Because the dry and wet references intrinsically incorporate changes in vegetation density, a change in sensitivity ( $\Delta\sigma^\circ$ ) is directly related to  $\tau_a$ , which can be mathematically illustrated using the water-cloud model by combining equations III.6 and III.7 and calculating the sensitivity  $\Delta\sigma^\circ$  in  $\text{m}^2 \text{m}^{-2}$ :

$$\begin{aligned} \Delta\sigma^\circ(D\sigma Y) &= (\sigma_{s,wet} - \sigma_{s,dry}) e^{-\frac{2\tau_a(D\sigma Y)}{\cos\theta}} \\ &= \Delta\sigma_s^\circ e^{-\frac{2\tau_a(D\sigma Y)}{\cos\theta}}. \end{aligned} \quad (\text{III.8})$$

which can be solved for  $\tau_a$  as:

$$\tau_a(D\sigma Y) = \frac{\cos\theta}{2} \ln \frac{\Delta\sigma_s^\circ}{\Delta\sigma^\circ(D\sigma Y)} \quad (\text{III.9})$$

where  $\Delta\sigma^\circ$ , in  $\text{m}^2 \text{m}^{-2}$ , is the sensitivity calculated from  $\sigma_{dry}^\circ$  and  $\sigma_{wet}^\circ$ , and  $\Delta\sigma_s^\circ$ , also in the linear domain, represents the maximum range in backscatter values over bare soils related to a change in soil moisture only and is assumed to be constant through time.  $\Delta\sigma_s^\circ$  cannot be retrieved directly but for this study is estimated from backscatter observations over non-vegetated areas and modeled using the latest version of the Integrated Equation Model (IEM) (Fung et al., 2002). The calculation of the  $\Delta\sigma_s^\circ$  and results are discussed in the next sections. Negative  $\tau_a$  values occur when  $\Delta\sigma^\circ$  exceeds  $\Delta\sigma_s^\circ$ . For these areas  $\tau_a$  is set to 0.  $\tau_a$  is available for every day of the year and is masked when no data for  $\tau_p$  is available to account for snow-covered or frozen soil.

### 3.2 Bare soil backscatter estimation and sensitivity analysis

In order to calculate  $\tau_a$  the sensitivity of backscatter to changes in soil moisture in bare soils needs to be estimated. As a first step we try to estimate this based on ASCAT observations by identifying areas which are not covered by any high vegetation and looking at the driest (lowest) measurements over these gridpoints during periods with minimum vegetation. Bare soil areas are classified as areas with a percent tree cover Hansen et al. (2013) of less than 10%, and optical depth values from AMSR-E of less than 0.20. A literature study is performed on studies that measured backscatter over bare soils to obtain an average value for the backscatter sensitivity to soil moisture changes. These studies demonstrate that sensitivity of backscatter to changes in soil moisture varies from about 5.5 dB to 10 dB depending on the change in soil moisture. These values for  $\Delta\sigma_s$  have been found for different sensor configurations, for a large diversity of soil types and root mean square heights of random soil roughness ( $s$ ) (Table III.2). This leads to our assumption that one value for  $\Delta\sigma_s^\circ$  can be set.

When  $\sigma_{s,dry}$  and  $\Delta\sigma_s^\circ$  in dB are known,  $\Delta\sigma_s^\circ$  can easily be calculated in  $\text{m}^2 \text{m}^{-2}$ , as follows:

$$\Delta\sigma_s^\circ[\text{dB}] = 10 \cdot \log \sigma_{s,wet} - 10 \cdot \log \sigma_{s,dry} \quad (\text{III.10})$$

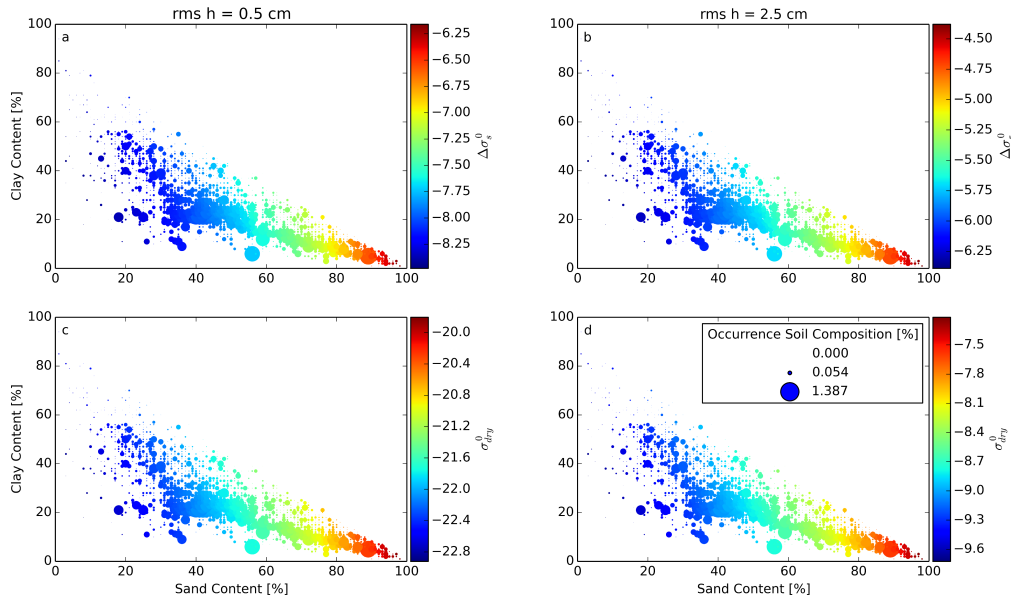
$$\begin{aligned} \Delta\sigma_s^\circ[\text{m}^2 \text{m}^{-2}] &= \sigma_{s,dry} \cdot 10^{\Delta\sigma_s^\circ[\text{dB}]/10} - \sigma_{s,dry}[\text{m}^2 \text{m}^{-2}] \\ &= (10^{\Delta\sigma_s^\circ[\text{dB}]/10} - 1) \cdot \sigma_{s,dry}[\text{m}^2 \text{m}^{-2}] \end{aligned} \quad (\text{III.11})$$

Table III.2: Bare soil backscatter and roughness measurements from literature

Sensor, Freq., inc. angle	$\sigma_{dry}^{\circ}$	$\sigma_{wet}^{\circ}$	$\sigma_s^{\circ}$	$\Delta\sigma_s^{\circ}$	$s$	sm [m <sup>2</sup> m <sup>-2</sup> ]	Landuse/Tillage	Study	
	[dB]		[m <sup>2</sup> m <sup>-2</sup> ]		[cm]				
MAS, 4.25GHz, 20°	-10	-2	8	0.7	4.1	<i>b</i>	ploughed bare soil	Ulaby and Batlivala (1976)*	
	-15	-7	8	0.16	1.1		dragged bare soil		
MAS, 4.25GHz, 10°	-	-	7.5	-	1.1 - 4.1	<i>b</i>	0.05 - 0.35	Ulaby and Batlivala (1976)	
MAS, 5.25GHz, 30°	-11	-1	10	0.71	4.1	<i>b</i>	chiseled bare soil	Ulaby et al. (1978)*	
	-17	-8	9	0.14	1.1		dragged bare soil		
SAR, 5.3GHz, 23°	-	-	5.5	-	0.5 - 2.5	<i>a</i>	0.05 - 0.3	rolled, harrowed, disked bare soil	Beaudoin et al. (1990)
SAR, 5.3GHz, 23°	-18	-8	10	0.14	0.2 - 0.5	<i>a</i>	0.05 - 0.35	planting row structure	Sano et al. (1998a)*
SAR, 5.3GHz, 23°	-7	0.5	7.5	0.92	-		0.05 - 0.40	bare soil	Moran et al. (2002)
-	-	-	-	-	0.49 - 3.43	<i>b</i>	-	pasture - bare soil	Bindlish and Barros (2000)
-	-	-	-	-	0.03 - 4.00	<i>a</i>	-	wheat sowing fields prepared three months earlier - ploughed bare soil	Baghdadi et al. (2002)
-	-	-	-	-	0.32 - 3.03	<i>c</i>	-	-	Oh et al. (1992)
-	-	-	-	-	0.02 - 0.90	<i>a</i>	-	natural grassland/pasture	Peischl et al. (2012)
-	-	-	-	-	0.20 - 2.45	<i>b</i>	-	bare soil	Wang et al. (1983)
-	-	-	-	-	0.70 - 4.70	<i>c</i>	-	rolled - ploughed	Davidson et al. (2000)
-	-	-	-	-	1.47 - 4.33	<i>a</i>	-	rolled seedbed - ploughed	Álvarez Mozos et al. (2009)
-	-	-	-	-	0.60 - 3.08	<i>a</i>	-	rangeland	Jackson et al. (1997)
-	-	-	-	-	0.64 - 1.99	<i>a</i>	-	rangeland	Sano et al. (1998b)

\* Estimated from figures

*a*: needle-pin profilometer*b*: photography/spraypainting*c*: laser profile



**Figure III.3:** The top two graphs (a and b) show  $\Delta\sigma_s^\circ$  in dB calculated using IEM and the lower two graphs (c and d) show the  $\sigma_{s,dry}^\circ$ . Where  $\sigma_{s,dry}^\circ$  and  $\Delta\sigma_s^\circ$  are calculated using the IEM for smooth (a and c) and rough (b and d) soil surfaces given by two root mean square heights:  $s = 0.5$  cm and  $s = 2.5$  cm. Data is displayed according to the global occurrence of soil properties: sand content (depicted on the x-axis) and clay content (depicted on the y-axis) by the size of the circles. The colorbar depicts the  $\sigma_{s,dry}^\circ$  and  $\Delta\sigma_s^\circ$  with low values in blue and high values in red.

Since there are limited non-vegetated gridpoints in tropical, temperate and cold climate classes, and experiments are mainly done with a different configuration than that of ASCAT,  $\sigma_{s,dry}^\circ$  and  $\Delta\sigma_s^\circ$  are also modeled using the Integral Equation Model (IEM) (Fung et al., 2002). The IEM is the most commonly used theoretical model for modeling backscatter from bare soils. It combines the Kirchhoff and Small Perturbation methods and is applicable to a large range of surface roughness scales and frequencies. It describes the backscatter behaviour of a random rough bare surface. A detailed description can be found in Fung et al. (2002). Since bare soil backscatter is sensitive to soil surface roughness and soil properties a range of root mean square heights of the surface have been used. To get representative average values for  $\sigma_{s,dry}^\circ$  and  $\Delta\sigma_s^\circ$ , backscatter is modeled for every gridpoint using the respective soil texture for that gridpoint. Subsequently, a global weighted average based on soil texture is calculated for  $\sigma_{s,dry}^\circ$  and  $\Delta\sigma_s^\circ$ . Only  $s$  is varied between  $s = 0.5$  cm and  $s = 2.5$  cm in the modeling, since soil moisture is more than ten times as sensitive to errors in  $s$  than correlation length (Lievens et al., 2009). Baghdadi et al. (2008) found correlation length to vary between 2 cm and 20 cm for agricultural fields. Based on these findings correlation length is kept constant, set to a value of 10 cm. Final values for  $\sigma_{s,dry}^\circ$  and  $\Delta\sigma_s^\circ$  are set based on observations and modeling.

Furthermore, to take into account the effect of  $\Delta\sigma_s^\circ$  on the resulting  $\tau_a$ , a perturbation model is applied to demonstrate the sensitivity of  $\tau_a$  to  $\Delta\sigma_s^\circ$ . The sensitivity of  $\tau_a$  to perturbation  $1+\epsilon$  is given as:

$$\tau_a(\Delta\sigma_s^\circ \cdot (1 + \epsilon)) = \frac{\cos \theta}{2} \ln \frac{\Delta\sigma_s^\circ \cdot (1 + \epsilon)}{\Delta\sigma_s^\circ} \quad (\text{III.12})$$

, which can be rewritten as:

$$\tau_a(\Delta\sigma_s^\circ \cdot (1 + \epsilon)) = \frac{\cos \theta}{2} \ln \frac{\Delta\sigma_s^\circ}{\Delta\sigma_s^\circ} + \frac{\cos \theta}{2} \ln(1 + \epsilon) \quad (\text{III.13})$$

The change in  $\tau_a$  as a function of the perturbation  $\epsilon$  can be defined as:

$$\begin{aligned}\delta\tau_a &= \tau_a(\Delta\sigma_s^\circ \cdot (1 + \epsilon)) - \tau_a(\Delta\sigma_s^\circ) \\ &= \frac{\cos\theta}{2} \ln(1 + \epsilon) \\ &= \frac{\cos\theta}{2} \ln\left(1 + \frac{\delta\Delta\sigma_s^\circ}{\Delta\sigma_s^\circ}\right)\end{aligned}\quad (\text{III.14})$$

In order to look at a valid range of  $\Delta\sigma_s^\circ$  maximum bare soil backscatter values are set based on Ulaby and Batlivala (1976), Ulaby et al. (1978) and Sano et al. (1998a). In these studies backscatter was measured either with a field scale radar or spaceborne SAR. Observations at 5.25 GHz at VV and HH polarization over bare soils with different roughness and soil moisture values were used. The findings of these studies are summarized in Table III.2. Based on these results the minimum and maximum  $\Delta\sigma_s^\circ$  were estimated to  $0.05 \text{ m}^2 \text{ m}^{-2}$  and  $0.7 \text{ m}^2 \text{ m}^{-2}$  respectively.

### 3.3 Metrics used for assessing $\tau_a$ and $\Theta_a$

The Spearman Rank correlation coefficient ( $r_s$ ) is calculated between the climatologies of  $\tau_a$  and  $\tau_p$ .  $r_s$  is based on a relative ranking of the data, not on absolute values, and does not make any assumption on the nature of the relationship between the different datasets.

To assess the effect of the TU Wien vegetation correction on the soil moisture retrieval both the normalized backscatter  $\sigma^\circ(40)$  (Eq. III.2, right hand term) and the surface soil moisture  $\Theta_a$  Eq. (III.2, left hand term) were correlated with  $\Theta_{ERA}$ . The  $\sigma^\circ(40)$  is not yet corrected for vegetation whereas the  $\Theta_a$  is. With this analysis the impact of the vegetation correction on the quality of  $\Theta_a$  can be identified. However, with this analysis we only investigate how the vegetation correction improves the temporal dynamics of the soil moisture retrieval. How the vegetation correction impacts the absolute values of soil moisture is not investigated with this approach although it is expected to be significant.

To test the impact of the existing fixed year-to-year vegetation correction, the dry reference, which incorporates the existing vegetation correction, was substituted by the  $\tau_p$  to produce a soil moisture product with an inter-annually varying vegetation correction ( $\Theta_{\tau_p}$ ):

$$\Theta_{\tau_p}(t) = \frac{\sigma^\circ(40, t) - \sigma_{dry}^\circ(t, \tau_p)}{\sigma_{wet}^\circ(t) - \sigma_{dry}^\circ(t, \tau_p)} \quad (\text{III.15})$$

$\sigma_{dry}^\circ(t, \tau_p)$  is the new dry reference based on  $\tau_p$  from AMSR-E scaled to the dry reference (in dB) with a mean-standard deviation scaling as follows:

$$\sigma_{dry}^\circ(t, \tau_p) = \frac{\tau_p(t) - E[\tau_p(t)]}{\text{Sd}[\tau_p(t)]} \text{Sd}[\sigma_{dry}^\circ(DoY)] + E[\sigma_{dry}^\circ(DoY)] \quad (\text{III.16})$$

, where E and Sd are the mean and standard deviation. The mean and standard deviation scaling is purely to scale the  $\tau_p$  values to the dry reference values which are in dB. The whole time series of  $\tau_p$  is used to calculate the respective mean and standard deviation. The goal of this is to introduce inter-annual variability in the vegetation correction and subsequently in the soil moisture retrieval. As a consequence, the results only provide information on the differences in the temporal behaviour of soil moisture and not absolute values. Because of the scaling of  $\tau_p$  to the mean and standard deviation of the dry reference, absolute values of soil moisture are not expected to change dramatically.

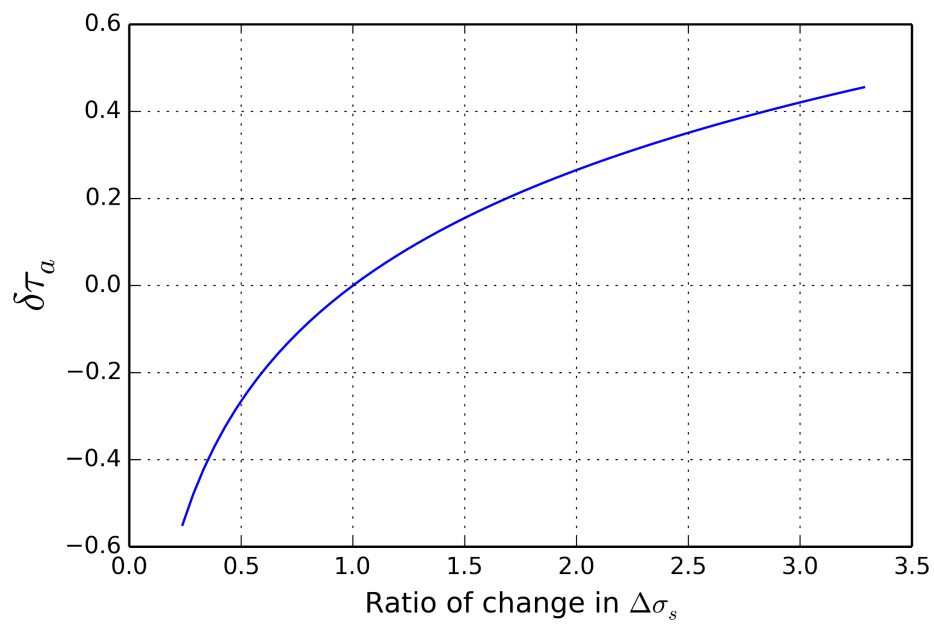


**Figure III.4:** Sensitivity of  $\tau_a$  to a change in surface scattering  $\Delta\sigma_s^\circ$  as given by (III.14), with the ratio of change on the x-axis.

## 4 Results and Discussion

### 4.1 Effect of bare soil backscatter on $\tau_a$ retrievals

Only a limited number of gridpoints satisfied the conditions of Hansen tree cover less than 10% and  $\tau_p$  less than 0.20. For all land surface areas, 17.8% of the gridpoints are classified as bare soils, of which only 5.4% are in climate classes which are not deserts. This fraction of bare soils was found in the Great Plains and Canadian prairies. The low fraction of bare soils in non-deserts resulted in two different methods to estimate  $\Delta\sigma_s^\circ$ ; one for deserts and one for all other areas, here referred to as non-desert areas. For every gridpoint in deserts it is assumed that the lowest measurements are not affected by vegetation. Hence, the lowest backscatter measurements are taken as  $\sigma_{s,dry}^\circ$ . For deserts the  $\sigma_{s,dry}^\circ$  varies per gridpoint based on ASCAT observations. For all non-desert areas results are averaged to one value in order to obtain a representative value of  $\sigma_{s,dry}^\circ$ . The variability in  $\sigma_{s,dry}^\circ$  is clearly represented in the standard deviation per climate class (Table III.3). For climate classes A, BS, C and D the standard deviation ranges from 1.67 dB to 2.70 dB, whereas the standard deviation in climate class BW is as high as 4.6 dB.  $\sigma_{s,dry}^\circ$  ranges from -27.01 dB to -3.71 dB for temperate climates (class C) and from -21.91 dB to -8.59 dB for cold climates (class D). For deserts  $\sigma_{s,dry}^\circ$  is highly variable, with values ranging from -37.78 dB to -5.89 dB. The variability is much higher than for non-desert areas, confirming the importance of a variable  $\sigma_{s,dry}^\circ$ . Averaging all results from gridpoints located within climate classes A, BS, C, D and E yields an average  $\sigma_{s,dry}^\circ$  of -15.23 dB. Based on the literature review (Table III.2) the  $\Delta\sigma_s^\circ$  is set to a single value of 8 dB. Inserting the average  $\sigma_{s,dry}^\circ$  for non-desert areas and the estimate of  $\Delta\sigma_s^\circ$  into Eq. III.12 leads to a  $\Delta\sigma_s^\circ$  of  $0.16 \text{ m}^2 \text{ m}^{-2}$  for non-desert areas. This value is similar to the value found for relative smooth soils from the literature review, e.g.  $1.1 > s > 0.2 \text{ cm}$  (Table III.2).

Fig. III.3 shows the results from the IEM modeling for  $\sigma_{s,dry}^\circ$  and  $\Delta\sigma_s^\circ$  for using a  $s$  of 1 cm and 2.5 cm. Results are shown according to the respective occurrence of combinations of sand and clay content as derived from the FAO soil map. We have chosen to calculate a weighted average based on occurring soil textures, in order to obtain more representative values for  $\sigma_{s,dry}^\circ$  and  $\Delta\sigma_s^\circ$ . Results are summarized for all values of  $s$  in Table III.3. Comparing the values obtained from ASCAT observations and the literature study to modeled results of the analyses using IEM, confirms that the obtained value of  $0.16 \text{ m}^2 \text{ m}^{-2}$  is characteristic for relatively smooth soils. modeling yields  $\sigma_{s,dry}^\circ$  values ranging from -23.01 dB for smooth soils with a  $s = 1 \text{ cm}$  (Fig. III.3.c), to -7.17 dB for rough soils with a  $s = 2.5 \text{ cm}$  (Fig. III.3.d). The values for  $\Delta\sigma_s^\circ$  were found to range from -8.54 dB for smooth soils (Fig. III.3.a) to -4.38 dB for rough soils (Fig. III.3.b). The modeling yields smaller values for  $\Delta\sigma_s^\circ$  than the literature study. This can be explained by the fact that most studies assessed in the literature review, use backscatter observed under an incidence angle lower than the  $40^\circ$  angle of ASCAT. The sensitivity of backscatter to soil moisture decreases with increasing incidence angles (Ulaby and Batlivala, 1976; Ulaby et al., 1978; Baghdadi et al., 2002), explaining the lower  $\Delta\sigma_s^\circ$  from the modeling at  $40^\circ$ .  $\Delta\sigma_s^\circ$  of 8 dB is on the high end of results from the IEM modeling, i.e.  $\Delta\sigma_s^\circ$  around 8 dB are only found for  $s = 0.5 \text{ cm}$ .

Based on the modeling study we can conclude that the estimated values for  $\sigma_{s,dry}^\circ$  and  $\Delta\sigma_s^\circ$ , based on observations and a literature review, is associated to smooth soils with  $s \simeq 1 \text{ cm}$ . Assuming that land use over tropical, temperate and cold climates is mainly either agriculture, tundra or forest, average microscale random roughness conditions for these surfaces are likely higher than  $s = 1 \text{ cm}$ . Subsequently,  $\sigma_{s,dry}^\circ$  in dB and  $\Delta\sigma_s^\circ$  in  $\text{m}^2 \text{ m}^{-2}$  are likely higher than calculated from ASCAT observations over the bare soil areas in the Canadian Prairies and Great Plains. Jackson et al. (1997) and Davidson et al. (2000) stated that 1.5 cm and 1.6 cm are most representative for typically observed normal conditions of roughness. Considering the results from the data analysis, the literature review and the modeling, the  $\Delta\sigma_s^\circ$  in  $\text{m}^2 \text{ m}^{-2}$  for non-deserts calculated from observations was adjusted. For the ultimate calculation of  $\tau_a$ ,  $\Delta\sigma_s^\circ$  is set to the modeled value for

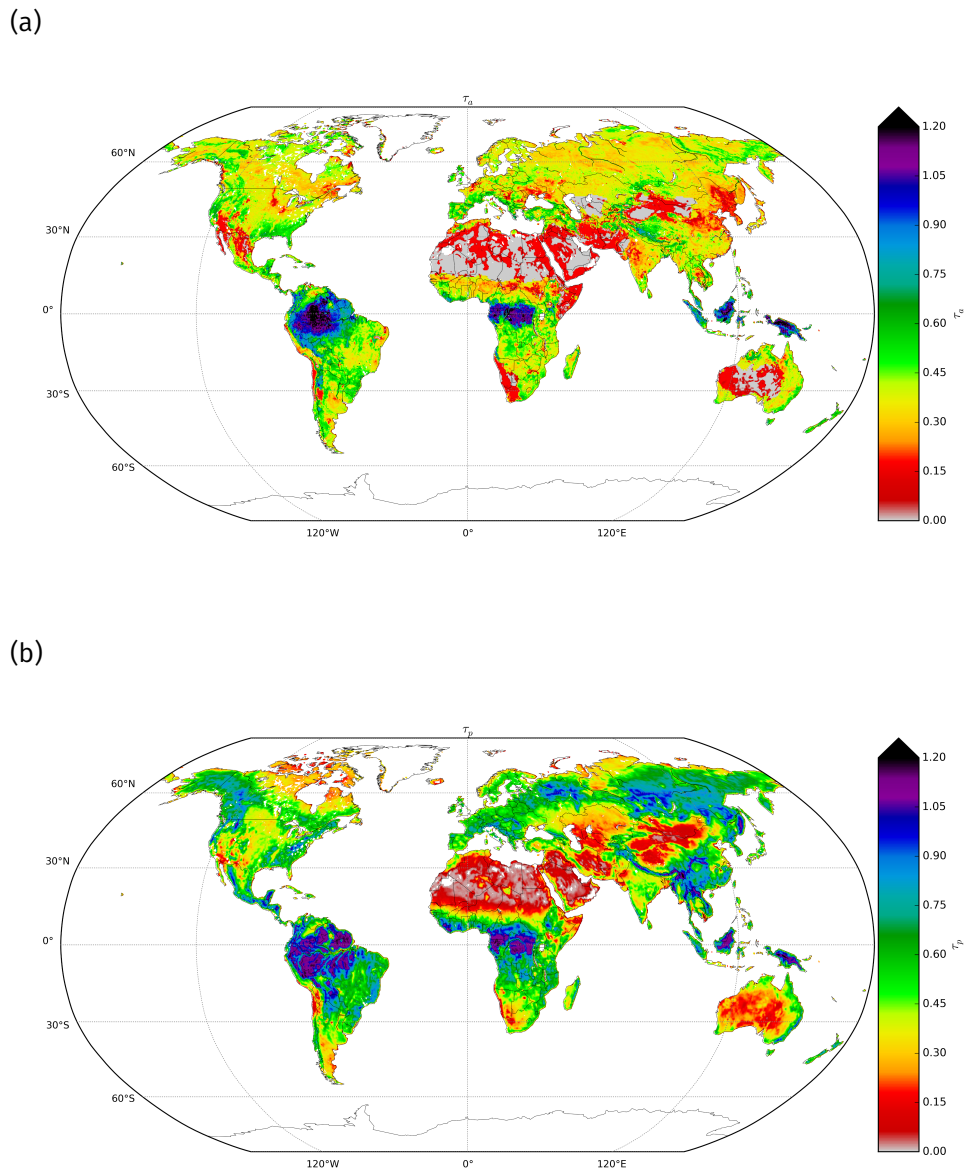


Figure III.5: Global map of mean  $\tau_a$  (a) and  $\tau_p$  (b) calculated over the period from 2007 to 2011.

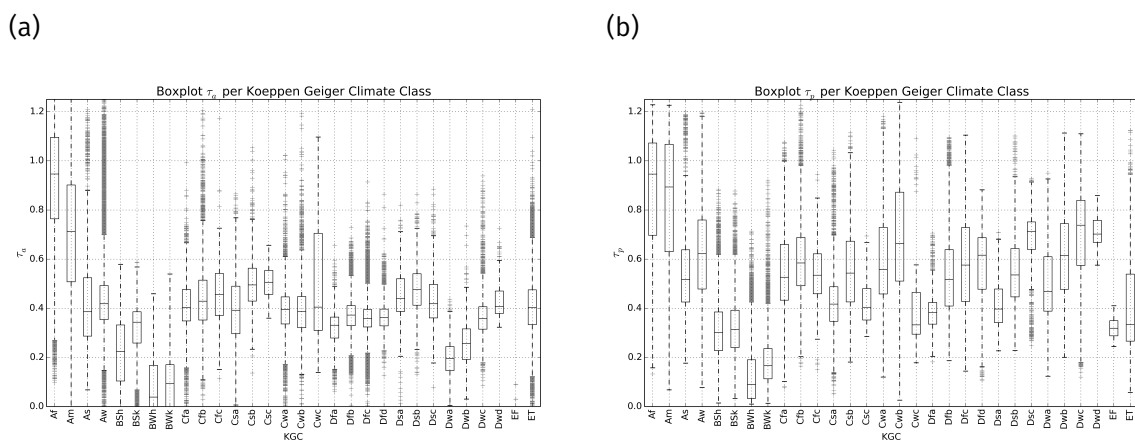


Figure III.6: Boxplots of  $\tau_a$  (a) and  $\tau_p$  (b) per Koeppen Geiger climate class.

**Table III.3:** Bare soil backscatter and  $\Delta\sigma_s^\circ$  from data and modeling

Source	KGC	$\sigma_{dry}^\circ$ [dB]			$\Delta\sigma_s^\circ$ [dB]			$\Delta\sigma_s^\circ$ [m <sup>2</sup> m <sup>-2</sup> ]
		min	max	mean	min	max	mean	
ASCAT data	A	-18.29	-6.14	-12.29				0.31
	BS	-26.49	-8.35	-16.25				0.13
	BW	-37.78	-5.89	-16.93				0.10
	C	-27.01	-3.71	-13.15				0.26
	D	-21.91	-8.59	-16.79				0.11
	average	-27.01	-3.71	-15.23				0.16
Source	s [cm]	$\sigma_{dry}^\circ$ [dB]			$\Delta\sigma_s^\circ$ [dB]			$\Delta\sigma_s^\circ$ [m <sup>2</sup> m <sup>-2</sup> ]
		min	max	mean	min	max	mean	
IEM	0.5	-23.01	-19.74	-21.74	-8.52	-6.11	-7.71	0.03
	1.0	-16.40	-13.51	-15.27	-7.30	-5.09	-6.54	0.10
	1.5	-12.64	-9.90	-11.55	-6.77	-4.67	-6.06	0.21
	2.0	-10.57	-7.88	-9.50	-6.54	-4.46	-5.82	0.32
	2.5	-9.80	-7.16	-8.76	-6.43	-4.34	-5.69	0.36
	average	-23.01	-7.17	-13.37	-8.52	-4.34	-6.37	0.15

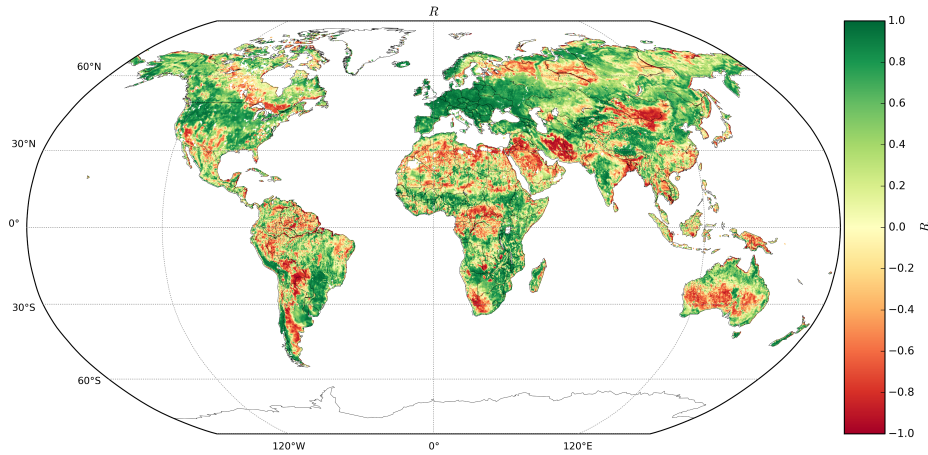


Figure III.7: Global  $r_s$  between  $\tau_a$  and  $\tau_p$ .

$s = 1.5$  cm:  $0.21 \text{ m}^2 \text{ m}^{-2}$ . For deserts  $\Delta\sigma_s^\circ$  is lowered to the weighted average of the IEM analyses:  $-6.37$  dB. This leads to the following values being used for  $\Delta\sigma_s^\circ$ :

$$\Delta\sigma_s^\circ = \begin{cases} 0.21 & KGC = A|BS|C|D|E \\ (10^{6.37[\text{dB}]/10} - 1) \cdot \sigma_{s,dry}^\circ(x,y), & KGC = BW \end{cases}$$

where units are  $\text{m}^2 \text{ m}^{-2}$  unless stated otherwise and for climate class BW,  $\sigma_{s,dry}^\circ$  varies spatially for every gridpoint, denoted with the suffix  $(x,y)$ .

When calculating  $\tau_a$ , the bare soil backscatter  $\Delta\sigma_s^\circ$  is assumed to be static for all areas apart from deserts. This very likely introduces spatial biases in  $\tau_a$ , because the range of surface roughness conditions changes from pixel to pixel and is not accounted for. The sensitivity analyses assesses the effect of  $\Delta\sigma_s^\circ$  on  $\tau_a$ . Fig. III.4 shows for decreasing  $\Delta\sigma_s^\circ$  from the estimated average value of 0.21 to 0.05 will lead to a decrease in  $\tau_a$  of 0.55, whereas increasing  $\Delta\sigma_s^\circ$  to 0.7 will increase  $\tau_a$  with 0.46. However, it needs to be taken into account that the sensitivity analysis is performed using extreme values. Smooth soils or ploughed soils as prepared for the experiments described in Section 3.2 are rare and unrealistic to span the entire extent of a pixel. Taking into account the natural conditions of the soils a pixel of ASCAT will not solely contain recently ploughed soils or only smooth soils, but is a mix of different states of soil surface roughness. Furthermore, one needs to keep in mind that how soil surface roughness affects satellite scale observations is not yet well understood. Field-scale surface roughness as measured during experiments, parameterized by two variables, is not assumed to be representative for the effective surface roughness at the satellite scale (Verhoest et al., 2008). Taking this into account, one can assume that soil surface roughness is unlikely to reach extreme values of e.g. 0.05 cm or 4 cm over a whole pixel of ASCAT. A decrease of  $\Delta\sigma_s^\circ$  happens in relatively smooth soils (Fig. III.3 and Ulaby and Bativala (1976)) e.g. soils with a lower microscale roughness, which are expected to be in natural areas like deserts, savannah and rangeland. However, for most of these areas, which fall in climate class B,  $\Delta\sigma_s^\circ$  is estimated at every gridpoint from the ASCAT data. The analysis demonstrates that for areas where  $\tau_a$  gives lower values compared to  $\tau_p$  the estimated  $\Delta\sigma_s^\circ$  might be too low. Considering that  $\Delta\sigma_s^\circ$  of  $0.21 \text{ m}^2 \text{ m}^{-2}$  is found in relatively smooth soils, i.e.  $s = 1.5$ cm, this estimate could be too low for soils with a higher surface roughness. Even though the estimation of  $\Delta\sigma_s^\circ$  clearly introduces a bias, the spatial distribution and temporal variability of  $\tau_a$  still gives valuable information on how the TU Wien model describes the vegetation and makes it comparable to  $\tau$  values derived from other sensors. In the following sections the results are discussed in general and per climate class.

## 4.2 Comparing $\tau_a$ and $\tau_p$

Fig. III.5 and III.6 show the global maps and boxplots per Koeppen Geiger climate class of both  $\tau_a$  and  $\tau_p$  average values over the period 2007 to 2011. When looking at the spatial distribution of the mean values of  $\tau_a$  and  $\tau_p$ , spatial patterns are similar, especially over tropical forests, southern Europe and North-America. As the boxplots show (Fig. III.6), for both products  $\tau$  values decrease from values close to 1.0 for climate class Af to values between 0.4 and 0.6 for climate classes Am and As to values close to 0 for climate classes BWh and BWk. Higher values are found in climate class C, with lowest values in classes that are characterized by a hot summer, identified by the suffix 'a' in the climate class classification, indicating drier conditions and a lower vegetation density. In cold climates especially areas with dry winters (Dw) show very similar patterns with increasing values for both  $\tau_a$  and  $\tau_p$  with decreasing summer temperatures. The clear spatial patterns in  $\tau_a$  demonstrate that the assumption of a spatially constant  $\Delta\sigma_s^\circ$  for non-desert areas is reasonable to obtain a first estimate of  $\tau_a$ . In general, values for  $\tau_a$  are 0.15 lower than values found for  $\tau_p$ . A potential explanation for this is that  $\Delta\sigma_s^\circ$  is estimated too low.  $\Delta\sigma_s^\circ$  could be too low due to the relatively large correlation length that has been used in the IEM modeling. Lowering the correlation length to the average value found by Davidson et al. (2000) would increase  $\tau_a$  by 0.08, bringing it closer to the values found for  $\tau_p$ . On top of this,  $\tau_a$  shows particularly lower values in cold climates, i.e. northern Europe, Russia and North-America. The comparison of absolute values of  $\tau_a$  and  $\tau_p$  are discussed in detail in the following subsections.

Fig. III.7 shows the results of the  $r_s$  between the climatologies of  $\tau_a$  and  $\tau_p$ . The boxplots (Fig. III.8) show the distribution of  $r_s$  per Koeppen Geiger climate class. High values of  $r_s$  are observed over temperate and cold climates (climate classes C and D). In deserts and drylands (climate class BWh and BWk) clearly negative  $r_s$  values are observed. Fig. III.9 shows the climatologies of  $\tau_a$  and  $\tau_p$  for nine gridpoints with different land cover and in different climate classes (see Fig. III.2 for locations). Intra-annual variability is in general low for  $\tau_a$  (around 0.1) and for most gridpoints lower than for  $\tau_p$ .

### Equatorial regions (KGC: A)

In tropical climates both  $\tau_a$  and  $\tau_p$  show distinctively high values (Fig. III.5), i.e. climate class A, can be easily distinguished with the median values from 0.44 to 0.99 (Fig. III.6). Average values for climate class Af, Rainforests respectively, agree very well with each other. However, values for  $\tau_p$  are on average 0.17 higher in monsoon areas (Am) and savannah (As) than  $\tau_a$ , which is close to the overall bias found between  $\tau_a$  and  $\tau_p$ . The temporal comparison between  $\tau_p$  and  $\tau_a$  in tropical climates shows both weak negative and weak positive  $r_s$  values. The cause for these mixed weak  $r_s$  values is the small intra-annual variability for both  $\tau_a$  and  $\tau_p$  (Fig. III.9a). The same conclusion was drawn by Liu et al. (2011) who found a low intra-annual variability in  $\tau_p$ . It needs to be considered that the  $r_s$  is not the appropriate metric in regions with low variation of the signal. A more suited metric is the Mean Squared Error (MSE) (Fig. III.10), as calculated in Su et al. (2013), which is a function of the correlation coefficient, the standard deviation and the mean of the time series. Looking at the MSE between  $\tau_p$  and  $\tau_a$  over tropical rainforests and deserts the MSE does not show distinctly higher values than in other regions. Hence, it supports the assumption that the low  $r_s$  values are caused by the minimal variation in  $\tau_p$ .

Fig. III.7 and III.10 show negative  $r_s$  and high errors in some regions belonging to class Aw (equatorial climate with dry winter), i.e. north of the African tropical rainforest, over Cameroon, Central African Republic and South Sudan. When looking at the MSE (Fig. III.10) it shows that this area is characterized by relatively high MSE:  $MSE > 0.10$ . The time series plots (Fig. III.9c) show little variation in  $\tau_a$ , but the highest value lies around February, whereas  $\tau_p$  has its minimum at this time, which coincides with the end of the dry season. Only from July to October both  $\tau_a$  and  $\tau_p$  increase, the rest of the year the behaviour of the time series is opposite here, where  $\tau_a$  also

does not follow the precipitation regime. The different behaviour of  $\tau_a$  and  $\tau_p$  is subject to further investigation.

### Arid regions (KGC: B)

In arid climates, e.g. deserts, climate class B,  $\tau_a$  and  $\tau_p$  show low values, between 0.0 and 0.39. Values here correspond very well to each other with almost no bias between the two products for climate classes BSh and BSk, i.e. bias = 0.04. For deserts (climate classes BWh and BWk) the bias between the two products is larger, where  $\tau_a$  is on average 0.21 lower than  $\tau_p$ . This originates mainly from areas where backscatter is extremely low, e.g. in sand dunes, and  $\tau_a$  shows values close to 0 or even negative.  $\Delta\sigma_s^\circ$  is extremely low in sand dunes, e.g. -32 dB, since it is obtained for every gridpoint individually based on ASCAT observations, leading to  $\tau_a$  values of 0. Spatial patterns between  $\tau_a$  and  $\tau_p$  are very similar in deserts, with higher values in Yemen and in mountainous areas in the Sahara desert. Even though the mean values of the two products correspond well to each other, negative values for  $r_s$  are observed between  $\tau_a$  and  $\tau_p$ . Previous studies have shown that the  $\tau_p$  shows a good correspondence to both precipitation and NDVI over these regions (Andela et al., 2013; Liu et al., 2011). Multiple processes can play a role in deserts, introducing discrepancies and low correspondence between  $\tau_a$  and  $\tau_p$ . Most importantly, as for tropical forest, variation in vegetation is very low in most parts of deserts (Fig. III.9e). In fact, many areas do not have any vegetation at all (Fig. III.9f). Consequently,  $r_s$  between  $\tau_a$  and  $\tau_p$  is meaningless for some areas. In these areas the  $\tau_a$  and  $\tau_p$  signal do not correspond to vegetation water content but are sensitive to other surface parameters.

For example, soil volume scattering, can play a role in deserts (Matzler, 1998), caused by dry sand soils. In wet soils, microwaves do not penetrate the soil very deep, since the soil moisture forms a dielectric surface, hence volume scattering does not need to be taken into account. However, studies have demonstrated that in dry sand soils, the penetration depth of the microwaves can be large, i.e. up to several meters, causing volume scattering (Matzler, 1998) and the chance of hitting subsurface bedrock. Since volume scattering is also the prevailing scattering mechanism in vegetation, volume scattering due to dry soils can cause an increase in  $\tau_a$  when no vegetation is present.

When microwaves do hit subsurface bedrock or rocks  $\tau_a$  is also affected. Rocks and bedrock patterns at the same scale as the wavelength of ASCAT can increase the microscale surface roughness of the scattering surface. Since the effect on the slope and curvature of the  $\sigma^\circ - \theta$  curve is the same for increasing surface roughness as for increasing vegetation density, i.e. the slope of the  $\sigma^\circ - \theta$  curve decreases with increasing soil surface roughness (Ulaby et al., 1978), increasing microscale roughness can increase  $\tau_a$ . Rocky surfaces can be found in desert pavements, pediments and regolithic slopes. Pavements are flat surfaces, formed by long-term aeolian erosion, with pebbles and cobbles on the (sub)surface. Pediments form at the foot of mountainous areas, and are characterized by eroded bedrock surfaces covered with pebbles. Since weathering in deserts is a mechanical process, and not driven by water, it results in coarse angular rocks with the size of pebbles (2 - 6.4 cm) and cobbles (6.4 - 25.4 cm) covering many areas in deserts (Skinner et al., 2004; Nichols, 2009). With a wavelength of 5 cm, C-Band is highly sensitive to the presence of pebbles and cobbles on the surface or in the subsurface, increasing  $\tau_a$ . In addition, buttes are distinctive landforms in deserts, which consist of steep-sided hills and cliffs (Skinner et al., 2004), which can function as corner reflectors, leading to higher backscatter and potentially increasing  $\tau_a$ . Here it needs to be considered that surface roughness is difficult to define in microwave remote sensing, and represents the roughness of the boundary between two media with different dielectric properties. If during dry periods volume scattering or scattering from subsurface bedrock is the dominant mechanism a high  $\tau_a$  is observed, leading to negative  $r_s$  values. Furthermore, the signal to noise ratio is very low in deserts, which makes a change detection very challenging. In conclusion, not considering the generally low vegetation density and dynamics in deserts, the variation observed in  $\tau_a$  can be originating from sensor noise, surface roughness changes, volume scatter-

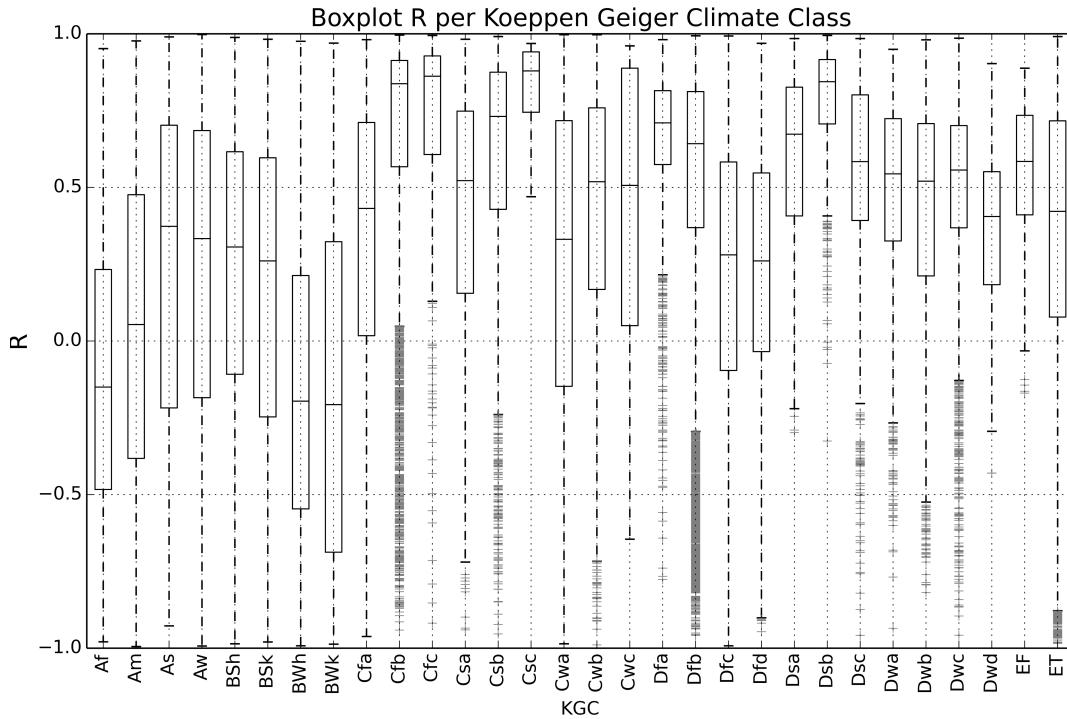


Figure III.8: Boxplot of the  $r_s$  per Koeppen Geiger climate class for  $\tau_a$  and  $\tau_p$ .

ing, a wrong estimation of the wet reference or some yet unknown physical process, possibly explaining the high values for  $\tau_a$  and low  $r_s$  with  $\tau_p$ .

### Warm temperate regions (KGC: C)

Temperate regions cover parts of Europe, Argentina, eastern China and the USA, and are dominated by croplands. In general,  $\tau_a$  shows lower values for temperate climates than  $\tau_p$ , with an average bias of 0.15. This bias originates mainly from climate classes Cwa and Cwb, temperate climates with a dry winter and hot and warm summer. Climate class Cwa covers part of the Himalaya mountains and mountainous regions in China, excluding the Tibetan Plateau which falls in climate class ET, where retrieval is potentially hampered due to the rough terrain. Analysis of RADARSAT2 observations over the Italian Alps showed a difference in backscatter values of 8 to 9 dB attributed to extreme topography (Pasoli et al., 2011). Even though backscatter is normalized for topography in the TU Wien retrieval algorithm, extreme topography, as found in the Himalayas can still cause ambiguity in backscatter observations and thus in  $\tau_a$ . When looking at spatial patterns and mean values of  $\tau_a$  and  $\tau_p$ , they are similar in southern Europe and the southern USA. In southern Europe higher values are found for both  $\tau_p$  and  $\tau_a$  in northern Spain, around the Mediterranean and the coastal regions of Turkey. For both products the inland of Turkey and Iran show lower values than the coastal areas. Also over North-America similar patterns are found, with low values in the south-eastern part of the USA and higher values in the north-western part. Fig. III.6 shows that for temperate climates both products show lower values in regions with hot summers, i.e. Cfa, Csa, Cwa. Both  $\tau_p$  and  $\tau_a$  are increasing with decreasing summer temperatures, demonstrated by the increasing averages from e.g. Cfa to Cfc.

$r_s$  values between  $\tau_a$  and  $\tau_p$  are very high for temperate climate regions (Fig. III.6, III.7 and III.9h-l). This is demonstrated by the high values for  $r_s$  of  $> 0.7$  (Fig. III.8) in KGC classes C. For temperate climates with hot summers, i.e. class Cfa, Csa, Cwa,  $r_s$  is lower than for the other temperate classes, which have a median  $r_s < 0.5$ . One explanation for this may be volume

scattering, as described in the section on arid regions, taking place in summer when soils are very dry. Especially, in Spain and in the south-east of the USA this has been observed, where high backscatter values occur in dry periods (Wagner et al., 2014, 2013). In some cases, total backscatter only decreases after the occurrence of a rain-event. Due to the rainfall event the main scattering mechanism shifts from volume scattering to surface scattering, decreasing the  $\tau_a$ .

### Cold regions (KGC: D)

In cold climates (climate class D), characterized by tundra, taiga and forests,  $\tau_a$  shows lower values compared to  $\tau_p$ , especially over Canada, Alaska and Russia. The average bias between  $\tau_a$  and  $\tau_p$  is higher here than for all other climate classes, i.e. 0.21. This bias originates mainly from climate class Dfc and Dwc, cold climates with cool summers and either dry summers or dry winters, and these classes cover mainly boreal forests and taiga. There are different reasons that might explain this phenomenon. First, the estimated sensitivity of bare soil backscatter  $\Delta\sigma_s^\circ$  may be too low, e.g. because increasing vegetation cover increases the soil surface roughness, e.g. by the presence of litter on the surface and roots in the subsurface. However, we do not see these particularly low values, e.g. the median negative bias for climate classes Dfc and Dwc is close to 0.5, for  $\tau_a$ , in other forested areas, which would be the case if the problem would lie with the  $\Delta\sigma_s^\circ$  estimation. Another, more likely reason, could be a bias in the estimation of the dry reference. Additional analysis during this study revealed that the wet reference,  $\sigma_{wet}^\circ$ , shows very little variation between climate classes A, BS, C and D with an overall mean and standard deviation of 0.47 and 0.96 respectively. When comparing subclasses with similar  $\tau_p$  values from climate classes A and D the dry reference in climate classes Dfc and Dwc is on average 3 dB lower than in climate classes As and Am and up to 5 dB lower than in climate class Af. This suggests that the dry reference might be estimated too low in cold climates where land cover is characterized by boreal forests. Since the wet reference can be considered the same for these classes, a lower dry reference leads to lower  $\tau_a$  values. Several processes could possibly explain the low estimates for the dry reference. In the TU Wien retrieval algorithm, the dry reference is estimated based on the lowest observed backscatter values per gridpoint. Since the dielectric constant of ice is significantly lower than that of water (Wang and Schmugge, 1980a), frozen soils are characterized by a lower backscatter, which can be similar to backscatter from dry soils (Hallikainen et al., 1984a). Hence, even if backscatter is obtained during frozen soil conditions, we assume these values are comparable to dry soil surface conditions. A possible explanation for lower dry reference values compared to more temperate climates, may be that in areas with an extended period of freezing, frozen conditions extend to the water content in vegetation (McDonald et al., 2002) and this leads to a decrease in backscatter. This decrease in backscatter due to the freezing of trees has been observed and modeled in other studies using L-Band SAR and C-Band SIR-C observations (Dobson et al., 1990; Ranson et al., 1995; Wang et al., 1993) over boreal forests. This hypothesis is supported by the extent of the low values for  $\tau_a$ , which only occur in boreal forests and taiga and not in less vegetated regions like the northern parts of the Siberian Plain. In cold climates many other natural processes can cause strong variations in backscatter, i.e. freeze-thaw cycles, snow cover and ponding water on frozen soils or snow. In springtime, when temperatures are above freezing point, surface water can form from snow melt and thawing of frozen soils. During this time backscatter values can decrease strongly, due to the presence of ponding water on the surface as shown in Bartsch et al. (2007). Dorigo et al. (2015) found artefacts in the soil moisture times series which lead to low correlations between *in situ* soil moisture and satellite soil moisture are found in northern latitudes. These artefacts are assumed to be caused by strong backscatter variations due to freeze-thaw cycles or specular reflection on ponding water which decreases the returned backscatter signal. Snow can also contribute to the backscatter signal, originating from three components, the top of the snow pack, volume scattering from within the snow pack, or the underlying soil. When the snow pack is dry, it is practically transparent and the backscatter signal is controlled by the underlying soil. But if the top of the snow pack is wet and smooth, backscatter originates from the top of the snow pack and can be as low as or even lower than from a dry soil. However, when calculating the dry reference outliers are removed and this subsequently masks backscatter values obtained during

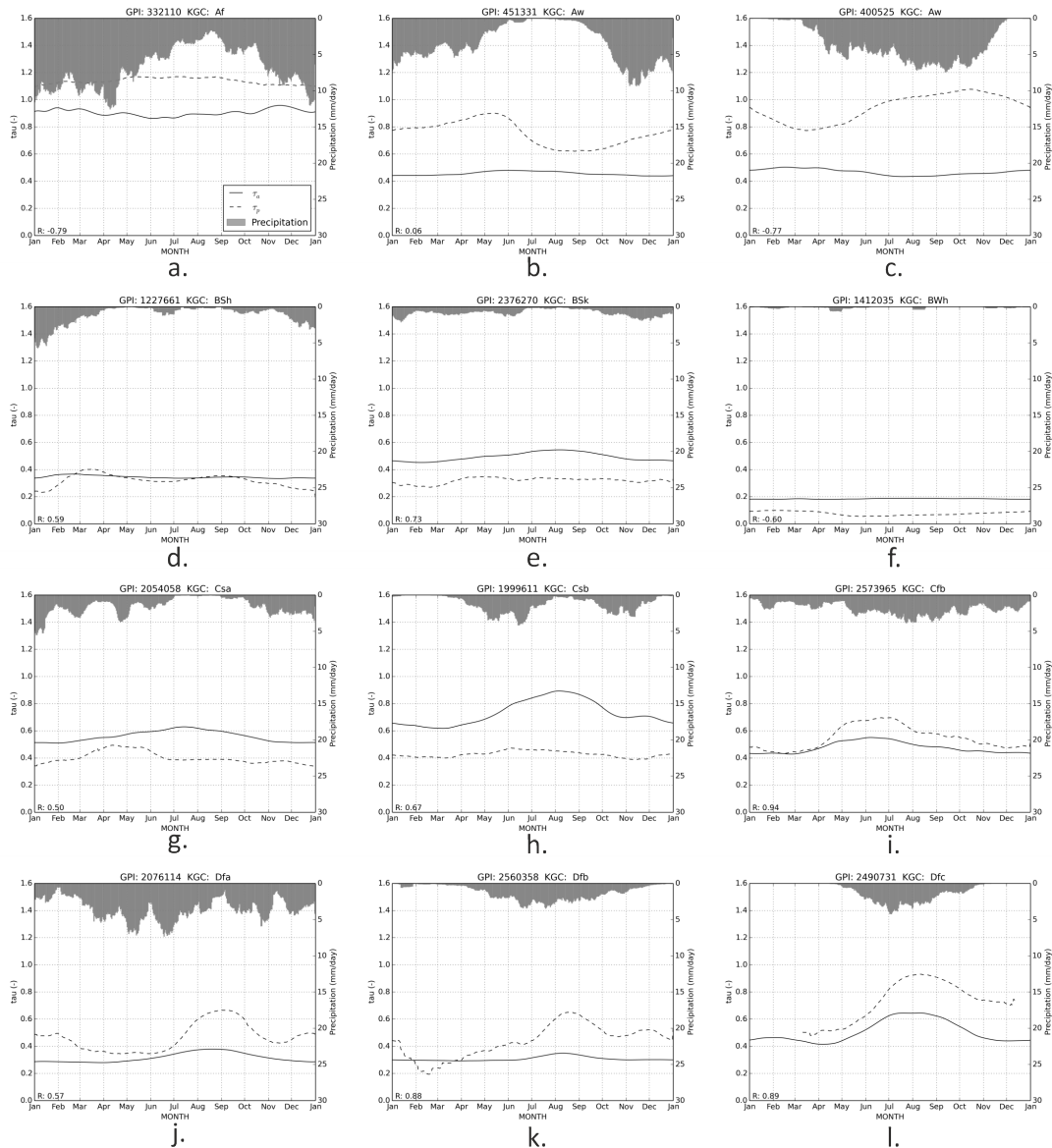


**Figure III.9:** Timeseries plots for  $\tau_a$  (solid line),  $\tau_p$  (dotted line) and GLDAS-Noah precipitation (grey bars) sorted after Koeppen Geiger climate classes; Tropical (a-c), Arid (row d-f), Temperate (g-i), Cold (j-l). Where the  $\tau_p$  shows a climatology based on data over the period 2007-2011. The locations of the plots can be found in Figure III.2. The numbers above the plots represent the gridpoints and the Koeppen Geiger climate classes and R gives the  $r_s$ .

freeze-thawing cycles, ponding water and wet snow cover. Naturally, the outlier removal is an automated procedure and can be subject to error. But since the dry reference is an average of many observations the contribution of these spurious values is assumed to be small.

The temporal behaviour of  $\tau_a$  and  $\tau_p$  is very similar to each other, although values for  $r_s$  are lower than for temperate climates. Especially, in Canada around the Hudson Bay, and the northern parts of Ural and Siberia negative  $r_s$  can occur. However, these areas are characterized by the presence of numerous lakes. As discussed before, the presence of open water and ponding water can cause artefacts in the retrieved  $\tau_a$  and  $\tau_p$ . The retrieval of both soil moisture and vegetation optical depth in northern latitudes is hindered by the presence of snow cover, freeze-thaw cycles and frozen soils and ponding water on the surface. Further research is planned to look at the estimation of the dry reference and the relation between the lowest backscatter values found for every gridpoints and the surface conditions at the time of observation.

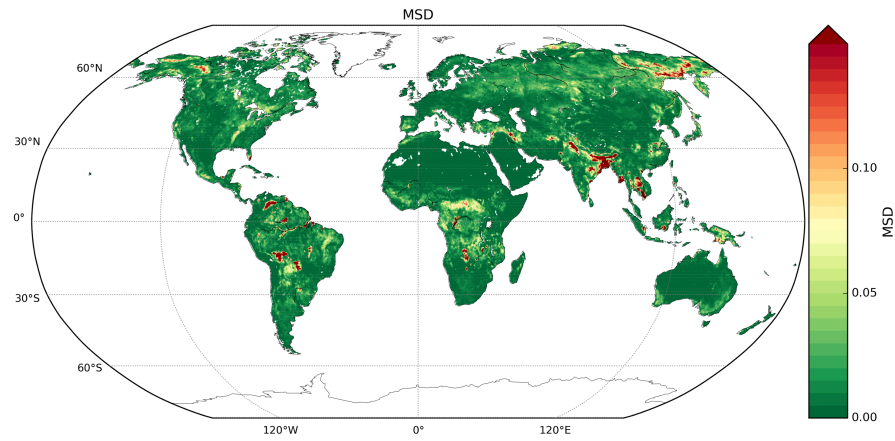


Figure III.10: Global Mean Square Error between  $\tau_a$  and  $\tau_p$ .

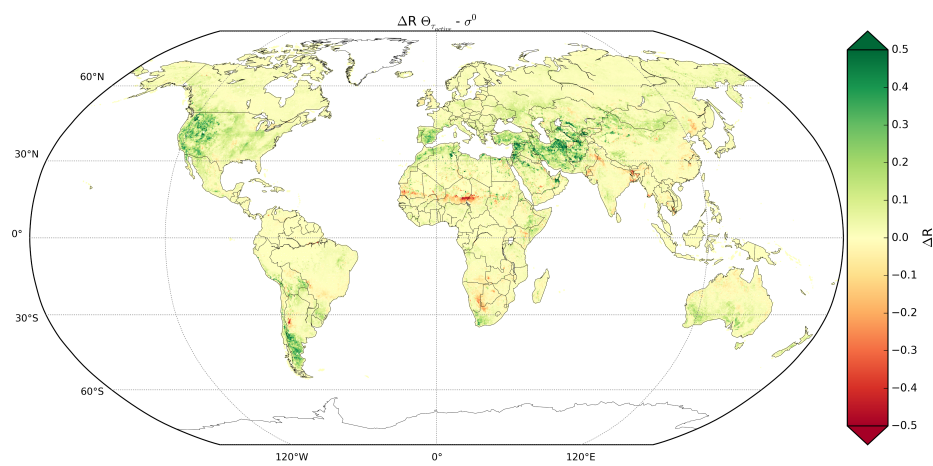
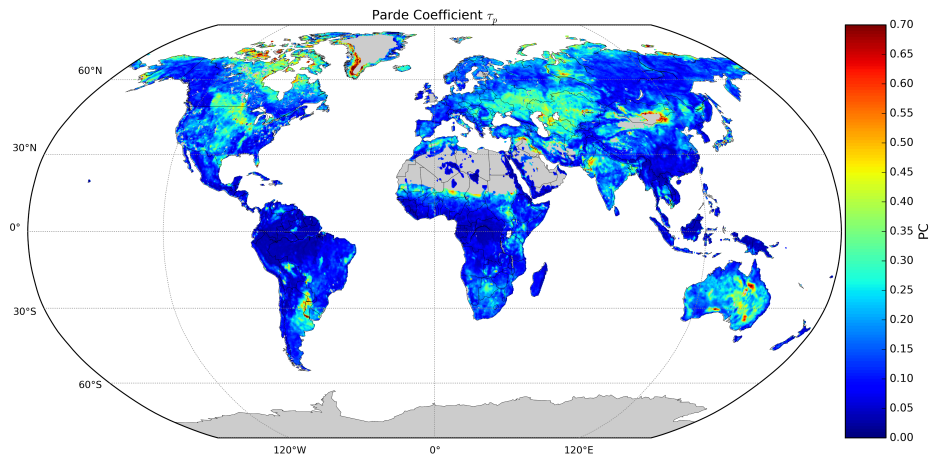
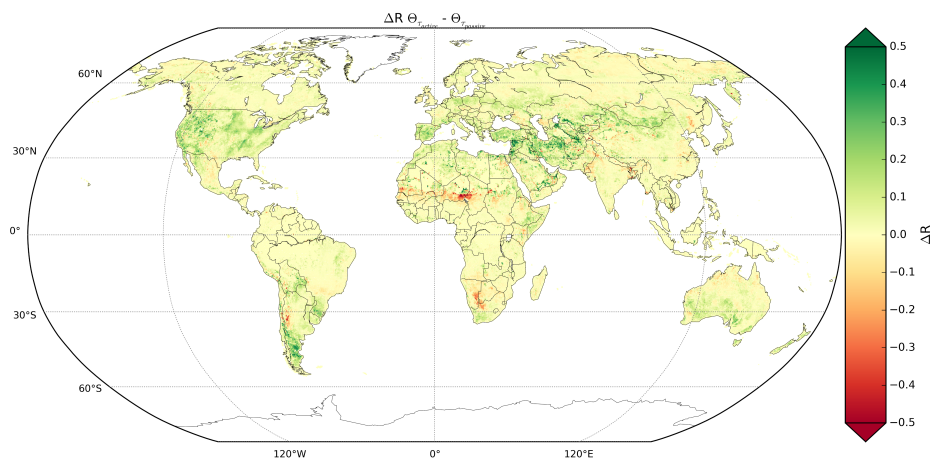


Figure III.11: The difference in  $r_s$  between  $\Theta_a$  and  $\Theta_{ERA}$  and  $\sigma^o(40)$  and  $\Theta_{ERA}$ , where positive values indicate areas where  $r_s$  between  $\Theta_a$  and  $\Theta_{ERA}$  is higher than between  $\sigma^o(40)$  and  $\Theta_{ERA}$ , i.e. areas with positive impact of the vegetation correction.



**Figure III.12:** The  $\Delta PC$  over the normalized monthly differences of  $\tau_p$ , where red areas represent high inter-annual variability.



**Figure III.13:** Difference in  $r_s$  between  $\Theta_a$  and  $\Theta_{ERA}$  and  $\Theta_{\tau_p}$  and  $\Theta_{ERA}$  where  $\tau_a$  is substituted by  $\tau_p$ . Negative values (in red) indicate areas where  $r_s$  between  $\Theta_{\tau_p}$  and  $\Theta_{ERA}$  is higher than between  $\Theta_a$  and  $\Theta_{ERA}$ .

### Wetlands

In wetlands and regularly or permanently flooded regions like irrigated areas and floodplains, i.e. the Ganges and Mekong floodplain, the Okavango Delta and rice fields in Malaysia  $\tau_a$  shows negative values for  $r_s$  with  $\tau_p$  (Fig. III.7) and very high values for MSE (Fig.III.10). Previous studies have emphasized that care should be taken with interpreting  $\tau_p$  observations in areas with large open water areas (Andela et al., 2013; Jones et al., 2011; Gouweleeuw et al., 2012). For active microwaves backscatter is controlled by the roughness of the water surface. Hence, the backscatter is a function of wind direction and impedes the retrieval of the  $\tau_a$ . Consequently, this can lead to low  $r_s$  values between both products.

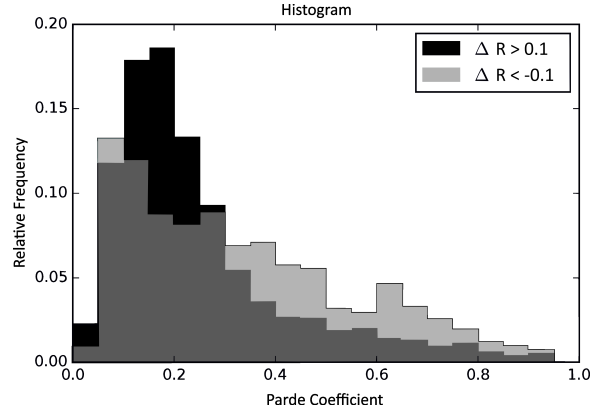


**Figure III.14:** The relative frequency of  $\Delta PC$  for points where when compared to ERA-Land  $\Theta_{\tau_p}$  outperforms  $\Theta_a$  ( $\Delta r_s < -0.1$ ) in pink-purple and where  $\Theta_a$  outperforms  $\Theta_{\tau_p}$  ( $\Delta r_s > 0.1$ ) in blue.

### 4.3 Effect of $\tau_a$ on soil moisture retrievals

Since  $\tau_a$  is a function of both  $\Delta\sigma^\circ$  and  $\Delta\sigma_s^\circ$ , the effect of  $\tau_a$  on soil moisture retrievals with regard to the absolute soil moisture values is not straightforward. However, since  $\Delta\sigma_s^\circ$  is assumed to be constant, apart for deserts, we can discuss the effects of  $\Delta\sigma^\circ$  and the estimation of  $\sigma_{dry}^\circ$  on the retrieved soil moisture. As already discussed in Section 4.2, in cold climates low values for the  $\sigma_{dry}^\circ$  are found most likely caused by surface conditions in winter and spring, i.e. snow cover, frozen soils, freeze-thaw cycles and ponding water on the surface. With the dry reference being this low, it introduces a positive bias in the soil moisture retrieval, which is suggested by the relatively high soil moisture values found in boreal forests compared to soil moisture products from other satellites, e.g. SMOS and AMSR-E (Al-Yaari et al., 2014). Al-Yaari et al. (2014) have attributed the high soil moisture values to the high porosity values that were used to calculate absolute soil moisture. However, considering the low values for  $\tau_a$  another likely explanation is the low dry reference which is obtained during frozen conditions.

The TU Wien products before and after the application of the current vegetation correction, i.e. the TU Wien normalized backscatter ( $\sigma^\circ(40)$ ) and TU Wien soil moisture ( $\Theta_a$ ) respectively, were compared to modeled surface soil moisture from ERA-Land ( $\Theta_{ERA}$ ) (Fig. III.11). Green colors represent regions where the vegetation correction improves  $r_s$  with ERA-Land, while red colors indicate areas where  $r_s$  between  $\Theta_a$  and  $\Theta_{ERA}$  is decreased as a result of the vegetation correction. The results demonstrate the positive impact of the existing vegetation correction over semi-arid, temperate and cold climates, reinforcing the previously observed high values of  $r_s$  between  $\tau_p$  and  $\tau_a$ . Especially, the positive impact on soil moisture retrievals in deserts and drylands is interesting since the temporal  $r_s$  between  $\tau_a$  and the  $\tau_p$  is negative in these areas. This suggests that either the existing vegetation correction does not correct for vegetation, but corrects for dynamic land surface properties other than vegetation or that  $\tau_p$  does not describe vegetation correctly.

$r_s$  between  $\Theta_a$  and ERA-Land soil moisture can decrease by as much as 0.4 in the northern Sahel, the southern regions in Africa and the Ganges and Mekong floodplains and deltas compared to  $r_s$  between  $\sigma^\circ(40)$  and ERA-Land soil moisture. We suggest that this is due to the fact that these regions are characterized by strong inter-annual variations in vegetation, while the correction method applies the same correction every year. Fig. III.12 shows inter-annual variability in the  $\tau_p$  for the period 2007-2011 based on the range between the minimum and maximum Parde Coefficient  $\Delta PC$  (Viglione et al., 2013).  $\Delta PC$  is calculated as the difference between the minimum and maximum monthly mean  $\tau_p$  values normalized per year:

$$\Delta PC = \frac{1}{m} \sum_{m=1}^{12} \frac{\max(\tau_{p(m,a)}) - \min(\tau_{p(m,a)})}{\tau_{p(a)}} \quad (\text{III.17})$$

, where subscript  $m$  represents months and  $a$  represents years. Areas with a high coefficient are areas where the behaviour of the  $\tau_p$  differs significantly from year to year. Regions of strong inter-annual variability in  $\tau_p$  can be found in Australia, the Sahel, southern Africa and Texas. These regions correspond with regions where the  $\Theta_a$  shows less correspondence to  $\Theta_{ERA}$  than the  $\sigma^\circ(40)$ . In these regions inter-annual variability is not only found in the mean or maximum of the vegetation, but also in the timing, e.g. where vegetation growth is strongly dependent on sporadic rainfall events and hence the timing of maximum vegetation cover is highly variable.

Figure III.13 shows the results of the inter-annual variability test, with the difference in  $r_s$  between modeled soil moisture,  $\Theta_{ERA}$ , and the soil moisture product using the  $\tau_a$  as a correction,  $\Theta_a$ , and the soil moisture product using  $\tau_p$  as a correction  $\Theta_{\tau_p}$ . Fig. III.13 is very similar to Fig. III.11 but in more temperate and continental climates, like in Europe and North-America, the use of  $\tau_p$  deteriorates the soil moisture retrieval with lowering  $r_s$  with as much as 0.5. Areas like the Sahel, which are characterized by high inter-annual variability in vegetation dynamics show significantly higher  $r_s$  values when using  $\Theta_{\tau_p}$ . Fig. III.14 shows the histograms of relative frequency of  $\Delta PC$  for points where  $\Theta_{\tau_p}$  outperforms  $\Theta_a$  when correlated to  $\Theta_{ERA}$  ( $\Delta r_s < -0.1$ ) and when  $\Theta_a$  correlates better to  $\Theta_{ERA}$  ( $\Delta r_s > 0.1$ ). The histogram shows that points where  $\Theta_{\tau_p}$  outperforms  $\Theta_a$  correspond to areas with a high  $\Delta PC$ , i.e. to areas with a high inter-annual variability. In addition, a Mann-Whitney test was performed which confirmed a significant difference between  $\Delta PC$  of areas where  $\Theta_{\tau_p}$  performed better, characterized by a higher  $\Delta PC$ , and areas where  $\Theta_a$  performed better, characterized by a low  $\Delta PC$ . It appears that in areas with no significant inter-annual variability in vegetation dynamics the seasonally fixed vegetation correction shows similar results or even outperforms the  $\Theta_{\tau_p}$ . For these regions the characterization of vegetation and roughness is better by the existing vegetation correction than by the  $\tau_p$ .

## 5 Conclusions

This study analysed the vegetation correction method of the TU Wien soil moisture retrieval algorithm for active microwave observations and its impact on the final soil moisture product. To verify spatio-temporal characteristics of the vegetation characterization with respect to a vegetation product from passive microwave observations we first converted it into vegetation optical depth using a water-cloud model. On average, mean values of the newly derived  $\tau_a$  are 0.15 lower than mean values from  $\tau_p$  retrieved using LPRM from passive microwave observations. This can be attributed to the underestimation of  $\Delta\sigma_s^\circ$ . Over boreal forests,  $\tau_a$  is even lower, which can potentially be explained by the estimation of the dry reference over cold climates. Apart from the low values in boreal forests,  $\tau_a$  shows very similar spatial patterns as  $\tau_p$  and the retrieval of  $\tau_a$  is not hampered by the assumption that  $\Delta\sigma_s^\circ$  does not vary spatially. High temporal correlation coefficients are found between  $\tau_a$  and  $\tau_p$  in temperate and continental climates, apart from areas with open water. Especially in semi-arid, temperate and cold climates  $\tau_a$  shows potential to monitor vegetation. In arid regions and in areas with dry hot summers low or even negative correlations with the  $\tau_p$  were observed. These are likely due to volume scattering effects or apparent soil roughness changes in dry soils. However, in these areas the effect of vegetation on the soil moisture retrieval is minimal and the vegetation correction does not negatively impact the quality of the soil moisture product itself.

In areas where there is high inter-annual variability in vegetation dynamics the soil moisture product is negatively affected by the fixed year-to-year vegetation correction, even though the  $\tau_a$  itself is highly correlated to  $\tau_p$ . Substituting the existing correction for a dynamic correction based on the  $\tau_p$  demonstrates that the soil moisture product is improved with respect to soil moisture from ERA-Land in areas with high inter-annual variability in vegetation dynamics. Consequently, the importance of a dynamic, from year to year varying vegetation correction in soil moisture retrievals is confirmed with this study. This is especially valuable information for the algorithm development of new soil moisture missions like SMAP and Sentinel-1 and the improvement of

the TU Wien soil moisture retrieval itself. With regard to the latter, research is ongoing to develop a dynamic vegetation correction from ASCAT active microwave observations in order to provide a more robust and accurate soil moisture product. Based on the results of this study, it is expected that the new dynamic correction will improve the soil moisture retrieval especially in drylands and deserts and regions with high inter-annual variability in vegetation.

## Acknowledgements

This study was performed in the framework of the Doctoral Programme on Water Resource Systems (DK-Plus W1219-N22) of the Austrian Science Funds FWF and ESA's Climate Change Initiative for Soil Moisture (contract 4000104814/11/I-NB). We thank Emanuel Dutra and Clement Albergel from ECMWF and Matthias Langer from ZAMG for providing ERA-Land soil moisture data, NASA for providing GLDAS-NOAH precipitation data and University of Veterinary Medicine Vienna, Austria for providing Koeppen Geiger climate maps. Furthermore, we thank N. Andela and J.L. Salinas for their valuable input on inter-annual vegetation dynamics, wildfires and perturbation models and the reviewers for their comments and valuable feedback.

# Chapter IV

## Inter-comparison of Vegetation Variables Derived from Microwave Instruments.

Mariette Vreugdenhil, Sebastian Hahn, Christoph Reimer, Thomas Melzer,  
Wouter Dorigo, Raphael Quast, Richard de Jeu, Robin van der Schalie,  
Felix Greifeneder, Emanuele Santi, Claudia Notarnicola, Simonetta Paloscia  
and Wolfgang Wagner

This chapter is based on a paper which will be submitted.

*The layout has been revised.*

## Abstract

*This paper describes a comparison between novel vegetation products retrieved from two scatterometers and vegetation datasets from a passive microwave radiometer and visible and near-infrared data. The products were compared in terms of spatial and temporal characteristics and phenological parameters derived from them. We found that a ratio of cross- and co-polarized data from Aquarius scatterometer observations (CR) and vegetation optical depth retrieved from Advanced Scatterometer observations ( $\tau_a$ ) are able to follow vegetation dynamics as found in Leaf Area Index (LAI) and vegetation optical depth from the Advanced Microwave Scanning Radiometer 2 ( $\tau_p$ ), with correlation coefficients of 0.58 and 0.19 between LAI and  $\tau_a$  and CR, respectively. Highest correlations with LAI are found over croplands and grasslands ( $\tau_a$ : 0.74 and 0.72,  $\tau_p$ : 0.79 and 0.62). Products from scatterometers show negative correlations with  $\tau_p$  and LAI over Deciduous Broadleaf Forests, where leaf fall might contribute to unexpected backscatter behaviour. This exposes a different response of active and passive microwave observations to changes in vegetation. The observed time lag between LAI and the microwave indices is suggested to be related to the different penetration depth of LAI and  $\tau$ . This study demonstrates the complementary nature of vegetation products from scatterometers to existing vegetation products, and especially the added value of cross-polarized data for vegetation parameterization in soil moisture retrieval algorithms where data is not available under different incidence angles.*

## 1 Introduction

In recent years our understanding of the hydrological-, energy- and carbon cycles has increased by the availability of long-term global data sets of land surface parameters, e.g. soil moisture and vegetation optical depth. Microwave observations from satellites provide data on a global scale and on near-daily basis, enabling the retrieval of near-daily soil moisture and vegetation datasets. Microwave remote sensing monitoring of vegetation has the advantage that it is not hindered by cloud cover, smoke, aerosol contamination and low solar illumination, unlike visible near infra-red (VNIR) remote sensing. Due to its sensitivity to water, microwave observations are assumed to be sensitive to land surface parameters including: soil moisture and vegetation water content. Their sensitivity to water in both soil and vegetation makes the retrieval of a single parameter from microwave observations ambiguous, since similar backscatter values and brightness temperatures can be found for different combinations of soil and vegetation water content and characteristics.

Recently, [Vreugdenhil et al. \(2016a\)](#) retrieved vegetation optical depth from Advanced Scatterometer (ASCAT) backscatter observations ( $\tau_a$ ) using model parameters estimated within the TU Wien change detection algorithm and a simple water-cloud model. The  $\tau_a$  showed similar spatial patterns to vegetation optical depth from Advanced Microwave Scanning Radiometer - Earth (AMSR-E) ( $\tau_p$ ), although comparatively low values were observed in boreal forests. Positive correlation coefficients indicated that temporal behaviour of the two products is similar over temperate and cold climates, but distinct negative correlations were found in deserts and drylands. [McColl et al. \(2014\)](#) used Aquarius cross and co-polarized backscatter observations (HV, HH and VV) at L-band to calculate the so-called Radar Vegetation Index (RVI). Results showed that RVI distinguishes well between vegetation densities, with low values in sparsely vegetated areas and high values in tropical forests. The RVI showed a distinct seasonal cycle, which corresponded to modeled precipitation. On the field scale, the RVI showed a high linear correlation to *in situ* measured NDVI, LAI and vegetation water content over cropfields ([Kim et al., 2012a](#)). [Paloscia et al. \(2013\)](#) found that the ratio (CR) between cross- and co-polarized backscatter (VH/VV and HH/HV) from field observations from SIR-C, X-SAR and ASAR over different sites, exhibits a good sensitivity to vegetation cover (slope = -4.69), expressed as NDVI, whereas the sensitivity to soil moisture is negligible (slope = -0.03). This result was confirmed by model simulations, where the regressions between simulated and observed CR and NDVI were compared and found to be

**Table IV.1:** Overview of the characteristics of all datasets used in the study.

Product	Platform, Sensor	Frequency	Spatial Res.	Spatial Sampling	Temp. Res.	Temp. coverage
CR	SAC-D, Aquarius	L-band	84 x 120 km		7 days	2011/06 - 2015/06
$\tau_a$	Metop-A, ASCAT	C-band	25 x 25 km	12.5 km	2 days	2007/05 -
$\tau_p$	GCOM-1, AMSR2	C-band	35 x 62 km	0.25°	2 days	2012/05 -
LAI	SPOT, VGT	Blue, Red, near+middle IR	1165 x 1165 m	1/112°	10 days	2002/05 -

very close to each other (Paloscia et al., 2013).

The first long-term  $\tau_p$  product from AMSR-E passive microwave observations using the VUANASA Land Parameter Retrieval Model (LPRM) was derived by Liu et al. (2011). Several studies have validated  $\tau_p$  by comparing it with the Normalized Difference Vegetation Index (NDVI) and looking into long-term trends (Andela et al., 2013; Liu et al., 2011). Higher agreement between microwave vegetation indices and NDVI was found in Santi et al. (2012) where the vegetation biomass was estimated by using the X-band (10 GHz) channel, which is more sensitive to surface vegetation features than C-band. When comparing vegetation parameters derived from microwave observations to NDVI a lag between the two is often found (Wagner et al., 1999a; Jones et al., 2012; Andela et al., 2013; Guan et al., 2014; Tian et al., 2016). In contrast to NDVI, derived from VNIR observations, microwave observations are not sensitive to the chlorophyll content of the vegetation but more sensitive to the total amount of vegetation water. Hence,  $\tau$  is also related to the above ground biomass, since a large fraction of biomass is water. Jones et al. (2012) demonstrated that the Start Of Season (SOS) derived from  $\tau_p$  preceded NDVI with 4-7 weeks in cold, temperature limited regions and followed NDVI in warmer, water limited regions. Tian et al. (2016) found that over drylands in the West African Sahel, there is a shift in the peak between  $\tau_p$  and NDVI, which increases with increasing woody cover. This was also observed by Guan et al. (2014) over African savannah and woodlands. All three studies (Jones et al., 2012; Guan et al., 2014; Tian et al., 2016) contribute the shift in SOS and peak to the fact that NDVI is more sensitive to canopy photosynthetic activity, which responds quickly to rainfall.  $\tau_p$  responds slower since vegetation total water content reaches its peak later in the season. Other studies also suggested that a peak in total amount of vegetation water does not necessarily coincide with a peak in the greenness of the vegetation (Liu et al., 2011; Wagner et al., 1999a; Andela et al., 2013; Doubkova et al., 2009). These studies demonstrate the complementary nature of VNIR and microwave products, where  $\tau$  is more sensitive to the total vegetation water content and thus also the woody component of the vegetation.

The above described studies give an insight in the similarities and differences between the different vegetation data sets, but a detailed inter-comparison between active microwave products and VNIR and passive microwave products is still missing. This study presents a comprehensive inter-comparison of four different vegetation products and indices from different sources and algorithms; Cross-Ratio (CR) from Aquarius (L-band),  $\tau_a$  from ASCAT (C-band),  $\tau_p$  from AMSR2 (C-band) and Leaf Area Index from SPOT-VEGETATION (VNIR). The primary objectives of this study are to: 1) compare  $\tau_a$  and CR to existing products from passive microwave observations and VNIR observations,  $\tau_p$  and Leaf Area Index respectively, 2) identify differences between products from active and passive microwave observations, 3) quantify differences in timing of phenological parameters, i.e. SOS and Peak Of Season (POS). The results are discussed in three sections: spatial, temporal and phenology comparison.

## 2 Data and Methods

### 2.1 Aquarius - Cross Ratio (CR)

Aquarius is a NASA multi-polarimetric scatterometer on board of SAC-D which provided global L-band observations from June 2011 until its mission-ending failure in June 2015. The scatterometer is arranged in a pushbroom configuration with three beams, oriented at the respective incidence angles of  $28.7^\circ$  (inner beam),  $37.8^\circ$  (mid beam), and  $45.6^\circ$  (outer beam). Aquarius is in a sun-synchronous orbit, passing the equator twice a day (6 a.m. and 6 p.m. local time) and has a repeat time of seven days. Aquarius' footprint is elliptical with dimensions of  $7 \times 94$ ,  $84 \times 120$ , and  $96 \times 156$  km, respectively (Vine et al., 2007) (Table IV.1). For this study only mid beam data is used since this incidence angle is closest to the reference incidence angle of the TU-Wien soil moisture retrieval algorithm of  $40^\circ$ . Aquarius Level 2 version 4.0 data is used and resampled to the closest latitude and longitude on a  $1^\circ$  grid. Operating at L-band, Aquarius data is heavily affected by Radio Frequency Interference (RFI). Especially over the northern hemisphere a large part of the data is unreliable due to RFI. Therefore, we masked data for severe RFI.

Co-polarized backscatter is sensitive to both vegetation and soil moisture, and the VV backscatter signal was found to follow precipitation. Cross-polarized backscatter is found to be more sensitive to vegetation (McNairn and Brisco, 2004; Toan et al., 1992b) and increases stronger than VV-backscatter with vegetation growth. A commonly used index using HV cross- and VV and HH co-polarized backscatter observations is the Radar Vegetation Index (McColl et al., 2014; Piles et al., 2015). However, HV polarized data is not always available. At the moment, the primary mode for Sentinel-1 over land is the Interferometric Wide Swath mode with VV and VH polarization. HV polarized data in extra wide swath mode is at the moment only available over northern regions. And the follow up mission of the Metop ASCAT series, the Metop-SG SCA mission, is planned to provide VH and VV polarized backscatter observations. Hence we choose to use a ratio which can be calculated from Sentinel-1 observations and Metop-SG SCA observations when they become available. Since Paloscia et al. (2013) found a relation between NDVI and the cross-ratio between VV and VH polarized data (CR), this ratio is used in this study to compare it to other vegetation products. The ratio is calculated by converting the Aquarius VV and VH time series to the linear domain and is described as:

$$CR = \sigma_{VH}^{\circ} / \sigma_{VV}^{\circ} \quad (IV.1)$$

### 2.2 ASCAT - vegetation optical depth ( $\tau_a$ )

The Advanced Scatterometer (ASCAT) on-board of Metop-A provides VV-polarized backscatter observations in C-band on a global scale every two days since 2007. It has a spatial resolution of 25 - 34 km, and is sampled to a 12.5 km grid in swath orbit geometry (Table IV.1). Backscatter is observed under different incidence angles ( $\theta$ ), ranging from  $20^\circ$  to  $60^\circ$ .

$\tau_a$  is computed from ASCAT model parameters derived from the TU Wien backscatter model used for operational soil moisture retrieval (Wagner et al., 1999b; Naeimi et al., 2009). The first step in the TU Wien retrieval algorithm is the normalization of backscatter observations to a reference incidence angle  $\theta_r = 40^\circ$  using a second-order Taylor expansion function. The first and second order coefficients of the expansion function are the slope and curvature parameters of the backscatter-incidence angle relationship ( $\sigma_r'$  and  $\sigma_r''$ ). The estimation of  $\sigma_r'$  and  $\sigma_r''$  is done using the so called local slopes. ASCAT measures backscatter under two distinct incidence angles at the same time. The difference in  $\theta$  varies between  $9^\circ$  for the near range and  $10^\circ$  in the far range and a local slope can be obtained between the two incidence angles. These local slopes are only valid for

a small range of incidence angles, and are therefore assigned to a local incidence angle which is defined as the center point between the two distinct incidence angles.  $\sigma'_r$  and  $\sigma''_r$  are calculated as a straight line fitted to these so-called local slopes. To ensure precision of the estimates, account for noise and make sure that the whole range of  $\theta$  is covered, the fit is computed by aggregating the local slopes for every day of year, covering the entire observation period of ASCAT from 2007 to 2015. In addition,  $\sigma'_r$  and  $\sigma''_r$  are calculated averaging over a time window of two to twelve weeks centred at the specific day of year. The length of the time window is determined by using a Monte Carlo simulation which contaminates the original time series with Gaussian noise and randomly assigns a window length. Because of computational limitation, this is only done for the 15th day of each month and a cubic spline interpolation is applied to achieve a seasonality of  $\sigma'_r$  and  $\sigma''_r$  for 366 days.

$\sigma'_r$  and  $\sigma''_r$  are also used to account for vegetation effects on the backscatter. It is assumed that backscatter strongly depends on  $\theta$  and that  $\sigma'_r$  and  $\sigma''_r$  of the  $\sigma^\circ - \theta$  relationship are heavily affected by changes in vegetation, but not by changes in soil moisture: Vegetation dynamics change  $\sigma'_r$  whereas soil moisture variations affect the backscatter signal over the complete incidence angle range, thereby leaving  $\sigma''_r$  unaltered. This assumption is one of the key characteristics of the TU Wien change detection algorithm and is also the basis of the  $\tau_a$  retrieval. With this behaviour, cross-over angles exist, where the effect of vegetation is cancelled out. [Wagner et al. \(1999a\)](#) found these cross-over angles to lie at  $25^\circ$  for dry soils and  $40^\circ$  for wet soils. Soil moisture is calculated by scaling backscatter between the historically driest and wettest conditions, the lowest and highest observed backscatter, respectively. Within the TU Wien retrieval algorithm the so-called dry reference ( $\sigma^\circ_{dry}$ ) is calculated at the dry cross-over angle to account for vegetation effects. At  $\theta = 25^\circ$ , the lowest observed backscatter is taken, which represents the historically driest conditions. Here backscatter is filtered for outliers, but frozen conditions are not masked. Within the algorithm it is assumed that frozen soils have a similar dielectric constant and backscatter signal as dry soils ([Wang and Schmugge, 1980b](#); [Hallikainen et al., 1984b](#)). Using the  $\sigma'_r$  and  $\sigma''_r$  this lowest backscatter value at  $\theta = 25^\circ$  is then converted back to  $\theta_r$  at  $40^\circ$  using the second-order Taylor expansion function. Consequently, temporal variability in the dry reference is controlled by  $\sigma'_r$  and  $\sigma''_r$  and it intrinsically accounts for vegetation dynamics. As discussed in the previous paragraph,  $\sigma'_r$  and  $\sigma''_r$  are only available as a seasonality, i.e. 366 values, and are smoothed with a time window of two to twelve weeks and a cubic spline interpolation. Hence  $\sigma^\circ_{dry}$  is only available as a seasonality. The historically wettest conditions are represented in the wet reference ( $\sigma^\circ_{wet}$ ), which are the highest backscatter values at a  $\theta_r$  of  $40^\circ$ . Since the wet reference does not need to be converted to a different  $\theta$  it does not vary over time.

The dry reference contains information on vegetation dynamics, and [Vreugdenhil et al. \(2016a\)](#) use the dry reference and a water-cloud model ([Attema and Ulaby, 1978](#)) to retrieve vegetation optical depth as:

$$\tau_a(DoY) = \frac{\cos \theta}{2} \ln \frac{\Delta \sigma^\circ_s}{\Delta \sigma^\circ(DoY)} \quad (IV.2)$$

where  $\Delta \sigma^\circ$ , in  $m^2 m^{-2}$ , is the difference between  $\sigma^\circ_{dry}$  and  $\sigma^\circ_{wet}$ , and  $\Delta \sigma^\circ_s$ , also in the linear domain, represents the maximum range in backscatter values over bare soils related to a change in soil moisture only and is assumed to be constant through time. A more detailed description of the soil moisture retrieval algorithm and optical depth retrieval can be found in [Hahn et al. \(2016\)](#) and Chapter III.

### 2.3 AMSR2 - vegetation optical depth ( $\tau_p$ )

The Advanced Microwave Scanning Radiometer 2, AMSR2, on-board the Global Change Observation Mission-1st Water satellite provides brightness temperatures at C-band on a global scale every two days since May 2012 at a spatial resolution of  $35 \times 62$  km (Table IV.1). The Land Parameter Retrieval Model (LPRM) developed by VUA-NASA uses a forward radiative transfer model

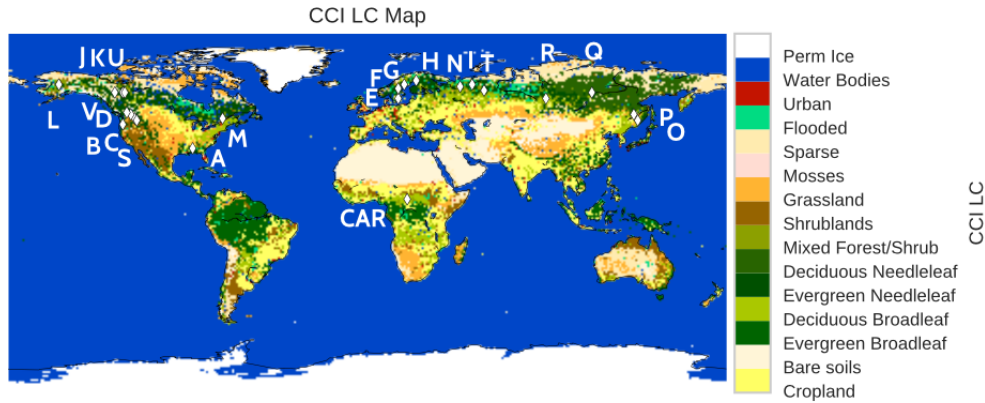


**Figure IV.1:** CCI Land Cover map resampled to  $1^\circ$ . Locations of gridpoint used in Fig. IV.3 and in Fig. IV.6 are indicated with white diamonds.

to derive soil moisture and vegetation optical depth ( $\tau_p$ ) simultaneously from C-band and X-band observations (Owe et al., 2008). Land surface temperature is derived separately from AMSR2's Ka-band (Holmes et al., 2009). Only night-time observations are used to calculate soil moisture and  $\tau_p$ . AMSR2 is sensitive to RFI and in this study data is masked according to Nijs et al. (2015).  $\tau_p$  is available on a  $0.25^\circ$  grid. In this study we use only  $\tau_p$  values retrieved from C-band observations.

## 2.4 SPOT-VEGETATION - Leaf Area Index (LAI)

Leaf Area Index is defined as half the developed area of photosynthetically active elements of the vegetation per unit horizontal ground area. In this study the GEOV1 LAI dataset from VITO is used, derived from observations from the VEGETATION sensor on-board SPOT (Baret et al., 2013) (SPOT-VGT). Several studies have validated GEOV1 products based on SPOT-VGT data and showed that a good temporal consistency exists with MODIS derived products (Raymaekers et al., 2014) and ground-measured LAI (Yang et al., 2015). In addition, Camacho et al. (2013) found that GEOV1 products outperform the quality of reference products (MODIS c5, CYCLOPES v3.1, GLOBCARBON v2 LAI and JRC SeaWiFS FAPAR). The GEOV1 algorithm consists of a neural network providing estimates of LAI for each used sensor. This approach is chosen to use existing knowledge and validation results and to easily merge data from different sensors into one long-term dataset. As a first step a training dataset is generated using CYCLOPES v3.1 and MODIS C5 LAI products. The neural network is calibrated on this training dataset and then applied to Top Of Canopy reflectance from SPOT-VGT in red, near-infrared and shortwave infrared. In this way, top of canopy reflectance values from the used sensors are paired with the 'best estimates' of LAI from MODIS C5 and CYCLOPES v3.1, providing a fused and scaled LAI dataset. Both MODIS and CYCLOPES are based on a radiative transfer model inversion. The resulting LAI dataset is a 10-day composite with a spatial resolution of  $1/112^\circ$ . LAI data for the period 2013 - 2014 was downloaded from the the Geoland2 web portal (accessed March 18, 2016) (Table IV.1). For this research LAI observations are masked for invalid observations based on the provided quality flags. Observations which are suspect, or which fall out of the valid range for LAI are masked. In addition the land/sea mask, snow flag and aerosol contamination flags are applied and observations are masked.

## 2.5 Additional Datasets

### ERA-Interim

In order to mask data for frozen soils and snow cover modeled data from the European Centre for Medium Range Weather Forecasts (ECMWF) (Dee et al., 2011; Balsamo et al., 2013) is used. ERA-Interim data are available on a reduced Gaussian grid, with a spatial resolution of  $0.7^\circ$  at the equator and increases with latitude. In this study soil temperature and snow depth from ERA-Land is used for masking. Soil temperature of the first soil layer (0 - 7 cm) and snow depth was extracted for the period 2013 - 2014. Data is available every 6-hrs and daily means are calculated by averaging all observations within one day. In addition, air temperature at 2 m height from ERA-Interim is used for additional analysis in subsection 3.1.

### Global Precipitation Climatology Centre

To show the relation between seasonality of vegetation and precipitation we used monthly precipitation data. Precipitation data is available from the GPCP Version 7 Full Data Product until 2013 (Schneider et al., 2013). Data is based on quality-controlled station data and is available on a  $1^\circ$  spatial resolution. We calculated seasonality of monthly precipitation over the years 2007-2013. The precipitation data was only used to show the seasonality and is not used in any calculations. Even though this does not coincide with the period for which the vegetation products are available, we assume the seasonality of precipitation over this period can provide general insight on when precipitation occurs.

### CCI Land Cover

The Climate Change Initiative Land Cover map has been developed as part of the European Space Agency Global Monitoring of Essential Climate Variables project. For this study the CCI Land Cover map for the period 2008 - 2012 is used, based on MERIS and SPOT-VGT data. The Land Cover map is available on a 300 m spatial resolution and is resampled to a  $1^\circ$  resolution by taking the median value for each  $1^\circ$  gridpoint (Fig. IV.1).

## 2.6 Data preparation

In order to enable a fair comparison between the different data sets a number of processing steps have been applied. A detailed overview of the data characteristics is given in Table IV.1.

The four datasets used are all spatially sampled at different grids, i.e.  $1/112^\circ$  for SPOT-VGT, 12.5 km for ASCAT,  $0.25^\circ$  for AMSR2 and  $1^\circ$  for Aquarius. All datasets are resampled to the coarsest resolution, a  $1.0^\circ$  grid, by taking the median value for all values within a  $1.0^\circ$ . The coarsest resolution is chosen as the reference grid to prevent spatial representativeness errors by resampling a coarse resolution product to a finer resolution. Since LAI data is not available over deserts, metrics are not calculated over these areas.

Frozen soil or snow cover affect the reliability of Aquarius, AMSR2, ASCAT and SPOT-VGT observations. Although SPOT-VGT provides a snow quality flag, we have applied an additional masking to make sure that all products are masked in the same way. For the masking we use ERA-Interim model estimates of snow depth and soil temperature for the first soil layer from 0 - 7 cm. Two steps of masking have been applied: 1. to the time series for  $\tau_p$ , CR and LAI, 2. to the seasonalities for  $\tau_a$ ,  $\tau_p$ , CR and LAI. The time series of  $\tau_p$ , CR and LAI are individually masked for days when snow depth exceeds 0.05 m water equivalent or when soil temperature is below  $2^\circ\text{C}$ . Since  $\tau_a$  is only available as a seasonality we could not apply a masking on the time series.

Hence, we calculate the seasonality of snow cover and soil temperature and additionally mask the seasonality of all four datasets for snow depth ( $>0.05$  m water equivalent) and frozen soils ( $<2^{\circ}\text{C}$ ). Days with no snow cover or soil temperatures above  $2^{\circ}\text{C}$ , which fall within a prolonged period with snow cover and temperatures below  $2^{\circ}\text{C}$  are also masked.

To enable a fair comparison between the four different vegetation products the seasonalities of the datasets are temporally matched. Because of the different temporal coverage of all satellites only two complete years are available, 2013 and 2014 respectively. Data from these two years are used for further analysis. Since only the seasonality is available from  $\tau_a$ , i.e. 366 values, the seasonality has been calculated for all the other datasets. LAI is only available every 10 days and this is chosen as the reference temporal resolution. Since LAI is a composite of 10 days, we calculate a 10 day moving average for  $\tau_a$ ,  $\tau_p$  and CR. The 10 day moving average of the three products is matched to LAI. These datasets are then used to calculate the spatial and temporal comparison metrics. The temporal matching leads to a limited amount of observations mainly in northern regions where datasets are masked for frozen soils and snow conditions. All gridpoints where less than 15 observations, i.e. covering less than half a year, are available are discarded from further analysis.

For calculating phenological metrics additional processing steps have been taken. Because a smoothing window is applied to calculate  $\sigma_r'$  and  $\sigma_r''$  within the TU Wien algorithm, seasonalities of  $\tau_p$ , LAI and CR are smoothed using a Savitzky-Golay filter. The Savitzky-Golay filter smooths data based on a least square regression of subsets of adjacent datapoints. For all three datasets a window length of 45 days is taken to smooth the data and a coefficient of 2. To apply the Savitzky-Golay filter data was linearly interpolated with a 21 day maximum interpolation period. This was done to ensure that prolonged periods with missing data, i.e. in winter, are not crudely interpolated.

## 2.7 Comparison Metrics

Comparisons were done both spatially and temporally. Spatial patterns in the different products are related to the CCI Land Cover product. Temporal behaviour is evaluated by looking at the correlation between different products. The products are not necessarily linearly related to each other. Because of this we chose to use Spearman Rank Correlation ( $r_s$ ), which does not make any assumptions on the relationship between two variables.  $r_s$  is calculated for every  $1^{\circ}$  gridpoint. Two phenological parameters are retrieved from all datasets, the timing of Start Of Season (SOS) and Peak of Season (POS). POS is found by taking the maximum value found in the data, and SOS is estimated using a threshold-method used by [White et al. \(1997\)](#) for NDVI. To compute the phenology metrics the seasonality of the respective product is scaled between its minimum and maximum and a threshold of 0.5 is chosen; here the respective product has attained 50% of its total regardless of land cover. To correct for outliers, SOS is only given if it falls within four months before POS. Since SOS calculation is very sensitive to gaps in winter due to frozen soils and snow cover, we only calculate SOS over gridpoints where we have valid data over the whole year, e.g. in northern regions SOS is not calculated.

# 3 Global comparison of vegetation products

## 3.1 Spatial comparison

As shown in Fig. IV.2 the spatial patterns exhibited by the scatterometer products follow patterns as found in  $\tau_p$  and LAI. High values are found in tropical forests, e.g. Congo, Indonesia and

Brazil, and in boreal forests, in e.g. North-America and Russia. Low values are found in drylands, especially in the central Australia, Sahel and South Africa. For  $\tau_a$ ,  $\tau_p$  and LAI a clear trend can be seen from the Sahara desert to the tropical rainforests in the Democratic Republic of Congo. For CR this trend is less pronounced. because CR shows relatively high values in dry regions compared to  $\tau_a$ ,  $\tau_p$  and LAI. This is especially clear in the Sahel and in Australia and central parts of the USA. This was also observed by McColl et al. (2014) in the RVI data. In this study the effect of noise and miscalibration of scatterometers on RVI was investigated. Scatterometers are calibrated over certain targets with a known scattering behaviour. However, miscalibration can lead to errors in the backscatter data. Using an error model which accounts for mean and amplitude biases, McColl et al. (2014) estimated the sensitivity of RVI to HV polarized backscatter. HV polarized backscatter occurs in both the numerator and denominator of RVI, hence a bias in HV data will positively bias RVI. The bias was found to be strongest in sparsely vegetated regions, where an additive bias of  $10^{-4}$  (in linear units) to the HV observations, resulted in a bias of 0.1 in RVI. Noise, however, did not lead to high biases. Hence, high values of RVI in sparsely vegetated regions were attributed to a calibration error in the cross-polarized data.  $\tau_a$  shows relatively low

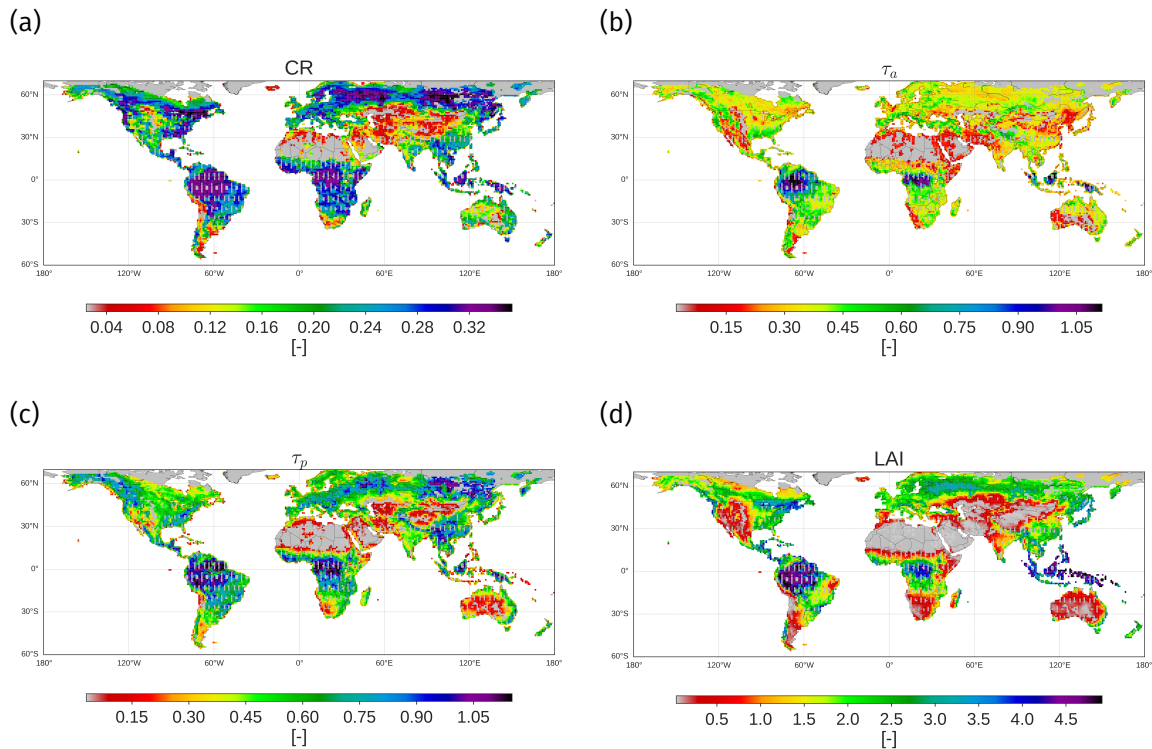
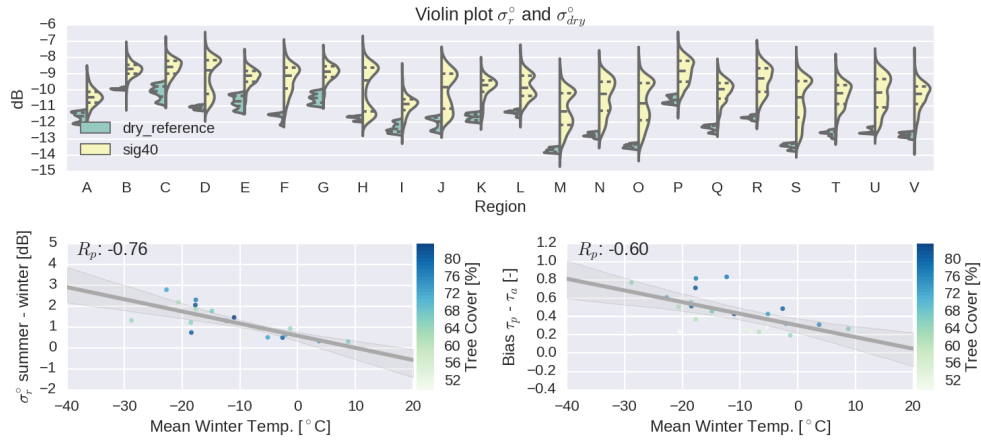


Figure IV.2: Mean values for the four vegetation products: a. CR, b.  $\tau_a$ , c.  $\tau_p$ , d. LAI.

values in boreal forests (Evergreen Needleleaf Forests, ENF, Fig. IV.1), compared to CR,  $\tau_p$  and LAI. But also comparing spatial patterns of  $\tau_a$  itself, lower values are found in boreal forests than for example in the south of Spain. These low values were already observed by Vreugdenhil et al. (2016a) who hypothesized that these are a result of the effect of frozen soils and frozen trees on the calculation of  $\sigma_{dry}^{\circ}$ . Even though the  $\tau_a$  seasonality is masked for frozen soils and snow cover conditions in every gridpoint, the mean value of  $\tau_a$  is affected by frozen soils and snow cover via the estimation of  $\sigma_{dry}^{\circ}$ . The  $\sigma_{dry}^{\circ}$  is calculated as the lowest 10% of backscatter observations over the period 2007-2015. Here outliers are removed, but no specific masking has been applied for frozen soils, because the assumption is made that frozen soils have a similar backscatter signal as dry soils (Hallikainen et al., 1984b). Hence, backscatter observed during periods of frozen soils and snow cover might be included in the lowest 10% of backscatter. In the calculation of  $\tau_a$ , the  $\sigma_{dry}^{\circ}$  acts as an additive constant and does not affect the variability and the range of  $\tau_a$ . So mean values of  $\tau_a$  can be affected by an error in the  $\sigma_{dry}^{\circ}$ . To analyse the effect of  $\sigma_{dry}^{\circ}$  and



**Figure IV.3:** Distribution of backscatter and the dry reference for the 23 different areas in evergreen needleleaf forests (top). The two lower plots depict the relation between the difference in summer (June, July, August (JJA)) and winter (December, January, February (DJF)) backscatter values compared to winter (DJF) air temperatures (left) and the bias between  $\tau_a$  and  $\tau_p$  in relation to winter (DJF) air temperatures (right). The color of the markers indicates the percentage of tree cover for the specific pixel, according to Hansen’s tree cover map. The colorbar is depicted on the right side of the two plots.

cold temperatures on  $\tau_a$  a detailed analysis on  $\sigma_r^\circ$  and  $\tau_a$  in Evergreen Needleleaf Forests (ENF) in different climates is performed. Based on the CCI Land Cover map centred in 2010 and Hansen percentage tree cover we have selected 22 locations in ENF in different latitudes, ranging from a region in Alabama to regions in Siberia and Alaska (see Fig IV.1 for exact locations). The annual average temperature and amount of days with frozen soils differs per location. Fig. IV.3a shows the distribution of  $\sigma_{dry}^\circ$  and  $\sigma_r^\circ$  from ASCAT. For some locations a clear bi-modality can be seen in  $\sigma_r^\circ$ . Where  $\sigma_r^\circ$  shows a bi-modality we also see that  $\sigma_{dry}^\circ$  is relatively low. This bi-modality most likely originates from large differences in  $\sigma_r^\circ$  observed during summer and winter time. Fig IV.3.b shows the regression between the difference in summer and winter  $\sigma_r^\circ$  values and average winter air temperature. A correlation of  $r_s = -0.76$  is found when comparing the difference between summer (JJA) and winter (DJF)  $\sigma_r^\circ$  to air temperature. This analysis shows that during winter time in ENF located in cold climates,  $\sigma_r^\circ$  can decrease dramatically, and can be up to 2 dB lower than in ENF in milder climates. When taking  $\tau_p$  as a reference, the bias between  $\tau_a$  and  $\tau_p$  also increases with decreasing air temperature, with  $r_s = -0.60$ . The error in the estimation of  $\sigma_{dry}^\circ$  propagates as an additive bias to the  $\tau_a$  seasonality. As can be seen from Fig. IV.3.c, the bias is also related to tree cover, where bias increases with increasing tree cover. This analysis supports the hypothesis of [Vreugdenhil et al. \(2016a\)](#) that frozen soil and vegetation could cause the low  $\tau_a$ -values. In the TU Wien algorithm it is assumed that frozen soils and dry soils give a similar backscatter response ([Wang and Schmugge, 1980b](#); [Hallikainen et al., 1984b](#)). However, our study infers that one needs to be careful in assuming that backscatter obtained from ASCAT during cold periods and obtained during dry periods are similar. The bias in  $\tau_a$  also affects the vegetation correction in the TU Wien soil moisture retrievals and propagates a bias in soil moisture, which was already observed by [Dorigo et al. \(2015\)](#). This study provides a basis to improve the vegetation correction and subsequently soil moisture retrieval in cold climates.

### 3.2 Temporal comparison

Fig. IV.4 shows the global maps of  $r_s$  between the different products. Moderate to high values for  $r_s$  are found in temperate and cold climates, e.g. Europe and North-America, and low correlations are mainly found over drylands (Fig IV.4). The highest median correlation is found between  $\tau_p$  and LAI with 0.59, followed by  $\tau_a$  and LAI with 0.58. CR shows the lowest correlation coefficients

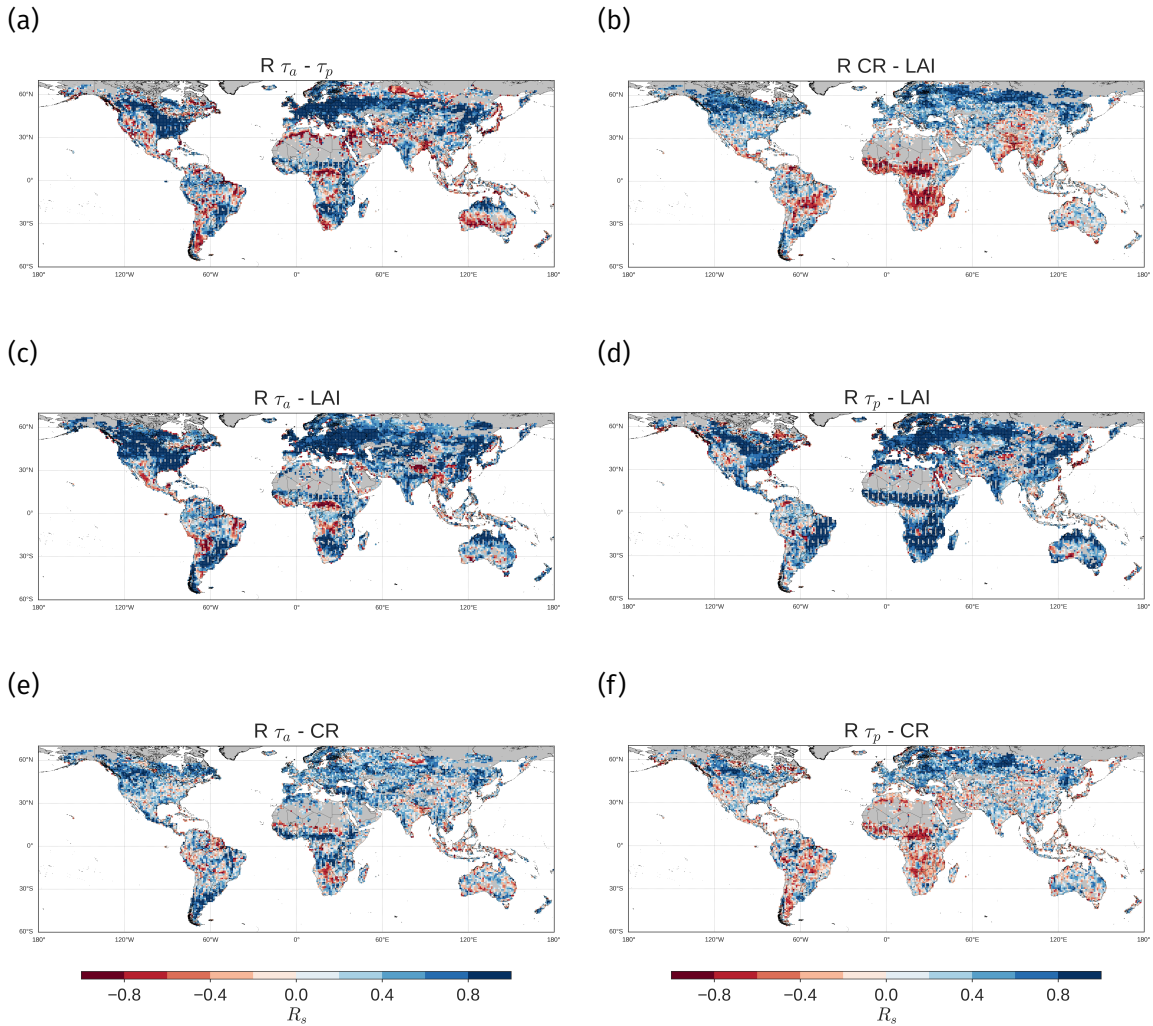


**Figure IV.4:** Global spearman correlation coefficients  $r_s$  between the different products: a.  $\tau_a - \tau_p$ , b. CR - LAI,  $\tau_a - LAI$ , d.  $\tau_p - LAI$ , e.  $\tau_a - CR$ , f.  $\tau_p - CR$ . Red areas indicate negative correlation coefficients and blue indicate positive correlation coefficients.

with the other products, with values of 0.12, 0.19 and 0.33 for  $\tau_p$ , LAI and  $\tau_a$  (Table IV.2). This could be a result of the relatively noisy signal of CR or the different frequency of Aquarius. When the vegetation is sparse, the signal from vegetation may be lower than the noise level. Where  $\tau_a$  and  $\tau_p$  are derived from C-band observations, CR is derived from L-band. With the longer wavelength of Aquarius it is assumed to be less sensitive to the vegetation canopy but comparably more to the woody part of the vegetation (Cui et al., 2015), which could possibly lead to the lower correlation between CR and the other products.

Looking at the distribution of  $r_s$  for different CCI Land Cover classes (Fig. IV.5 and Table IV.2) it becomes clear that both  $\tau$ -products show a strong correspondence with LAI in most land cover classes, but especially in croplands and grasslands, where in croplands the median  $r_s$  is as high as 0.74 and 0.79 for  $\tau_a$  and  $\tau_p$  respectively. In grasslands the median  $r_s$  is slightly lower with 0.72 and 0.62 for  $\tau_a$  and  $\tau_p$ . These high correlation coefficients ( $r_s > 0.5$ ) between all products over croplands and grasslands can be found in Europe, North-America and northern parts of Asia (Fig. IV.4). In sparsely vegetated regions and shrublands  $r_s$  is relatively high between  $\tau_a$  and LAI (0.48 and 0.52), and  $\tau_p$  and LAI (0.46, 0.64). However, in shrublands and sparsely vegetated regions negative correlations can also occur, e.g. Central Australia and northern Africa (Fig. IV.4). Very low backscatter, i.e. lower than -20 dB, could be contaminated by noise and changes in

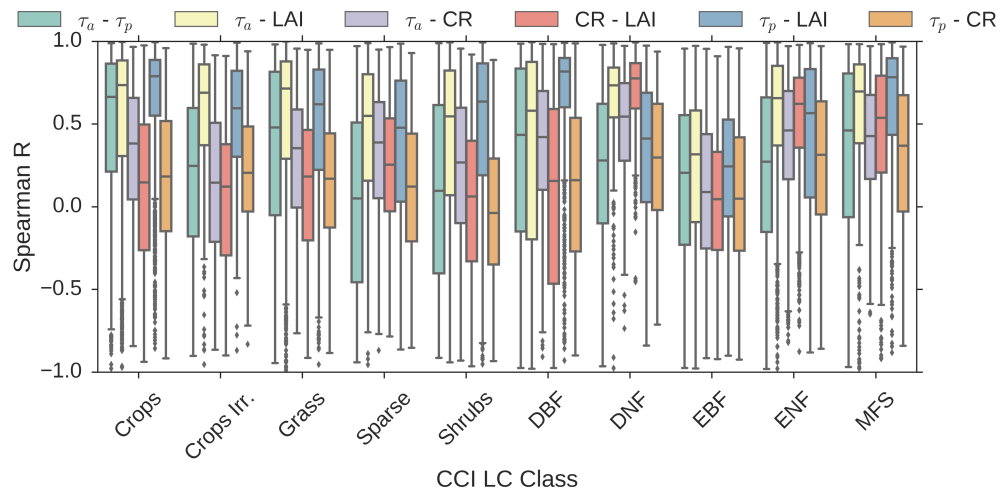


**Figure IV.5:** Boxplot of  $r_s$  for different land cover classes based on the CCI Land Cover dataset the colors depict the following combinations: green:  $\tau_a - \tau_p$ , yellow:  $\tau_a - \text{LAI}$ , purple:  $\tau_a - \text{CR}$ , pink:  $\text{CR} - \text{LAI}$ , blue:  $\tau_p - \text{LAI}$  and orange:  $\tau_p - \text{CR}$ . The acronyms can be found in Table IV.2

**Table IV.2:** Median values per CCI Land Cover Class for  $r_s$  between the different products.

CCI Land Cover Class	$\tau_a - \tau_p$	$\tau_a - \text{LAI}$	$\tau_a - \text{CR}$	$\text{CR} - \text{LAI}$	$\tau_p - \text{LAI}$	$\tau_p - \text{CR}$
<b>Global</b>	0.33	0.58	0.31	0.19	0.59	0.12
<b>Croplands</b>	0.66	0.74	0.38	0.15	0.79	0.18
<b>Croplands Irrigated</b>	0.25	0.69	0.15	0.12	0.60	0.21
<b>Grassland</b>	0.49	0.72	0.36	0.20	0.62	0.19
<b>Sparsely vegetated</b>	-0.04	0.48	0.34	0.22	0.46	0.12
<b>Shrubland</b>	0.08	0.52	0.26	0.05	0.64	-0.05
<b>Deciduous Broadleaf Forest (DBF)</b>	0.44	0.57	0.42	0.13	0.82	0.16
<b>Deciduous Needleleaf Forest (DNF)</b>	0.68	0.67	0.55	0.68	0.67	0.45
<b>Evergreen Broadleaf Forest (EBF)</b>	0.21	0.32	0.09	0.05	0.25	0.05
<b>Evergreen Needleleaf Forest (ENF)</b>	0.32	0.68	0.41	0.60	0.61	0.34
<b>Mixed Forest/Shrubland (MFS)</b>	0.54	0.71	0.42	0.53	0.80	0.41

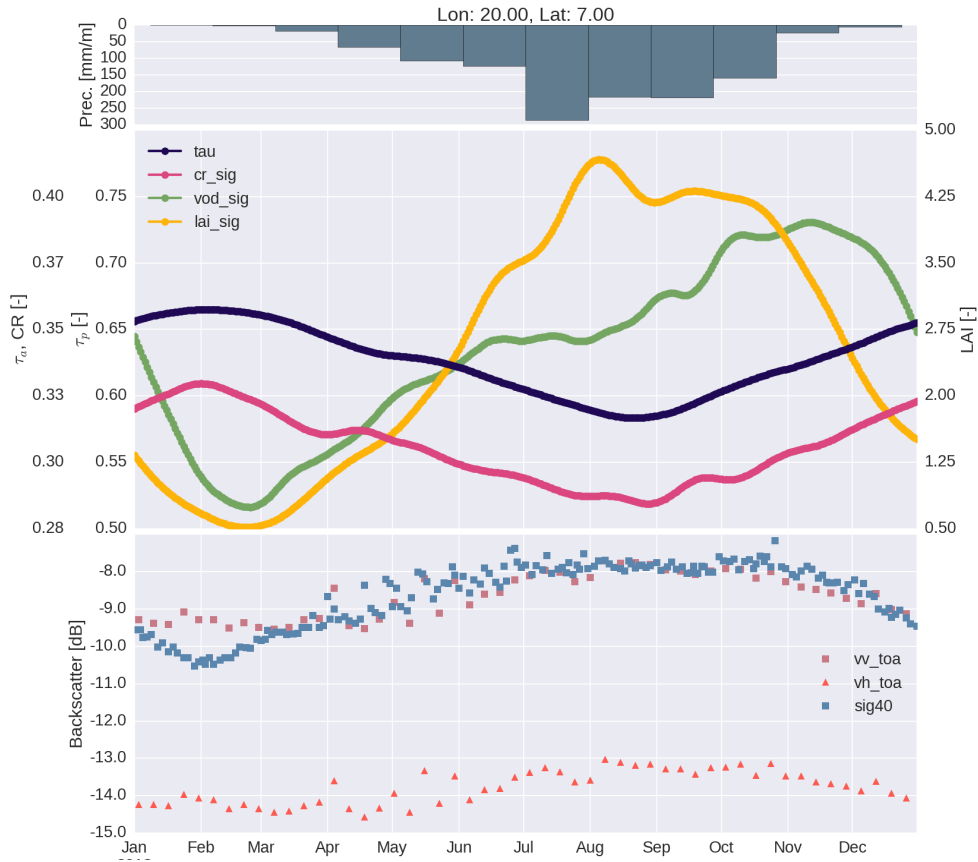


**Figure IV.6:** Time series of climatologies of all four vegetation products, ASCAT VV, Aquarius VH and VV and precipitation for one  $1^\circ$  pixel over Central African Republic at longitude 20.00 and latitude 7.00. The top barplot depicts the average precipitation per month over the period 2007 - 2013. The middle plot depicts the seasonalities of vegetation products in yellow: LAI, green:  $\tau_p$ , pink: CR, blue:  $\tau_a$ . The lower plot depicts the backscatter data over the year 2013 of Aquarius (VV in purple squares, VH in red triangles) and ASCAT VV (blue squares).

the  $\sigma_r'$  can no longer be reliably related to geophysical processes like vegetation dynamics. In Deciduous Needleleaf forests moderately high correlations are found between all four products, varying between 0.45 and 0.68. In Fig. IV.4 we can see that lower correlations between all products are found in some northern regions, e.g. Canada. These regions correspond to flooded areas in Fig. IV.1. Here many lakes, wetlands and river can be found, but also water can pond on the surface during thawing in spring. Open water has a strong effect on microwave observations, where scatterometers are sensitive to the direction of wind and waves on the water surface. Also  $\tau_p$  is found to be affected by open water as was discussed in [Gouweleeuw et al. \(2012\)](#). For the same reason negative correlations are found between most products in irrigated and flooded cropland, for example in the Ganges Delta and eastern China. In northern regions, which are characterized by boreal forests (ENF) we find highest correlation between  $\tau_a$  and LAI where  $r_s$  is 0.68. Slightly lower  $r_s$  its found between  $\tau_p$  and LAI, 0.61 respectively. As discussed in the previous section, mean values of  $\tau_a$  are most likely biased but are not affected temporally. This is also suggested by the high values for  $r_s$  that we find here. In addition, moderately high values for  $r_s$  are found between Aquarius and LAI and Aquarius and  $\tau_a$ , 0.60 and 0.41 respectively. In tropical forests (Evergreen Broadleaf Forests (EBF) in Fig. IV.5) no clear correlation is found, i.e. median  $r_s$  varies between 0.05 and 0.32, where highest values for  $r_s$  are found between  $\tau_a$  and LAI. These low values for  $r_s$  can be easily explained since there is little variation in vegetation in these areas, so that  $r_s$  as a metric is meaningless ([Vreugdenhil et al., 2016a](#)).

In Deciduous Broadleaf Forests relatively low values for  $r_s$  between  $\tau_a$  and LAI are found compared to  $\tau_p$  and LAI, 0.57 and 0.82 respectively. Strong negative correlations between  $\tau_a$  and  $\tau_p$  and LAI are found in the Central African Republic and southern parts of Congo and Brazil, regions that correspond to Deciduous Broadleaf Forests. Positive correlations are found between CR and  $\tau_a$ , but both show negative correlations with  $\tau_p$  and LAI. Fig. IV.6 shows the time series for all four products and normalized backscatter from ASCAT and Aquarius for a gridpoint (Lon: 20.00, Lat: 7.00) where we encounter negative  $r_s$ . LAI and  $\tau_p$  follow the expected pattern where the minima occur during the driest period, one month before the rain season starts. CR and  $\tau_a$  follow an opposite pattern. For ASCAT and Aquarius observations the VV-signal increases with increasing precipitation. Co-polarized backscatter is sensitive to both vegetation and soil moisture, and the VV-signal follows precipitation and soil moisture in this area. The cross-polarized VH-signal also increases with increasing precipitation, but as can be inferred from CR, less than the co-polarized VV-signal. For  $\tau_a$  the slope and curvature of the backscatter-incidence angle relationship control the temporal variation. Since we see the same behaviour in CR, the problem does not seem to lie in the TU Wien retrieval algorithm, but is more likely a difference in response to defoliation between active and passive microwave observations. For example, [Dobson and Ulaby \(1986a\)](#) showed that when defoliating corn the slope of the backscatter-incidence angle curve decreases. This was attributed to the fact that the signal from the stalks and cobs is very significant but is attenuated by foliage when present. In addition, [Macelloni et al. \(2001\)](#) observed that in broadleaf crops, with thick stalks, the backscatter is dominated by leaves when they are present and the backscatter from stalks and the soil is attenuated. [De Matthaëis et al. \(1994\)](#) found that L-band VV-observations from defoliated corn and maple are presumably dominated by double-bounce scattering mechanisms. [Hong and Wdowinski \(2014\)](#) argues that CR represents both volume scattering and double-bounce scattering and that the relation between the two depends on vegetation density. In DBF it is likely that the signal from stalks, stems and branches is attenuated by leaves, but becomes more important when leaves fall, which leads to a decrease in the slope (decreasing steepness of the  $\sigma^\circ$  and  $\theta$  relationship). In the current  $\tau_a$  retrieval, this is then interpreted as an increase in  $\tau_a$ . Further research is conducted on how to account for different scattering behaviour within the  $\tau_a$  retrieval, but also within the operational TU Wien soil moisture retrieval algorithm.

### 3.3 Phenology comparison

Fig. IV.7 and Fig. IV.8 show SOS and POS for all four datasets on a global scale. CR,  $\tau_a$ ,  $\tau_p$  and LAI show patterns which follow general precipitation and climate regions. The general patterns of SOS and POS coincide between the different products. With SOS in March to June and POS in June to August in temperate climates in the Northern Hemisphere, i.e. the eastern part of North America, Europe and south-eastern China. In the Southern Hemisphere SOS falls in November to January and POS falls in January to May. In the Sahel region SOS is found to vary from June to October. Here it also becomes clear that CR does not show as much temporal detail as the other products. CR follows the general temporal patterns as found in the other products, but patterns are not as clear. The CR data is relatively noisy and heavily affected by RFI. The lack of data and the noisy character makes it difficult to calculate reliable seasonal curves. Hence, we do not discuss any phenology metrics from CR in the rest of this section.

[Jones et al. \(2012\)](#) calculated SOS over North America using a Gaussian fit smoothing and a threshold of 10%. Hence, we cannot directly compare our findings of SOS to those of [Jones et al. \(2012\)](#), but we do observe similar patterns. For  $\tau_p$ , [Jones et al. \(2012\)](#) found SOS to vary from the end of February to the beginning of April in southern regions. We find similar values for SOS in  $\tau_a$  and  $\tau_p$ , where in southern regions SOS falls in March to May. Both VNIR products, NDVI in [Jones et al. \(2012\)](#) and LAI in our study, exhibit similar patterns for SOS. In southern regions SOS varies from the beginning of March to the end of June, usually concordant with or preceding  $\tau_p$ . We find slightly later SOS values compared to [Jones et al. \(2012\)](#), in April and May, in part due to the different thresholds adopted in [Jones et al. \(2012\)](#) (10%) and in our analysis (50%). For arid, sparsely vegetated regions in North America we see similar values in LAI and  $\tau_p$ , with SOS

values around July-August. However, contradicting values are found for  $\tau_a$  compared to Jones et al. (2012), where SOS is in February for  $\tau_a$ . This is most likely caused by the issue that in these regions  $\tau_a$  is not sensitive to vegetation but to other parameters, as is indicated by the negative correlations between  $\tau_a$  and LAI we observe in these regions. In an older study, Moulin et al. (1997) derived POS for NDVI over the year 1986 and found that POS in regions between 40° and 75° were very similar, corresponding to the end of July. We find similar values, where POS varies between June and August over North America and Europe.

Over Africa there is a clear gradient in  $\tau_p$  and LAI SOS values from March-April (Fig. IV.7) in tropical regions and in July-August in the Sahel region (Fig. IV.7). For  $\tau_a$  this pattern is less clear, but in the Sahel region similar timing is found for SOS. For LAI POS values shift from July-August in the tropical regions to September-October in the Sahel. In  $\tau_a$  and  $\tau_p$  no clear values for POS are found in tropical regions, most likely because there is not much variation in this region. Over the Sahel region POS shifts from September in the north to October in the south. This shift coincides with the shift in start and peak of the rain season in these areas which moves with the Inter-tropical Convergence Zone. Tian et al. (2016) found similar results over drylands in the West African Sahel zone from a latitude of 13°N to 17°N. They found a peak in NDVI in September in the whole study region. For  $\tau_p$  they found a peak in September in northern regions and in October in southern regions, which led to a lag of a month between LAI and  $\tau_p$ . In southern parts of Africa we see a very clear pattern, with SOS values in November-January and POS values in March-May. These regions are characterized by a strong seasonality, as also found in the Sahel. In Australia we see similar patterns between the different products. The rain season in southern Australia is during the Australian winter which coincides with a SOS from April-July and POS from August-November. Here  $\tau_a$  shows again opposite values, since we found negative correlation between  $\tau_p$ , LAI, and  $\tau_a$ . In the northern regions of Australia the rain season is controlled by the monsoon, which brings rain during the Australian summer, October to April. Here, SOS falls in December-February and POS in March-May. Naturally, large differences in timing arise in DBF over the Central African Republic, Brazil and southern Congo, where the active products showed a negative  $r_s$  with LAI and  $\tau_p$ .

Spatial patterns of the differences in SOS and POS between  $\tau_a$  and  $\tau_p$ , and LAI, are similar (Fig. IV.9). Largest differences between  $\tau_a$ ,  $\tau_p$ , and LAI are found in tropical forests where no clear seasonal cycle is present. In north-west Europe, SOS, and to a lesser extent POS, derived from microwave observations precede LAI (red areas in Fig. IV.9), with a maximum of two months (60 days). In central Europe and south-east USA POS is later for the microwave products than for LAI. In cold climates, e.g. Scandinavia, Russia and northern Canada and Alaska, POS of  $\tau_a$  precedes LAI (red areas in Fig. IV.9b), whereas  $\tau_p$  follows LAI (blue areas in Fig. IV.9d). As discussed in Section 3.2, parts of these regions are likely affected by open water. Subsequently, POS values might differ here between the different products. Jones et al. (2012) compared SOS found in NDVI and  $\tau_p$ , and found that SOS of  $\tau_p$  precedes NDVI in cold regions. It was suggested that this could be due to plant physiological regulation of canopy water content, where with thawing water from the stems is transported to existing leaves, before producing new leaves and green-up. In warm climate regions, where vegetation consists of savannah, shrubland and forest, e.g. the south of Spain and southern Sahel region, we find that the microwave products follow LAI (blue areas in Fig. IV.9). Focusing on the Sahel region we can see a gradient from north to south where the lag between LAI and the microwave products seems to increase. This can be seen both for  $\tau_a$  and  $\tau_p$ . This pattern was already observed for  $\tau_p$  in several previous studies and is attributed to the different sensitivity of microwave products and VNIR products (Liu et al., 2011; Wagner et al., 1999a; Andela et al., 2013; Guan, 2013; Tian et al., 2016; Jones et al., 2011, 2012). Where VNIR products are found to be sensitive to the top of the canopy and grasses, microwave products are assumed to be sensitive to the total vegetation water content and above ground biomass. Over the Sahel region, Jones et al. (2011) found a phase shift between  $\tau_p$  and three MODIS vegetation indices, NDVI, LAI and EVI, and the Growing Season Index. This shift increased when moving south from grasses to savannah to woody savannah. Guan (2013) found that NDVI and  $\tau_p$  are tightly coupled over African grasslands, but that they start to deviate in African woodlands where  $\tau_p$  exhibits a slower increase and a later peak compared to NDVI. Tian et al. (2016) inferred from

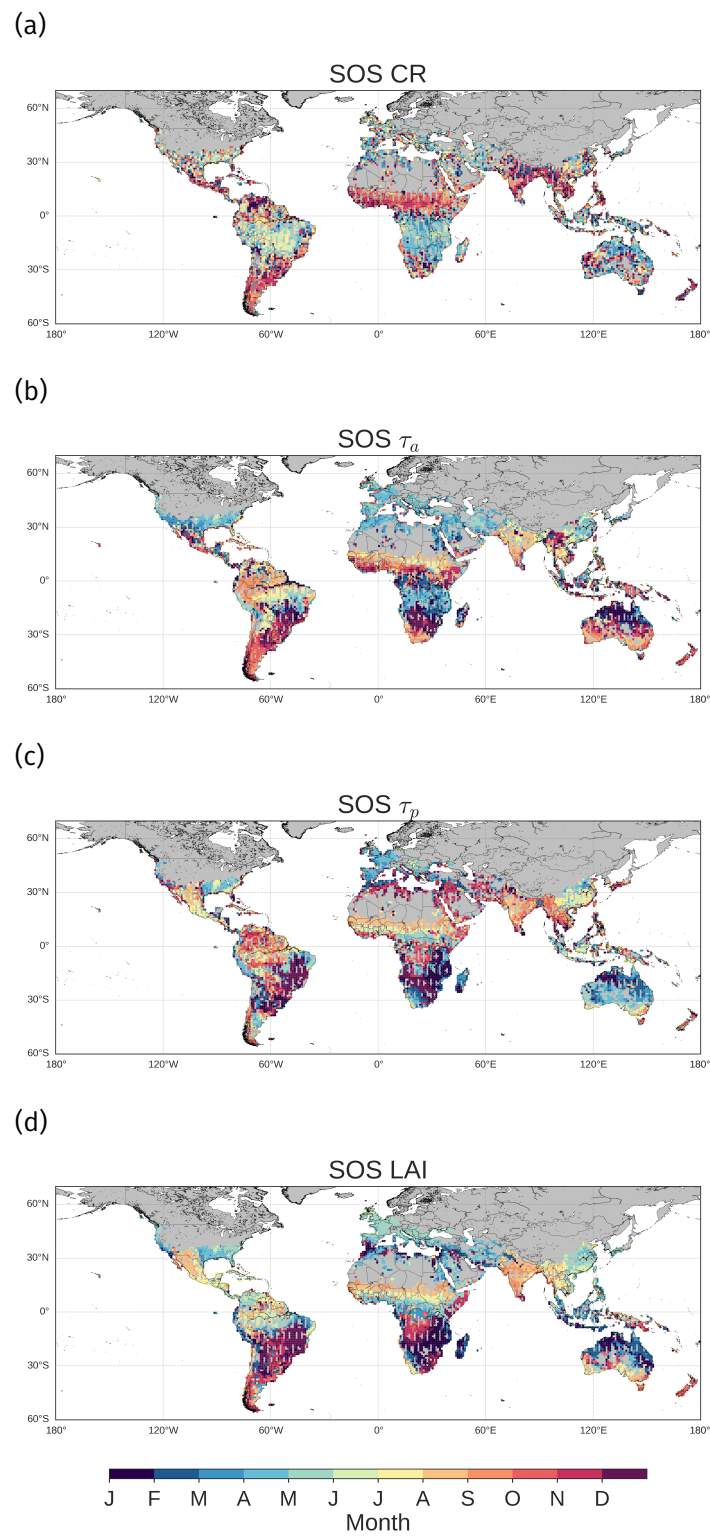


Figure IV.7: Timing of SOS in month of the year for the four vegetation products: a. CR, b.  $\tau_a$ , c.  $\tau_p$ , d. LAI.

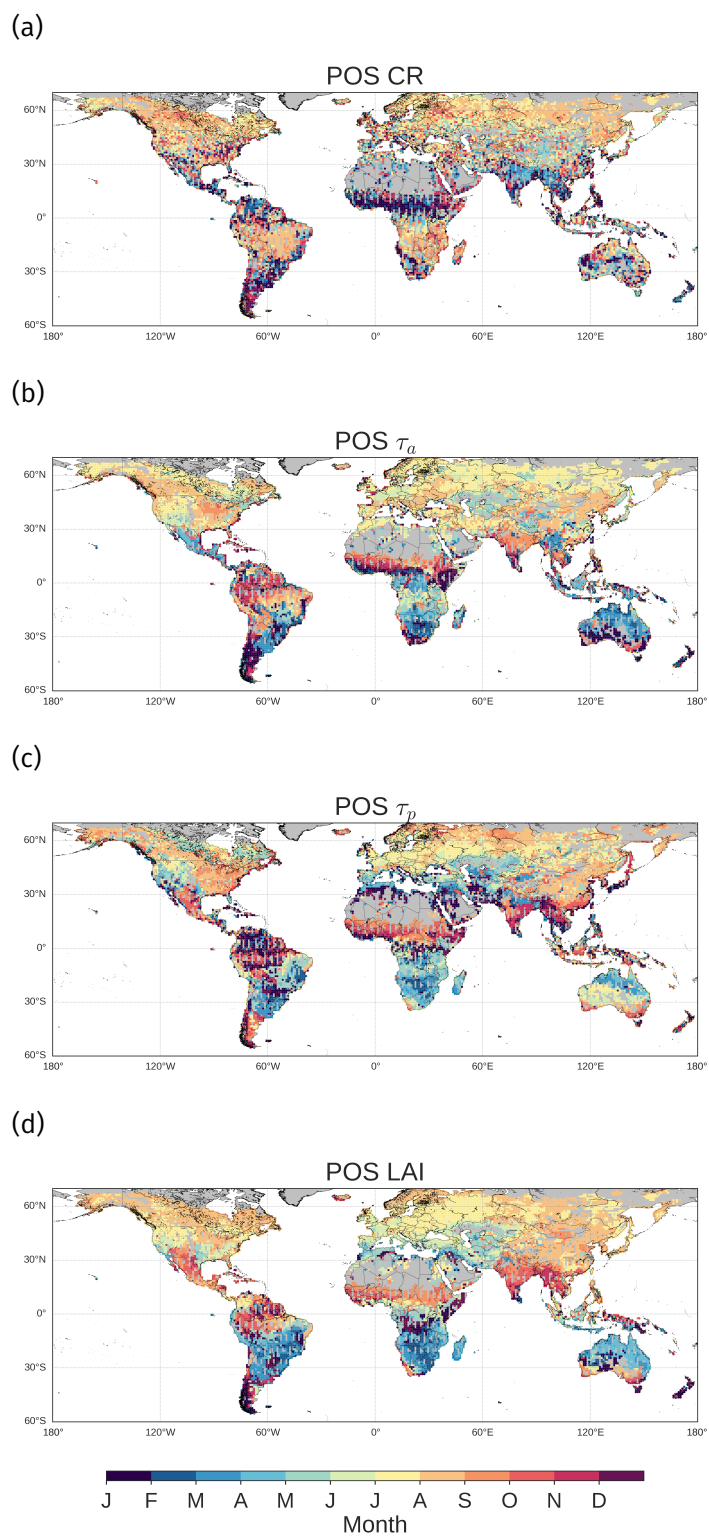
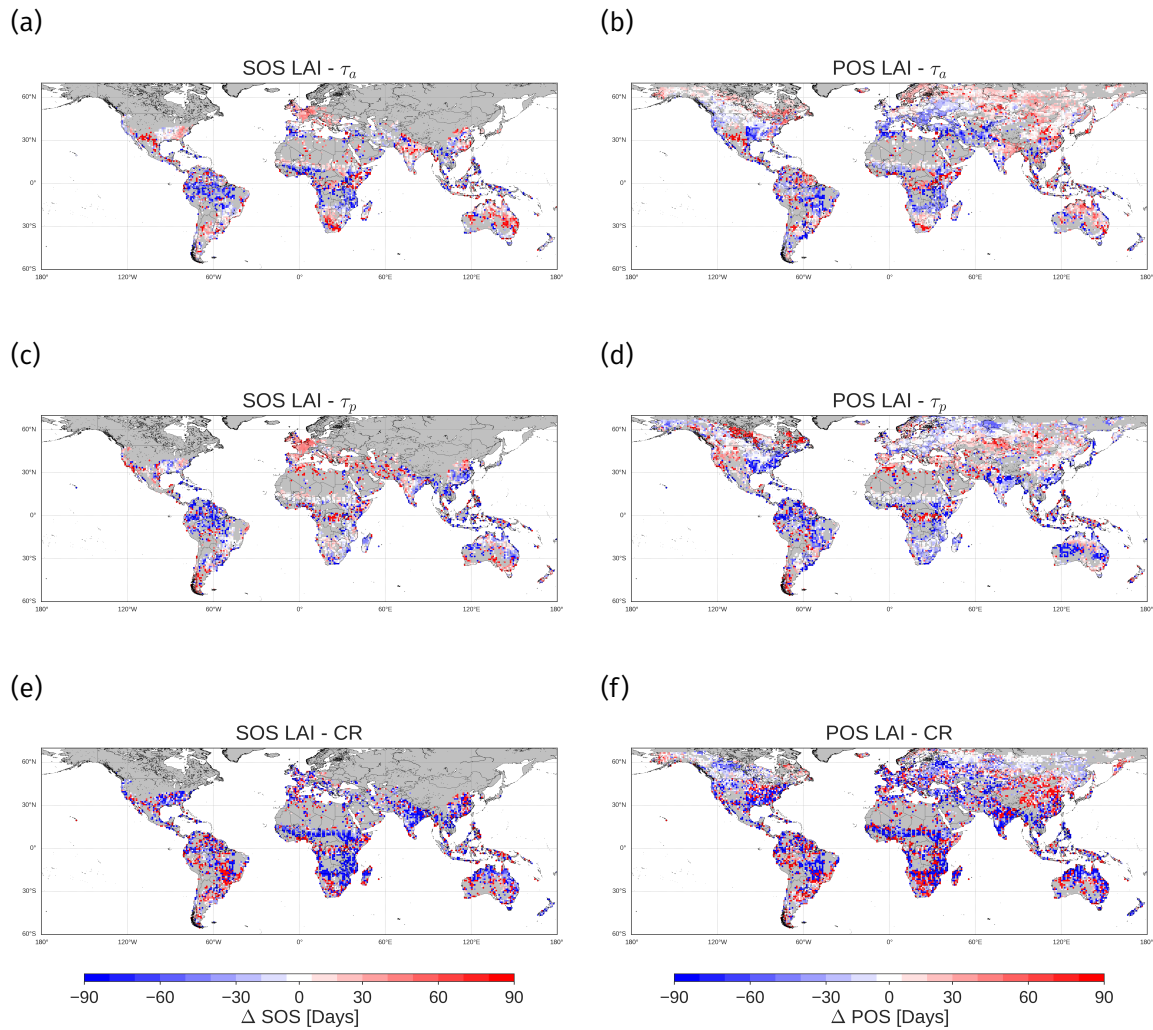


Figure IV.8: The timing of POS in month of the year for the four vegetation products: a. CR, b.  $\tau_a$ , c.  $\tau_p$ , d. LAI.



**Figure IV.9:** Difference in days between the three microwave products,  $\tau_a$ ,  $\tau_p$  and CR, and LAI for SOS (left column) and POS (right column). Red colors represent areas where LAI is later than the respective product and blue colors represent areas where LAI is earlier than the respective microwave product.

*in situ* phenological data that the lag which was found between NDVI and  $\tau_p$  over the West African Sahel is related to the later peak time of woody plant foliage (and likely the water content in the woody component). And Jones et al. (2012) found a relationship between the lag and woody vegetation cover; the lag between NDVI and  $\tau_p$  increased with increasing woody biomass. It was assumed that  $\tau_p$  becomes less sensitive to understory response, and more sensitive to overstory biomass, when woody vegetation cover increases. From these studies we can infer that the increasing lag between LAI and the microwave products which is observed in the Sahel region can be explained by an increase in woody vegetation cover from the northern part of the Sahel to the southern part of the Sahel.

The similar patterns in phenological parameters between  $\tau_a$  and  $\tau_p$  in most regions, suggests that  $\tau_a$  and  $\tau_p$  are sensitive to similar parts of the vegetation. Both products exhibit a difference with LAI phenological parameters which are related to the different sensitivity of microwave products and VNIR products. This comparison is a first step in suggesting that  $\tau$  retrieved from scatterometers is able to describe vegetation dynamics. CR derived from Aquarius observations is found to be not suitable to estimate phenological parameters but this is likely due to the noisy character of Aquarius data. When longer data time series of cross-and co-polarized become available this may become possible.

## 4 Conclusions

This study provides a comparison between four vegetation datasets which are derived from different spaceborne sensors. A spatial comparison of the vegetation products derived from scatterometers to existing and validated vegetation products from passive microwaves and VNIR observations illustrates that the scatterometer products follow general vegetation patterns. However, in boreal forests  $\tau_a$  shows low values compared to the other products, which are possibly caused by an additive error originating from the TU Wien soil moisture retrieval algorithm in these regions. The temporal comparison shows a strong temporal correspondence between  $\tau_a$ ,  $\tau_p$  and LAI, especially over croplands and grasslands. As previous studies have validated both LAI and  $\tau_p$ , our results suggest that  $\tau_a$  is sensitive to temporal dynamics in vegetation. CR shows relatively low values for  $r_s$ , which can be caused by noise, or is due to the different frequency of Aquarius. The effect of frequency on vegetation retrievals will be investigated in future studies. The seasonality of CR and  $\tau_a$  exhibit a different behaviour compared to LAI and  $\tau_p$ , indicating a disparity between active and passive microwaves. These results instigate further research on the different scattering mechanisms in deciduous forests, especially on the contribution of different parts of woody vegetation and the effect of double-bounce scattering.

Even though there are significant differences between CR and LAI and  $\tau_p$ , on a global scale CR does behave similar as  $\tau_a$  especially in forests. Hence, VH-data could potentially be used to parameterize vegetation if observations are not taken under different incidence angles. This is valuable information for e.g. ESAs Sentinel-1 missions which obtain VV-VH observations over land. Moreover, VH-data can help improve vegetation parameterization of vegetation when VV-data is available under different incidence angle, as for EUMETSATs planned Polar System - Second Generation Scatterometer mission (EPS-SG SCA). Further studies will focus on the effect of different wavelengths on the vegetation products, in order to further understand which part of the vegetation is described by CR and  $\tau$ .

## Acknowledgments

The activities were carried out within the project: “Use of SCA cross-polarization information for soil moisture retrieval”, funded through EUMETSAT ITT 14/208518. The authors would also like to acknowledge financial support from the Austrian Science Funds FWF as part of the Doctoral Programme on Water Resource Systems (DK-plus W1219-N22) and the Satellite Application Facility on support to operational hydrology and water management (H-SAF).

The SPOT-VGT LAI dataset was generated by the land service of Copernicus, the Earth Observation programme of the European Commission. The research leading to the current version of the product has received funding from various European Commission Research and Technical Development programmes. The product is based on SPOT/VGT 1km data ((c) CNES and distributed by VITO). We would also like to thank the ESA Climate Change Initiative Land Cover project (2014) for providing Land Cover data.

# Chapter V

## Assessing Vegetation Dynamics over Australia using Metop ASCAT.

Mariette Vreugdenhil, Sebastian Hahn, Thomas Melzer, Bernhard  
Bauer-Marschallinger, Christoph Reimer, Wouter Dorigo and Wolfgang Wagner

This chapter is based on a paper which is accepted for publication in  
*IEEE Journal of Selected Topics in Applied Earth Observations and Remote Sensing*. October 2016.

© 2016 IEEE

*The layout has been revised.*

## Abstract

Recently, the slope and curvature estimation of the backscatter - incidence angle relationship within the TU Wien retrieval algorithm has been improved (Melzer, 2013). Where previously only climatologies of the slope and curvature parameters were available, i.e. one value for every day of year, slope and curvature are now calculated for every day. This enables the retrieval of time series of vegetation optical depth ( $\tau_a$ ) from backscatter observations. This study demonstrates the ability to detect inter-annual variability in vegetation dynamics using  $\tau_a$  derived from backscatter provided by the Advanced Scatterometer on-board Metop-A.  $\tau_a$  time series over Australia for the period 2007 - 2014 are compared to Leaf Area Index (LAI) from SPOT-VEGETATION by calculating rank correlation coefficient ( $r_s$ ) for original time series and anomalies. High values for  $r_s$  are found over bare soil and sparse vegetation in central Australia with median  $r_s$  values of 0.78 and 0.58, respectively. Forests and ephemeral lakes and rivers impact the retrieval of  $\tau_a$  and negative values for  $r_s$  are found in these areas. Looking at annual averages of  $\tau_a$ , LAI and surface soil moisture, significantly high values are found for the anomalously wet years, 2010 - 2011. Patterns in increased  $\tau_a$  correspond to regions with increased soil moisture and Leaf Area Index. Especially in sparsely vegetated regions, values for  $\tau_a$  and LAI are anomalous, where the flush of grasses increases  $\tau_a$  and LAI. Regions with enough precipitation and higher woody vegetation component show a smaller increase in 2010 - 2011. This study demonstrates the skill of  $\tau_a$ , and subsequently of scatterometers, to monitor vegetation dynamics thanks to the multi-incidence angle observation capability.

## 1 Introduction

Scatterometers provide backscatter observations which can be used to monitor various ocean and land surface processes. Originally designed to monitor ocean winds, scatterometers are now also used for the retrieval of surface soil moisture and vegetation dynamics. In the late 90's, an algorithm was developed based on a change detection method, the TU Wien algorithm, to retrieve surface soil moisture from backscatter observations ( $\sigma^\circ$ ). The algorithm makes use of the capability of scatterometers to observe a target under a range of incidence angles ( $\theta$ ) Wagner et al. (1999b). The algorithm was first applied to the ERS-1 Active Microwave Instrument (ERS-1), and later to the Advanced Scatterometer on-board Metop-A (ASCAT-A). The dependence of  $\sigma^\circ$  on  $\theta$ , the function  $\sigma^\circ(\theta)$ , can be modelled as a second-order polynomial. The slope ( $\sigma'$ ) and curvature ( $\sigma''$ ) of the function  $\sigma^\circ(\theta)$  are sensitive to vegetation dynamics; an increase in vegetation increases the  $\sigma'$  of the function  $\sigma^\circ(\theta)$ , whereas bare soils result in a lower  $\sigma'$ , as is depicted conceptually in Fig. I.1. Within the TU Wien algorithm, the  $\sigma'$  and  $\sigma''$  are used to normalize all backscatter measurements to a reference incidence angle ( $\theta_r$ ) and to correct for vegetation. As a heritage of the limited number of yearly observations available from ERS-1,  $\sigma'$  and  $\sigma''$  were calculated by considering all observations of the measurement period, in order to account for noise and ensure a full range of incidence angles. However, with the increasing amount of observations available on a yearly basis for ASCAT-A, Melzer Melzer (2013) recently demonstrated the feasibility of calculating  $\sigma'$  and  $\sigma''$  for each year individually. With this improved method, inter-annual variations in  $\sigma'$  and  $\sigma''$  can be investigated. Hahn et al. Hahn et al. (2016) (submitted in this issue) tested the robustness and performance of the new calculation method on a global scale by comparing  $\sigma'$  and  $\sigma''$  calculated from ASCAT observations from Metop-A and Metop-B (ASCAT-B) independently. Their results show a good agreement between observations from ASCAT-A and ASCAT-B. Only in areas with little slope variation, i.e. deserts and tropical forests, low correlations are found because of small signal variation. In sandy deserts high azimuthal anisotropy in combination with low backscatter leads to unreliable slope calculations. Both ASCAT-A and ASCAT-B showed seasonal variation in  $\sigma'$ , with low values (steep slope) in winter time and higher values (moderate slope) in summer. The study demonstrated that the inter-annual variations in  $\sigma'$  and  $\sigma''$  are stable and that the variability in both parameters describe real physical changes. Based on previous studies (Wagner et al., 1999b) (Vreugdenhil et al., 2016a) (Doubkova et al., 2009), these variations are hypothesized

to be linked to vegetation dynamics.

Wagner et al. (1999b) compared  $\sigma'$  retrieved from ERS-1 backscatter observations to Normalized Difference Vegetation Index (NDVI) over Spain. They found that  $\sigma'$  was not related to vegetation greenness but more strongly related to seasonal dynamics in the wet biomass of the vegetation. Recently, Vreugdenhil et al. (2016a) retrieved vegetation optical depth ( $\tau_a$ ) from ASCAT backscatter observations using  $\sigma'$  and  $\sigma''$  from the TU Wien algorithm and a simple water-cloud model (Attema and Ulaby, 1978). With this model, the temporal variation in  $\tau_a$  is entirely controlled by temporal variations in  $\sigma'$  and  $\sigma''$ . Given that only climatological values of  $\sigma'$  and  $\sigma''$  were calculated, until now only climatologies of  $\tau_a$  could be retrieved. It was demonstrated that climatologies of  $\tau_a$  satisfactorily follow global vegetation patterns and dynamics as observed in Leaf Area Index (LAI) and vegetation optical depth retrieved from passive microwave observations ( $\tau_p$ ) (Vreugdenhil et al., 2016a). However, the novel calculation of  $\sigma'$  and  $\sigma''$  for each year individually enables the retrieval of time series of  $\tau_a$ . This provides, for the first time, an opportunity to investigate the inter-annual variations observed in  $\tau_a$ . Vegetation is one of the important links in the water, energy and carbon cycle, making monitoring inter-annual dynamics and trends in vegetation is pivotal. Recently, dryland biomass was found to be an important driver of inter-annual variability of the carbon cycle (Ahlström et al., 2015). Global change affects vegetation dynamics, for example by an earlier onset of vegetation activity in spring due to increasing temperatures (Linderholm, 2006). But vegetation can also influence climate through e.g. photosynthesis and albedo (Richardson et al., 2013). The availability of additional vegetation datasets from active microwave remote sensing can help monitor dynamics in the total water content of the vegetation, which can improve our understanding on vegetation dynamics and its link to the water, energy and carbon cycle.

In this study we extend the work reported in Hahn et al. (2016) and Chapter III and Chapter IV: our main objective is to assess whether  $\tau_a$ , and thus  $\sigma'$  and  $\sigma''$ , are sensitive to inter-annual variability in vegetation dynamics. First, time series of  $\tau_a$  are compared to LAI retrieved from SPOT-VEGETATION observations and discussed in relation to the respective land cover classes (Fig. V.1). This is done for both the original time series and the anomalies. By subtracting the climatology from the signal, we can assess whether inter-annual vegetation variability, as described by LAI, is captured by  $\tau_a$ . As described in Hahn et al. (2016), the calculation of  $\sigma'$  is problematic over sandy deserts due to azimuthal anisotropy and small variation in the signal is found in tropical forests and other deserts. Therefore, we selected mainland Australia to perform the thorough quality assessment of  $\tau_a$ . Australia is characterized by an arid to semi-arid climate in its interior and sub-tropical climate in the north, providing a large range of climate and land cover conditions (Fig. V.1). Furthermore, Australia experienced one of the worst droughts on record from 2001 - 2009, the so-called Millennium Drought. This was followed in 2010 by the highest spring rainfall on record in eastern Australia. Australia, with its lack of mountain ranges, semi-arid climate and location between the Antarctic, Pacific and Indian Ocean is especially sensitive to climate modes, e.g. El Niño Southern Oscillation (ENSO), Indian Ocean Dipole (IOD) and Southern Annular Mode (SAM). In 2010, all three climate modes were in a phase generally linked to wet conditions for Australia, bringing particularly large amounts of rainfall to northern and eastern Australia; a negative IOD event co-occurred with La Niña and a positive SAM Hendon et al. (2014). On the other hand, 2010 was the driest year on record in south-west Australia (SWA), which is assumed to be less affected by ENSO van Dijk et al. (2013). Consequently, there have been important changes in vegetation in the last decade over the whole continent. The high inter-annual variability in precipitation combined with the large range of surface conditions and land cover makes Australia a perfect region to study the sensitivity of  $\tau_a$  to inter-annual variability in vegetation dynamics. To investigate the sensitivity of  $\tau_a$  to these extreme events, spatial patterns of annual mean values of  $\tau_a$ , LAI and surface soil moisture from ASCAT-A observations (©) are qualitatively analyzed. Since  $\tau_a$  is sensitive to total water content of the vegetation and thus above ground biomass, we expect to see a significant increase in  $\tau_a$  in eastern Australia in 2010 - 2011.

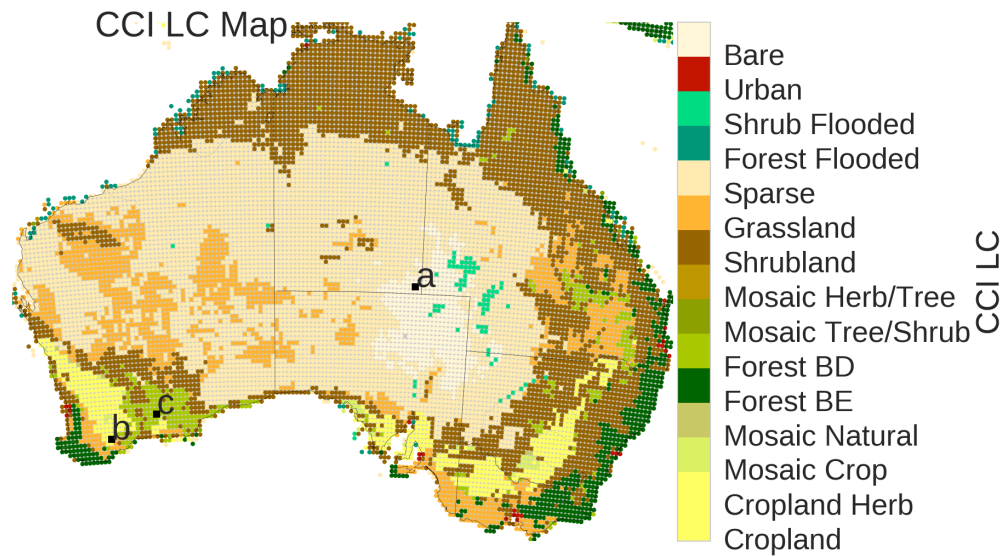


**Figure V.1:** A land cover map based on the European Space Agency's Climate Change Initiative Land Cover map of 2010. The map includes the location of the time series plots from Fig. V.5.

## 2 Data

### 2.1 Metop-A ASCAT Vegetation optical depth ( $\tau_a$ ) and Surface Soil Moisture

For this study,  $\tau_a$  is derived from model parameters from the TU Wien soil moisture retrieval algorithm using ASCAT-A observations [Vreugdenhil et al. \(2016a\)](#). ASCAT-A orbits the Earth since 2007 and provides C-band observations on a global scale every two days. Within the TU Wien algorithm, we use ASCAT-A observations resampled to a 12.5 km Discrete Global Grid [Naeimi et al. \(2009\)](#). Backscatter measurements ( $\sigma^\circ$ ) from ASCAT-A are obtained under different incidence angles ( $\theta$ ) and the dependence of  $\sigma^\circ$  on  $\theta$  can be modelled by a second-order polynomial. As described in Section 1,  $\sigma'$  and  $\sigma''$  of the function  $\sigma^\circ(\theta)$  are sensitive to vegetation dynamics and are used to normalize backscatter ( $\sigma_r^\circ$ ) to a reference  $\theta_r$  of  $40^\circ$  and to correct for vegetation. The change detection approach calculates  $\Theta$  by scaling  $\sigma_r^\circ$  between the historically lowest and highest observed backscatter, the so-called dry and wet reference respectively, which represent the driest and wettest conditions. As can be seen in Fig. I.1, cross-over angles exist, where vegetation effects on the backscatter are cancelled out. The wet reference is estimated by taking the average of the highest 10% of backscatter at the wet cross-over angle,  $\theta = 40^\circ$ , excluding outliers. Consequently, the wet reference is a constant value. The lowest backscatter is estimated at  $\theta = 25^\circ$  (Fig. I.1) and is converted back to the reference  $\theta_r$  of  $40^\circ$  using  $\sigma'$  and  $\sigma''$ . Hence, the variability in the dry reference is controlled by  $\sigma'$  and  $\sigma''$  and intrinsically corrects for vegetation. Previously,  $\sigma'$  and  $\sigma''$  were averaged over several years. Subsequently, the dry reference was only available as a function of the day of year, i.e. only 366 values were computed. Recently, the method to estimate  $\sigma'$  and  $\sigma''$  was improved by Melzer [Melzer \(2013\)](#). By using a Kernel Smoother (or weighted linear regression scheme),  $\sigma'$  and  $\sigma''$  are calculated for every single day. A detailed description of the Kernel Smoother is given in [Hahn et al. \(2016\)](#). [Vreugdenhil et al. \(2016a\)](#) used the dry and wet reference and a water-cloud model ([Attema and Ulaby, 1978](#)) to derive  $\tau_a$ . Consequently, only climatologies of  $\tau_a$  could be retrieved, i.e. 366 values. Using the novel calculation of  $\sigma'$  and  $\sigma''$ , the dry reference is available for every day, making the retrieval of  $\tau_a$  for every day possible.  $\tau_a$  is calculated as follows:

$$\tau_a = \frac{\cos \theta}{2} \ln \frac{\Delta \sigma_s^\circ}{\Delta \sigma^\circ} \quad (\text{V.1})$$

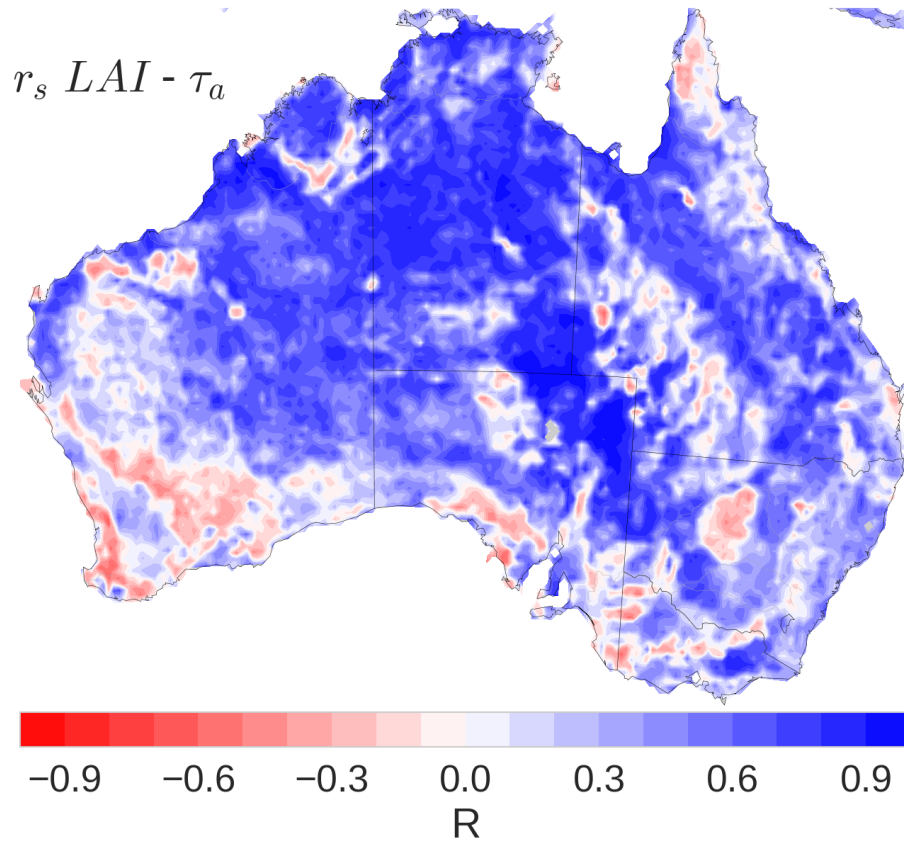


Figure V.2: Spearman Rank Correlation between Leaf Area Index from SPOT-VGT and  $\tau_a$  from ASCAT-A.

where  $\Delta\sigma^\circ$ , in  $\text{m}^2 \text{m}^{-2}$ , is the difference between the dry and wet reference.  $\Delta\sigma_s^\circ$ , also in the linear domain, represents the maximum range in backscatter values over bare soils related to a change in soil moisture only and is assumed to be constant through time. A change in  $\Delta\sigma_s^\circ$  only affects the mean value of  $\tau_a$ . The temporal variation in  $\tau_a$  is solely controlled by temporal variability in the dry reference, which is a function of  $\sigma'$  and  $\sigma''$ . The daily calculation of  $\sigma'$  and  $\sigma''$  makes it possible to compare time series of  $\tau_a$  with other vegetation products and investigate inter-annual variability.

$\Theta$  is calculated by scaling backscatter between the historically lowest (dry reference) and highest (wet reference) observed backscatter in a location. Vegetation dynamics are corrected for within the dry reference. Due to the scaling, soil moisture is available expressed in relative units of degree of saturation (%). As for  $\tau_a$ , surface soil moisture is available on a Discrete Global Grid with a grid spacing of 12.5 km. For this study both  $\tau_a$  and  $\Theta$  is resampled to a  $0.25^\circ$  grid.

## 2.2 Leaf Area Index (LAI)

LAI describes half the developed area of photosynthetically active elements of the vegetation per unit horizontal ground area. GEOV1 LAI derived from Visible and Near Infrared observations provided by the VEGETATION sensor onboard SPOT (SPOT-VGT) is used for this study (Baret et al., 2013). GEOV1 LAI is derived with a neural network, using a training dataset based on CYCLOPES v3.1 and MODIS C5 LAI to relate Top of Canopy reflectance to the best estimate of LAI. LAI is available globally as a 10-day composite with a spatial resolution of  $1/112^\circ$ . For this study LAI is resampled to a  $0.25^\circ$  grid.

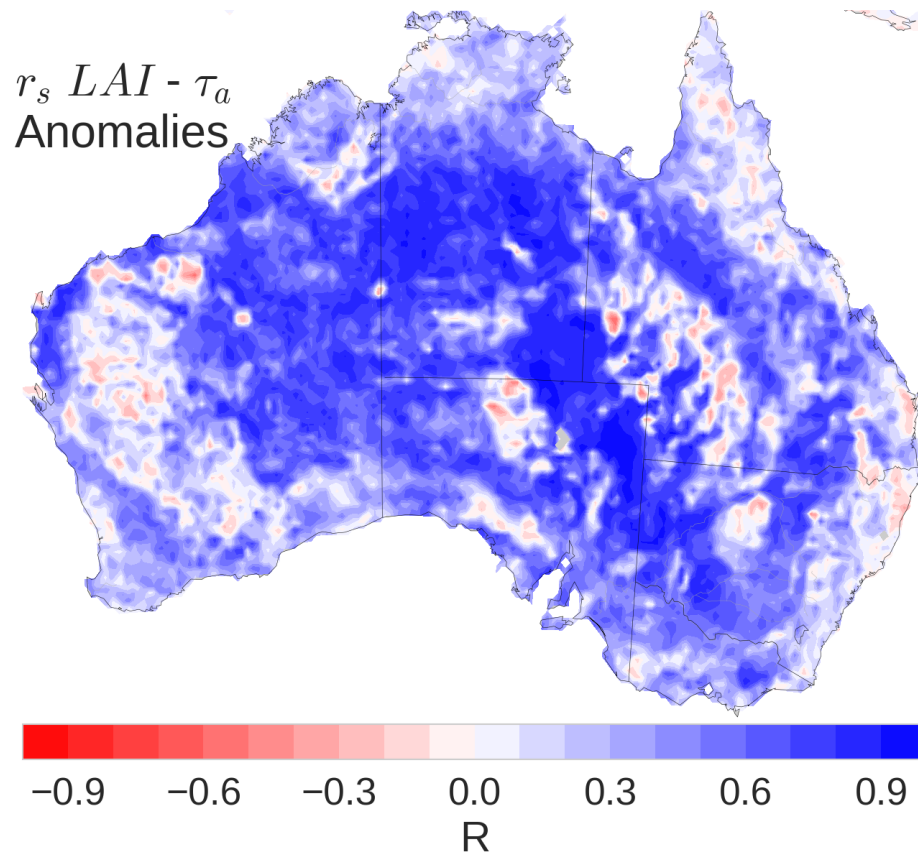


Figure V.3: Spearman Rank Correlation between anomalies from Leaf Area Index from SPOT-VGT and  $\tau_a$  from ASCAT-A.

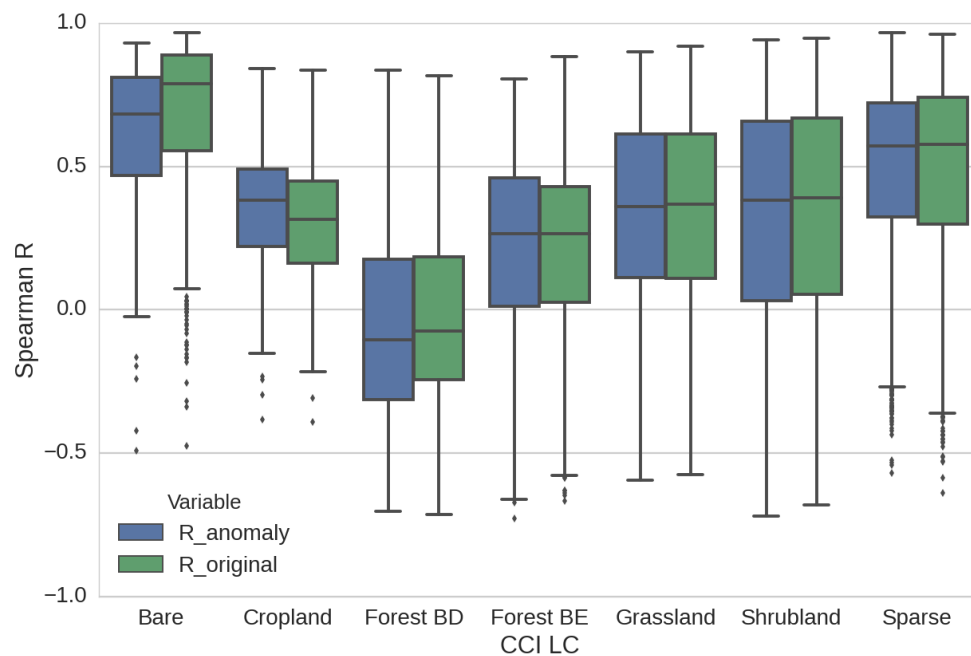


Figure V.4: Spearman Rank Correlation between GEOV1-LAI and  $\tau_a$  from ASCAT-A for original time series and anomalies grouped per CCI Land Cover Class.

### 3 Methods

To validate the performance of  $\tau_a$  over Australia, we first compare it to LAI observations from SPOT-VGT over the period 2007 - 2014. For this, all datasets are spatially resampled to a  $0.25^\circ$  grid and temporally resampled to monthly averages. For every  $0.25^\circ$  grid point in Australia, Spearman Rank Correlation is calculated for both original data ( $r_s$ ) and anomalies ( $r_{sa}$ ) of  $\tau_a$  and LAI. Anomalies are calculated by subtracting the climatology from the monthly mean values. For further analysis, grid points with a  $r_s$  lower than 0.2 are excluded. Since a lag was observed between climatologies of LAI and  $\tau_a$  (Vreugdenhil et al. (2016a)), we calculated  $r_s$  for different time lags of  $\tau_a$ . A map of monthly lag values is calculated by finding for every grid point the lag associated with the maximum  $r_s$  for that point. Lastly, an assessment of the spatial patterns of  $\tau_a$ , LAI and  $\Theta$  over the 2010 - 2011 La Niña phase is performed. To confirm if a significant increase occurs in a grid point for any of the three products, we check if the yearly mean of the 2010 - 2011 event is consistent with the ensemble of the yearly means during weak and neutral climate mode phases. We consider an increase to be significant when the mean over 2010 - 2011 is bigger than the ensemble mean plus three standard deviations of the ensemble mean. Since the ENSO cycles usually start in April/May of the first year and finishes the following year in March/April, the base for the yearly mean calculation is set in April. Spatially,  $\tau_a$  varies strongly over Australia because of the large range of climates and vegetation types, from deserts in central Australia to tropical forests in the north. At each grid point, each time series is normalized by subtracting the mean and dividing by the standard deviation, both estimated over the entire period 2007 - 2014. The resulting normalized time series facilitate the interpretation of patterns where mean and variance vary strongly from grid point to grid point.

## 4 Results and Discussion

### 4.1 Quality Assessment of $\tau_a$

Fig. V.2 and Fig. V.3 show  $r_s$  and  $r_{sa}$  per grid point over mainland Australia. In general, LAI and  $\tau_a$  show similar temporal dynamics, which is demonstrated by an average continental  $r_s$  of 0.46 (including negative values). For 71% of the grid points,  $r_s$  is higher than 0.2. Even though Hahn et al. (Hahn et al. (2016)) found unstable retrievals of  $\sigma'$  over deserts, e.g. Sahara and Takla Makan, the highest values of  $r_s$  are found over bare soils and sparse vegetation (Fig. V.4) with a median  $r_s$  of 0.78 and 0.58 respectively. Fig. V.5a and Fig. V.5b, example time series from interior Australia, show that in this region there is no clear seasonal cycle in  $\tau_a$ , but a clear inter-annual variability is found, where the highest monthly means are found in 2010 and 2011. The inter-annual variability in deserts is also captured by the anomalies in  $\tau_a$ , where the median  $r_{sa}$  is 0.68 and 0.58 for bare soils and sparse vegetation respectively. Shrubland and grassland show lower values of  $r_s$ , with medians of 0.35 and 0.37 respectively. Only on ephemeral lakes and salt pans, e.g. Lake Eyre,  $\tau_a$  does not follow LAI, which is expected due to effects stemming from open water and salt pans. Radar observations over open water are sensitive to the direction of winds and the waves on the water surface. In this case,  $\sigma'$  of the function  $\sigma^\circ(\theta)$  is strongly affected by standing water and not by vegetation.

Over croplands in New South Wales, relatively high values of  $r_s$  are found, but lower values are observed in Western Australia, leading to a median  $r_s$  of 0.32. Fig. V.5c shows time series over croplands east of Perth where a strong seasonal cycle can be observed in  $\tau_a$ , with little inter-annual variability (Fig. V.5d). Only in the winter of 2010 relatively low values for  $\tau_a$  can be observed compared to other years. This can be explained by the exceptionally dry year that western Australia experienced (van Dijk et al. (2013)). In the forested areas surrounding the agricultural regions

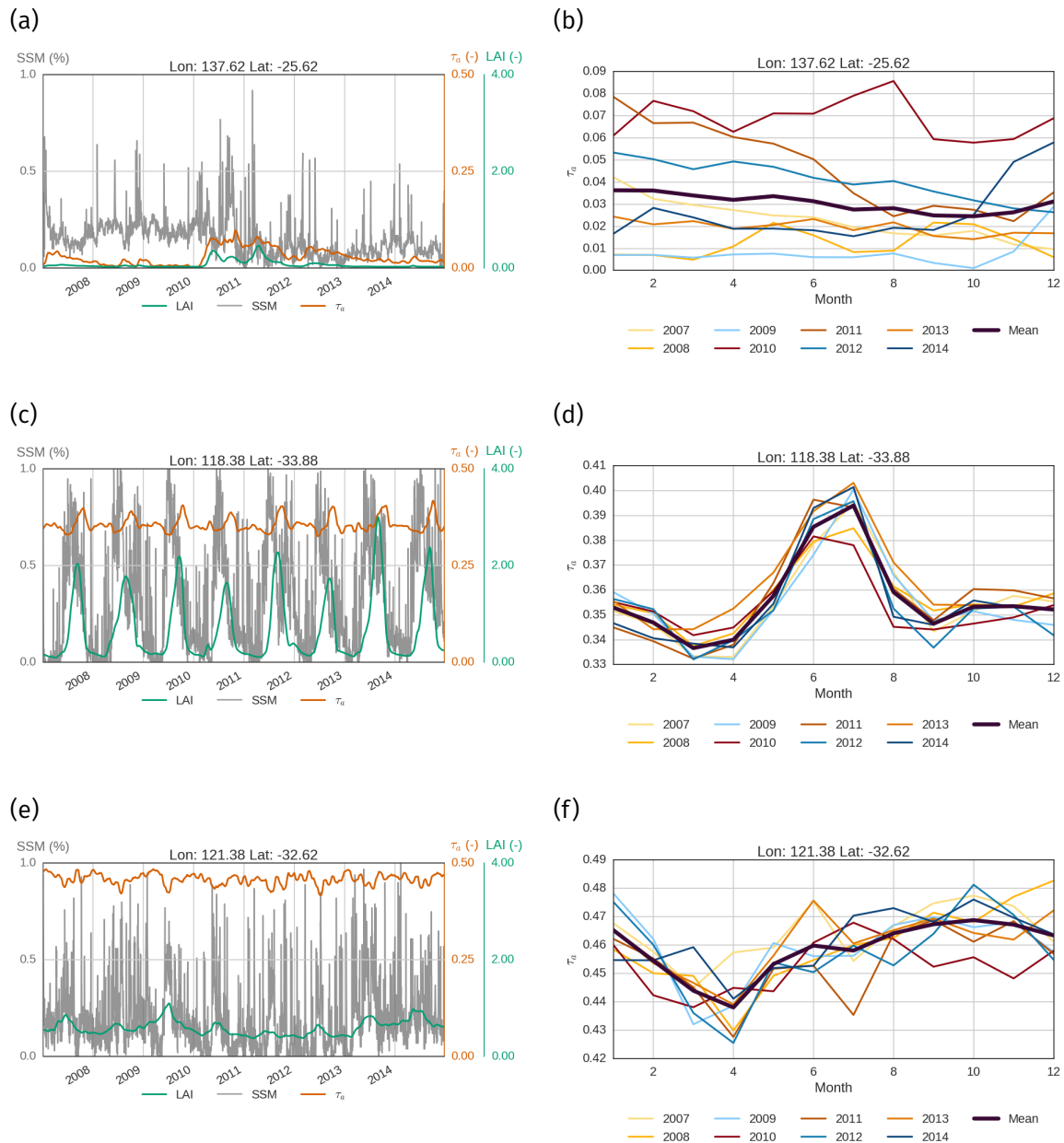


**Figure V.5:** Time series for  $\tau_a$ , LAI and  $\Theta$  (left figure) and monthly averages of  $\tau_a$  (right figure) for: a, b. interior Australia, c, d. Western Australia - croplands, e, f. Western Australia - Deciduous Broadleaf Forest. The locations of the gridpoints are depicted in Fig. V.1.

near Perth, a quick shift to negative  $r_s$  values can be observed (Fig. V.2 and V.3). The opposite behaviour of  $\tau_a$  with regard to LAI can also be observed in Fig. V.5e. Variation in  $\tau_a$  is small, but a clear seasonality can be found in the monthly time series. This indicates that there is a physical process, with a clear seasonality, which causes the opposite behaviour of  $\tau_a$  compared to LAI. These negative values are found in deciduous broadleaf forests (Forest BD in Fig. V.4) and are also observed in Vreugdenhil et al. Vreugdenhil et al. (2016b)(submitted in this issue), who attributed this behaviour to leaf fall. Leaf fall has a strong seasonal cycle, which we also see in Fig. V.5f.

In south-west Queensland and north-west New South Wales, Channel Country, areas with negative values for  $r_s$  are observed in flooded shrubland (Fig. V.1). The Channel Country river systems are some of the most variable and unpredictable flow regimes in the world Puckridge et al. (1998). Episodic floods can occur during summer monsoons in Northern Australia and this

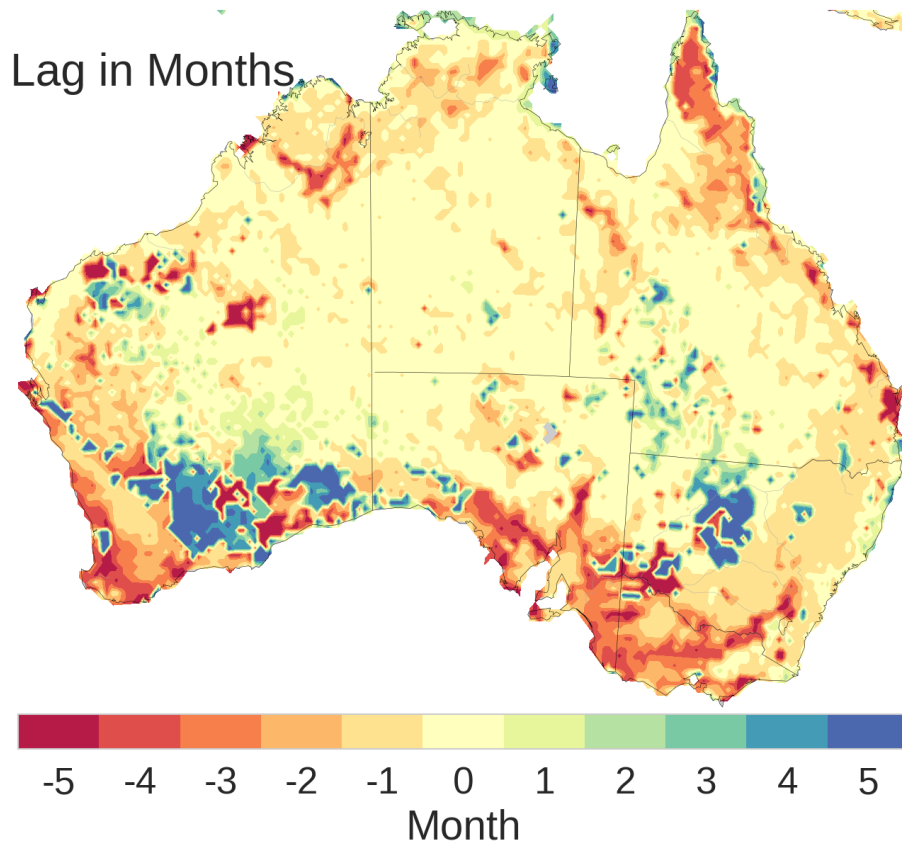


**Figure V.6:** Lag in months based on Spearman Rank Correlation between Leaf Area Index from SPOT-VGT and  $\tau_a$  from ASCAT-A. Red to orange colors indicate that  $\tau_a$  lags behind LAI.

water can fill up the anastomosing rivers in the extensive floodplain system and remain for weeks. On the other hand, there are long periods of no flow, the floodplains are dry and the little water that is available can only be found in waterholes. Also here the presence of standing water is likely to affect the estimation of  $\sigma'$ , and consequently  $\tau_a$ .

Fig. V.6 shows the lag in months between  $\tau_a$  and LAI, where negative values (red colors) indicate that  $\tau_a$  lags behind LAI. Clear spatial patterns can be observed in the lag, which correspond greatly to land cover. No lag is found for bare soils, sparsely vegetated areas and grasslands. The high values found for  $r_s$  and no lag, indicates that  $\tau_a$  is sensitive to similar vegetation dynamics as observed in LAI. A clear lag can be seen between  $\tau_a$  and LAI in croplands, with a lag of one to two months. This also explains the relatively low median  $r_s$  for croplands of 0.32. By correcting for the lag,  $r_s$  increases to 0.59 for croplands. The lag can be explained by the different vegetation characteristics represented by the two products. Since  $\tau_a$  is more sensitive to the total water content in the vegetation, including the woody part, and LAI is sensitive to the green vegetation part, differences between them are to be expected on physical grounds. Over areas which are classified as bare soil, sparse vegetation and grassland, grasses can bloom quickly after a rainfall event. If no woody vegetation is present,  $\tau_a$  and LAI are both sensitive to the grasses only. Consequently, we do not observe a lag between  $\tau_a$  and LAI. A lag was found in Jones et al. Jones et al. (2012) between  $\tau_p$  from AMSR-E observations and NDVI over the continental USA which increased with increasing woody vegetation cover. The lag was attributed to the different rooting depth of grasses and woody vegetation. After a precipitation event the rainfall is first available to grasses, which root in the upper soil layers. It was argued in Jones et al. Jones et al. (2012) that the woody biomass will only accumulate when deeper soil layers are recharged. Since we observe no lag over bare soils, sparse vegetation and grassland, and a lag of one to two months over areas with more woody vegetation cover this process could possibly also explain the observed lag between

$\tau_a$  and LAI.

The analysis of temporal correlation of original time series and anomalies between  $\tau_a$  and LAI shows that, apart from ephemeral lakes and rivers and deciduous broadleaf forest,  $\tau_a$  follows LAI. This study confirms the hypothesis of the authors of [Hahn et al. \(2016\)](#) that the variability which is seen in  $\sigma'$  is most likely driven by vegetation dynamics.

## 4.2 Inter-annual variability in $\tau_a$

The calculation of  $r_{sa}$  showed that  $\tau_a$  is sensitive to inter-annual variability in vegetation dynamics as represented by LAI in many grid points. Hence, we expect that yearly averages of  $\tau_a$  and LAI show similar spatial patterns. Fig. IV.9 shows the yearly averages for  $\tau_a$ , LAI and  $\Theta$ , in areas where  $r_s > 0.2$ . Overall, the patterns of the three products agree well. During the Millennium Drought (2007-2009), clear negative values can be seen. This is followed by two years of positive anomalies, which indicate an increase in vegetation and soil moisture. From 2012 onward values decrease slowly every year, especially in eastern Australia. The clear positive anomalies in 2010-2011 observed for  $\tau_a$ , LAI and  $\Theta$  are focused in central and eastern Australia. SWA is characterized by below average values, which is also visible in the time series in Fig. V.5c. This corresponds to the observations reported in [Van Dijk et al. \(2013\)](#), where SWA suffered the driest year on record until then. The strongest anomalies are found in interior Australia, which typically does not receive much rainfall and vegetation is sparse. However, with precipitation events vegetation blooms, mainly grasses, and therefore relative changes are more extreme in interior Australia. Significant differences between the annual mean of 2010 - 2011 compared to the ensemble mean are found for all three products in interior Australia (Fig. V.8).

For all three products, a clear pattern from north-west (NWA) to south-east (SEA) Australia can be seen (Fig. IV.9). This pattern coincides with cloud-bands that form over the Indian Ocean north-west of NWA and bring moisture deep land-inwards to SEA. Cloud-bands transport latent heat and moisture from tropical latitudes into higher latitudes and often trigger widespread and heavy rain over NWA and SEA [Wright \(1997\)](#). This north-west to south-east pattern, was also observed in time series of rain gauges [Nicholls \(1989\)](#). Variations in sea surface temperature over the Indian Ocean were found to be closely related to winter precipitation in a north-west to south-east band. Eastern rainfall was found to relate best to sea surface temperature variations in the Pacific Ocean. It was also found in [Ummenhofer et al. \(2009\)](#) that anomalous wet conditions were enhanced by precipitation brought by north-west cloud-bands when La Niña co-occurs with a negative Indian Ocean Dipole phase. Hence, the clear north-west to south-east pattern which we observe could be related to precipitation brought by cloud-bands as an effect of the interaction of climate modes.

In more vegetated regions,  $\tau_a$  and LAI do not vary as strongly as in interior Australia. Similar patterns were found in [Andela et al. \(2013\)](#), where in semi-arid drylands seasonality in  $\tau_p$  was strong, but the inter-annual response was limited. This was explained by seasonal abundance in water, where variation in precipitation does not affect vegetation. This is depicted in Fig. V.9, where the difference for every grid point between the yearly average of 2008, a year during the Millennium Drought, and 2010, during La Niña, is binned per percentage of Forest Cover. Here a decrease in the relative difference between the two years decreases with increasing Forest Cover. This could indicate that total water content in vegetation changes less dramatically in more forested regions, and that  $\tau_a$  is less sensitive to vegetation water content over forests than over grasslands. This can also be observed in Fig. V.8, where in the eastern parts of Australia LAI (Fig. V.8b) shows significant differences between the annual mean of 2010 - 2011 compared to the ensemble mean, but for  $\tau_a$  (Fig. V.8a) this is limited to a smaller region.

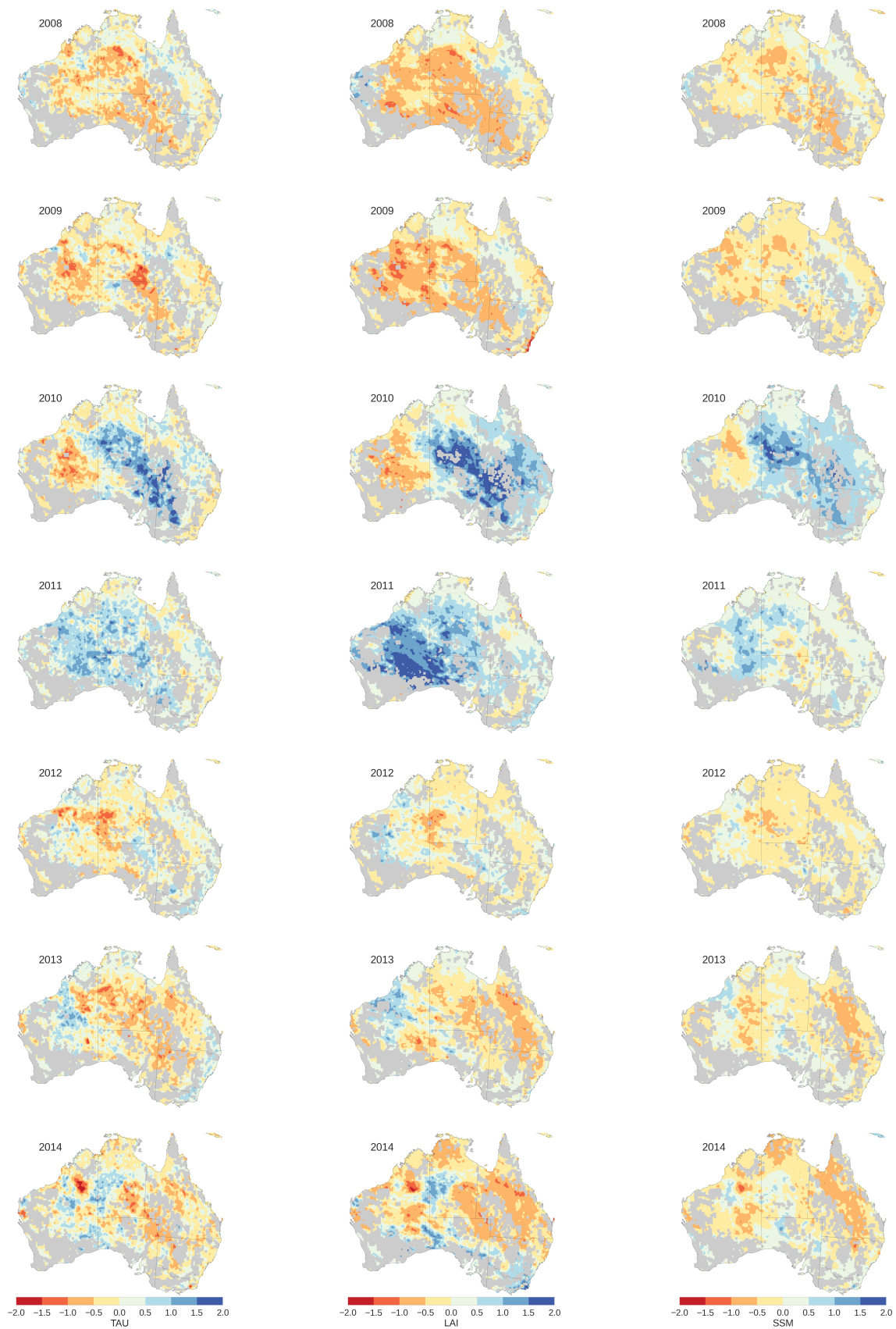


**Figure V.7:** These plots depict the yearly differences from the mean over 2008 to 2014 for  $\tau_a$  (left column), LAI (middle column) and  $\Theta$  (right column). Higher (lower) than the ensemble average values are depicted in blue (red).

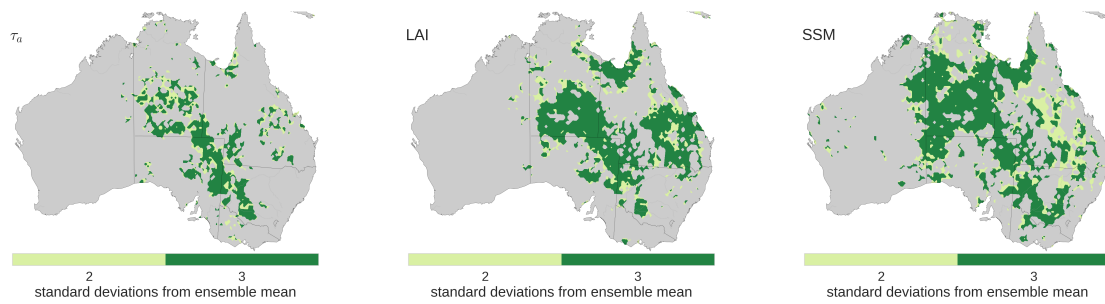


**Figure V.8:** Areas where a significant difference (three standard deviations above the ensemble mean) between the annual mean of 2010 - 2011 compared to the ensemble mean is found are indicated in green. Areas that are two standard deviations above the ensemble mean are depicted in yellow. Plots show: a.  $\tau_a$ , b. LAI, c.  $\Theta$ .

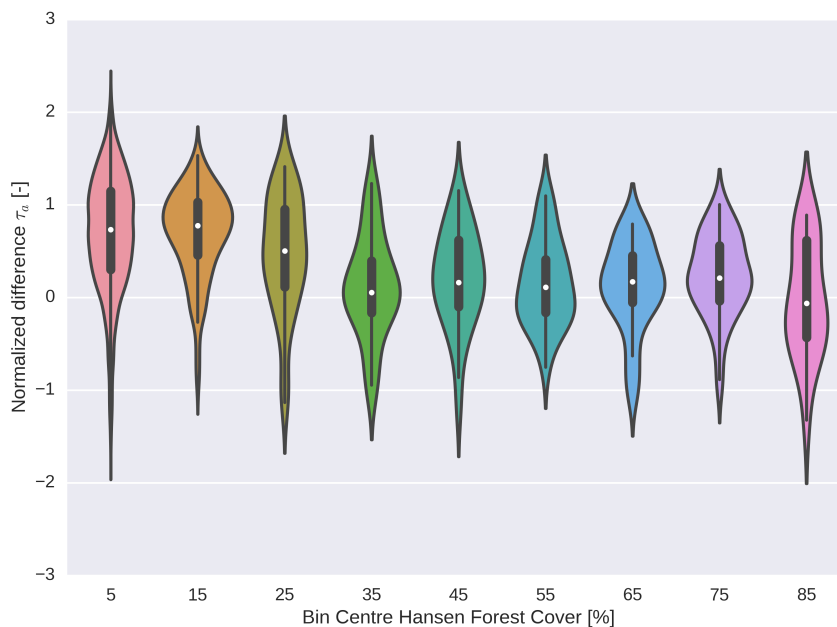


**Figure V.9:** Difference between normalized  $\tau_a$  between the year 2008 and 2010 (2010–2008) per gridpoint, binned to their respective percentage forest cover.

## 5 Conclusions

This study assessed the ability of  $\tau_a$  derived from ASCAT-A to capture inter-annual variability in vegetation dynamics. An improved estimation of model parameters in the TU Wien soil moisture algorithm allows for the retrieval of time series of  $\tau_a$ . We demonstrate that  $\tau_a$  derived from ASCAT-A is related to vegetation dynamics, as observed in LAI. In forested regions negative correlations between  $\tau_a$  and LAI are observed, which are attributed to scattering mechanisms which are not accounted for in the current  $\tau_a$  retrieval algorithm. Furthermore, dynamics of  $\tau_a$  show distinct inter-annual variability as observed in LAI and  $\Theta$ . For  $\tau_a$ , but also LAI and  $\Theta$ , positive anomalies are observed in an area which extends from north-west to south-east Australia. This area is possibly related to north-west cloud-bands that form over the Indian Ocean bringing precipitation land-inward to south-east Australia. Due to its sensitivity to the woody part of the vegetation,  $\tau_a$  shows a less pronounced increase in the north-east and east part of Australia.

This study confirms that variations in  $\tau_a$  are related to vegetation dynamics. It demonstrates the added value of scatterometers to monitor land surface parameters. However, the problems that were encountered in forested regions show that further studies on backscatter mechanisms and how to account for them in scattering models is needed. The successive scatterometers on-board ERS-1, Metop-A, Metop-B, and in the future Metop-C and Metop-SG SCA, provide a long-term dataset which presents an opportunity to further study trends and inter-annual variability in vegetation and scattering mechanisms related to vegetation.

## Acknowledgments

The authors would like to acknowledge financial support from the Austrian Science Funds FWF as part of the Doctoral Programme on Water Resource Systems (DK-plus W1219-N22) and the Satellite Application Facility on support to operational hydrology and water management (H-SAF). Wouter Dorigo is supported by the personal grant TU Wien Wissenschaftspreis 2015.

The SPOT-VGT LAI dataset was generated by the land service of Copernicus, the Earth Observation programme of the European Commission. The research leading to the current version of the product has received funding from various European Commission Research and Technical Development programmes. The product is based on SPOT/VGT 1km data ((c) CNES and distributed by VITO). We would also like to thank the ESA Climate Change Initiative Land Cover project (2014) for providing Land Cover data.

# **Chapter VI**

## **Conclusions and Outlook**



## 1 General

One of the biggest challenges of our generation is to preserve Earth's land surface and ecosystems. Humanity's impact on the Earth, by way of nuclear bomb tests, pollution, exploitation of resources and deforestation, is now so profound that scientists call for the declaration of a new geological epoch: The Anthropocene. This underpins the importance of monitoring Earth's ecosystems for investigating the effects of climate change and human impact. Designed to monitor ocean winds, observations from scatterometers have become a valuable source of information for monitoring land surface parameters. The advantage of scatterometers are their ability to observe Earth under cloud conditions, independence of solar illumination, and the higher spatial resolution, radiometric accuracy and stability compared to passive microwave observations. A series of European scatterometers on-board ERS-1, Metop-A and Metop-B provide long-term observations which are needed to observe trends and variability in land surface parameters.

The primary objective of this study was to develop and assess a methodology to retrieve vegetation optical depth from active microwave observations. To our knowledge, this is the first global  $\tau$  product based on active microwave observations. The approach was to use model parameters from an existing soil moisture retrieval algorithm, the TU Wien backscatter model, and a simple water-cloud model. With this approach two unknowns remained, vegetation optical depth and sensitivity of bare soil surface scattering. Vegetation optical depth is estimated as the decrease in sensitivity to soil moisture as observed in model parameters from the TU Wien backscatter model. It was decided to set bare soil surface scattering to a constant value, except in deserts where no vegetation is present and the bare soil surface scattering is based on the lowest observed backscatter. The method proved to be successful and was able to produce  $\tau_a$  which satisfactorily followed spatial and temporal vegetation patterns as observed in reference datasets. Especially in croplands and grasslands and in temperate and cold climates strong temporal correspondence was found between  $\tau_a$  and the reference datasets. Phenological parameters were calculated from  $\tau_a$  which were comparable to parameters calculated from the reference datasets. In addition, inter-annual variability in vegetation was observed in time series of  $\tau_a$ , demonstrating the potential of  $\tau_a$  to detect trends and anomalies in vegetation. This study demonstrated the potential of  $\tau_a$ , and active microwave observations, to monitor vegetation.

## 2 Scientific implications

The detailed analyses of  $\tau_a$  performed in this study, have increased our understanding of active microwaves and land surface parameters both with regard to more general backscatter theory and more specific with regard to soil moisture retrieval from ASCAT.

### 2.1 Implications for backscatter modeling of vegetation

Discrepancies between  $\tau_a$  and the reference datasets over deciduous broadleaf forests, which were discussed in Chapter IV, brought to light fundamental issues in backscatter models. Strong negative correlations were found between vegetation products from active microwave observations and both VNIR and passive microwave observations. The opposite temporal behaviour of the products seemed to have a strong seasonal cycle and was subsequently related to leaf fall. It was suggested that with leaf fall the contribution of double-bounce backscatter, via the soil and the stems, increases. This suggests that the water-cloud model used to retrieve  $\tau_a$  might be too simplistic since it does not take into account an interaction-term between soil and vegetation,  $\sigma_{int}^{\circ}$ . Hence, this thesis supports revisiting the assumption that  $\sigma_{int}^{\circ}$  can be ignored.

## 2.2 Implications for vegetation monitoring

ESAs BIOMASS mission is designed to map forest biomass on a global scale, using a fully polarimetric P-band SAR. Its main objective is to improve the understanding and quantification of land contribution to the global carbon cycle by improving global estimates of above ground biomass, forest disturbances and recovery. Since vegetation consists mainly of water, and  $\tau_a$  is sensitive to the total vegetation water content, it can provide an additional active microwave based informative dataset for the BIOMASS mission. This study has also shown the challenge in interpreting the backscatter signal over deciduous broadleaf forest, providing prior information on interpreting the SAR signal over this land cover class.

## 2.3 Implications for the TU Wien soil moisture retrieval algorithm

Analysis of  $\tau_a$  over boreal forests discussed in Chapter IV, demonstrated the effect of cold conditions on backscatter and the model parameters in the TU Wien algorithm. A bias between  $\tau_a$  and the reference datasets was observed, which increases with decreasing winter air temperatures. The bias was attributed to the inclusion of low backscatter observed during cold conditions in the calculation of the TU Wien model parameters. The bias in  $\tau_a$  and the model parameters of the TU Wien retrieval algorithm propagate to the operational soil moisture product. This bias was already observed in several validation studies which compared ASCAT soil moisture retrievals to other microwave remote sensing and modeled soil moisture products. By identifying the origin of the bias in this thesis, the bias can potentially be resolved in the model parameter estimation of future versions of the TU Wien retrieval algorithm.

In Chapter III the retrieval and validation of  $\tau_a$  brought to light the effect of neglecting inter-annual variability in the vegetation correction term. Introducing an inter-annually varying vegetation correction could improve soil moisture retrievals over highly dynamic and vulnerable regions like the Sahel. It is expected that using the vegetation parameterization which provides time series of  $\sigma'_r$  and  $\sigma''_r$  as described in Chapter V will improve the soil moisture retrieval in these regions.

## 3 Future studies

Future improvements of  $\tau_a$  should focus on including an interaction term in the model to account for soil-vegetation interaction scattering. This could possibly improve  $\tau_a$  retrievals over deciduous forests. Furthermore, this study brought to light an underestimation of vegetation in boreal forests, which propagates an additive error in the soil moisture retrieval. Retrieval of soil moisture and  $\tau_a$  can be improved by revisiting the assumption that backscatter from frozen soils is similar to that of dry soils.

In this thesis the focus was primarily on retrieval and validation of  $\tau_a$  from C-band observations. But the effect of frequency on the retrieval of vegetation products has not been discussed. Since the penetration depth of microwaves depends strongly on the frequency, it is assumed that lower frequencies can penetrate vegetation deeper. For example, ESAs BIOMASS mission operates at P-band, which is expected to penetrate the vegetation deeper, especially over dense forest. Because of the difference in penetration depth, lower frequencies are likely to be sensitive to a different part of the vegetation and could provide additional information on vegetation dynamics complementary to C-band and optical datasets. However, at the scale of ASCAT, studies have not yet thoroughly investigated from which part of the vegetation the signal originates from.

## 4 Applications of $\tau_a$

Applications which can utilize the newly developed  $\tau_a$  are numerous. Time series of  $\tau_a$  can help in monitoring trends and anomalies in vegetation dynamics or phenology as a result of climate change or extreme events. For example, variability in the start of the growing season can have a large effect on the carbon storage. Some first applications were also presented in this thesis. Phenological parameters, i.e. start and peak of season were derived from  $\tau_a$  in Chapter IV. The timing of the phenological parameters showed a strong correspondence to the reference datasets and spatial patterns followed climate zones and land cover classes. Over mainland Australia the sensitivity of  $\tau_a$  to inter-annual variability was investigated and discussed in Chapter V. Clear patterns and a significantly high  $\tau_a$  in years of large amounts of rainfall demonstrated the sensitivity of  $\tau_a$  to vegetation dynamics. Especially with highly dynamic vegetation which responds quickly to rainfall, e.g. grasses,  $\tau_a$  captures inter-annual variability.

Another interesting application of the  $\tau_a$  product could be monitoring of deforestation. Recent studies have used  $\tau$  from passive microwave observations to monitor forest loss in the Amazon. The higher spatial resolution of  $\tau_a$  could possibly provide more detailed information on the spatial extent of deforestation and forest fires. Especially in tropical regions this could be of importance since VNIR observations are often hindered by cloud cover.

The sensitivity of  $\tau_a$  to inter-annual variability could potentially be used to monitor croplands.  $\tau_a$  can also be used in combination with higher resolution products. Sentinel 1 C-band backscatter is available at a spatial resolution of 5 by 20 meters and a temporal resolution of 3 to 4 days. While  $\tau_a$  can provide global estimates of the state of vegetation on a daily basis, Sentinel 1 data can be used to obtain a high resolution product. One method could be to combine  $\tau_a$  derived from ASCAT observations and CR derived from VH and VV polarized Sentinel 1 observations. As this study has shown,  $\tau_a$  and CR show temporal correspondence in croplands, which suggests they are sensitive to similar processes. By combining observations from the two sensors a high resolution product can be developed which can be used for monitoring vegetation on the field scale.



## Bibliography

- Ahlström, A., Raupach, M. R., Schurgers, G., Smith, B., Arneeth, A., Jung, M., Reichstein, M., Canadell, J. G., Friedlingstein, P., Jain, A. K., and others (2015). The dominant role of semi-arid ecosystems in the trend and variability of the land CO<sub>2</sub> sink. *Science*, 348(6237):895–899.
- Al-Yaari, A., Wigneron, J. P., Ducharne, A., Kerr, Y. H., Wagner, W., De Lannoy, G., Reichle, R., Al Bitar, A., Dorigo, W., Richaume, P., and Mialon, A. (2014). Global-scale comparison of passive (SMOS) and active (ASCAT) satellite based microwave soil moisture retrievals with soil moisture simulations (MERRA-Land). *Remote Sensing of Environment*, 152:614–626.
- Albergel, C., de Rosnay, P., Gruhier, C., Muñoz-Sabater, J., Hasenauer, S., Isaksen, L., Kerr, Y., and Wagner, W. (2012). Evaluation of remotely sensed and modelled soil moisture products using global ground-based in situ observations. *Remote Sensing of Environment*, 118(0):215–226.
- Andela, N., Liu, Y. Y., van Dijk, A. I. J. M., de Jeu, R. A. M., and McVicar, T. R. (2013). Global changes in dryland vegetation dynamics assessed by satellite remote sensing: comparing a new passive microwave vegetation density record with reflective greenness data. *Biogeosciences*, 10(10):6657–6676.
- Attema, E. P. W. and Ulaby, F. T. (1978). Vegetation modeled as a water cloud. *Radio Science*, 13(2):357–364.
- Baghdadi, N., Cerdan, O., Zribi, M., Auzet, V., Darboux, F., El Hajj, M., and Kheir, R. B. (2008). Operational performance of current synthetic aperture radar sensors in mapping soil surface characteristics in agricultural environments: application to hydrological and erosion modelling. *Hydrological Processes*, 22(1):9–20.
- Baghdadi, N., King, C., Bourguignon, A., and Remond, A. (2002). Potential of ERS and Radarsat data for surface roughness monitoring over bare agricultural fields: Application to catchments in Northern France. *International Journal of Remote Sensing*, 23(17):3427–3442.
- Balsamo, G., Albergel, C., Beljaars, A., Bousssetta, S., Cloke, H., Dee, D., Dutra, E., Muñoz Sabater, J., Pappenberger, F., de Rosnay, P., Stockdale, T., and Vitart, F. (2013). ERA-Interim/Land: a global land water resources dataset. *Hydrology and Earth System Sciences Discussions*, 10(12):14705–14745.
- Baret, F., Weiss, M., Lacaze, R., Camacho, F., Makhmara, H., Pacholczyk, P., and Smets, B. (2013). GEOV1: LAI and FAPAR essential climate variables and FCOVER global time series capitalizing over existing products. Part1: Principles of development and production. *Remote Sensing of Environment*, 137:299–309.
- Bartsch, A., Kidd, R. A., Wagner, W., and Bartalis, Z. (2007). Temporal and spatial variability of the beginning and end of daily spring freeze/thaw cycles derived from scatterometer data. *Remote Sensing of Environment*, 106(3):360–374.
- Beaudoin, A., Le Toan, T., and Gwyn, Q. (1990). SAR observations and modeling of the C-band backscatter variability due to multiscale geometry and soil moisture. *IEEE Transactions on Geoscience and Remote Sensing*, 28(5):886–895.

- Berthelot, M., Friedlingstein, P., Ciais, P., Monfray, P., Dufresne, J. L., Le Treut, H., and Fairhead, L. (2002). Global response of the terrestrial biosphere to CO<sub>2</sub> and climate change using a coupled climate-carbon cycle model. *Global Biogeochemical Cycles*, 16(4).
- Bindlish, R. and Barros, A. P. (2000). Multifrequency Soil Moisture Inversion from SAR Measurements with the Use of IEM. *Remote Sensing of Environment*, 71(1):67–88.
- Brocca, L., Ciabatta, L., Massari, C., Moramarco, T., Hahn, S., Hasenauer, S., Kidd, R., Dorigo, W., Wagner, W., and Levizzani, V. (2014). Soil as a natural rain gauge: Estimating global rainfall from satellite soil moisture data. *Journal of Geophysical Research-Atmospheres*, 119(9):5128–5141.
- Brocca, L., Hasenauer, S., Lacava, T., Melone, F., Moramarco, T., Wagner, W., Dorigo, W., Matgen, P., Martinez-Fernandez, J., Llorens, P., Latron, J., Martin, C., and Bittelli, M. (2011). Soil moisture estimation through ASCAT and AMSR-E sensors: An intercomparison and validation study accross Europe. *Remote Sensing of Environment*, page submitted.
- Camacho, F., Cernicharo, J., Lacaze, R., Baret, F., and Weiss, M. (2013). GEOV1: LAI, FAPAR essential climate variables and FCOVER global time series capitalizing over existing products. part 2: Validation and intercomparison with reference products. *Remote Sensing of Environment*, 137:310–329.
- Cramer, W., Bondeau, A., Schaphoff, S., Lucht, W., Smith, B., and Sitch, S. (2004). Tropical forests and the global carbon cycle: impacts of atmospheric carbon dioxide, climate change and rate of deforestation. *Philosophical Transactions of the Royal Society of London B: Biological Sciences*, 359(1443):331–343.
- Cui, Q., Shi, J., Du, J., Zhao, T., and Xiong, C. (2015). An Approach for Monitoring Global Vegetation Based on Multiangular Observations From SMOS. *IEEE Journal of Selected Topics in Applied Earth Observations and Remote Sensing*, 8(2):604–616.
- Davidson, M., Toan, T. L., Mattia, F., Satalino, G., Manninen, T., and Borgeaud, M. (2000). On the characterization of agricultural soil roughness for radar remote sensing studies. *IEEE Transactions on Geoscience and Remote Sensing*, 38(2):630–640.
- De Matthaeis, P., Schiavon, G., and Solimini, D. (1994). Effect of scattering mechanisms on polarimetric features of crops and trees. *International Journal of Remote Sensing*, 15(14):2917–2930.
- de Rosnay, P., Drusch, M., Vasiljevic, D., Balsamo, G., Albergel, C., and Isaksen, L. (2013). A simplified Extended Kalman Filter for the global operational soil moisture analysis at ECMWF. *Quarterly Journal of the Royal Meteorological Society*, 139(674):1199–1213.
- Dee, D. P., Uppala, S. M., Simmons, A. J., Berrisford, P., Poli, P., Kobayashi, S., Andrae, U., Balmaseda, M. A., Balsamo, G., Bauer, P., Bechtold, P., Beljaars, A. C. M., van de Berg, L., Bidlot, J., Bormann, N., Delsol, C., Dragani, R., Fuentes, M., Geer, A. J., Haimberger, L., Healy, S. B., Hersbach, H., Hólm, E. V., Isaksen, L., Kållberg, P., Köhler, M., Matricardi, M., McNally, A. P., Monge-Sanz, B. M., Morcrette, J.-J., Park, B.-K., Peubey, C., de Rosnay, P., Tavolato, C., Thépaut, J.-N., and Vitart, F. (2011). The ERA-Interim reanalysis: configuration and performance of the data assimilation system. *Quarterly Journal of the Royal Meteorological Society*, 137(656):553–597.
- Dobson, M. C., McDonald, K., Ulaby, F. T., and Way, J. (1990). Effects of temperature on radar backscatter from boreal forests. In *Geoscience and Remote Sensing Symposium, 1990. IGARSS'90. Remote Sensing Science for the Nineties'*, 10th Annual International, pages 2481–2484. IEEE.
- Dobson, M. C. and Ulaby, F. T. (1986a). Active microwave soil moisture research. *IEEE Transactions on Geoscience and Remote Sensing*, GE-24(1):23–36.
- Dobson, M. C. and Ulaby, F. T. (1986b). Preliminary Evaluation of the SIR-B Response to Soil Moisture, Surface Roughness, and Crop Canopy Cover. *IEEE Transactions on Geoscience and Remote Sensing*, GE-24(4):517–526.

- Dorigo, W., de Jeu, R., Chung, D., Parinussa, R., Liu, Y., Wagner, W., and Fernández-Prieto, D. (2012). Evaluating global trends (1988–2010) in harmonized multi-satellite surface soil moisture. *Geophysical Research Letters*, 39(18):n/a–n/a. L18405.
- Dorigo, W. A., Gruber, A., De Jeu, R. A. M., Wagner, W., Stacke, T., Loew, A., Albergel, C., Brocca, L., Chung, D., Parinussa, R. M., and others (2015). Evaluation of the ESA CCI soil moisture product using ground-based observations. *Remote Sensing of Environment*, 162:380–395.
- Doubkova, M., Naeimi, V., Wagner, W., and Henebry, G. (2009). On the ability of the ERS scatterometer to detect vegetation properties. In *Geoscience and Remote Sensing Symposium, 2009 IEEE International, IGARSS 2009*, volume 3, pages III–920–III–923.
- Draper, C. S., Walker, J. P., Steinle, P. J., de Jeu, R. A., and Holmes, T. R. (2009). An evaluation of AMSR–E derived soil moisture over Australia. *Remote Sensing of Environment*, 113(4):703–710.
- FAO/IIASA/ISRIC/ISSCAS/JRC (2012). Harmonized world soil database (version 1.2). FAO, Rome, Italy and IIASA, Laxenburg, Austria.
- Ferrazzoli, P., Paloscia, S., Pampaloni, P., Schiavon, G., Sigismondi, S., and Solimini, D. (1997). The potential of multifrequency polarimetric SAR in assessing agricultural and arboreal biomass. *IEEE Transactions on Geoscience and Remote Sensing*, 35(1):5–17.
- Ferrazzoli, P., Paloscia, S., Pampaloni, P., Schiavon, G., Solimini, D., and Coppo, P. (1992). Sensitivity of microwave measurements to vegetation biomass and soil moisture content: a case study. *IEEE Transactions on Geoscience and Remote Sensing*, 30(4):750–756.
- Foley, J. A., DeFries, R., Asner, G. P., Barford, C., Bonan, G., Carpenter, S. R., Chapin, F. S., Coe, M. T., Daily, G. C., Gibbs, H. K., and others (2005). Global consequences of land use. *science*, 309(5734):570–574.
- Frison, P., Mougin, E., and Hiernaux, P. (1998). Observations and interpretation of seasonal ers-1 wind scatterometer data over northern sahel (mali). *Remote Sensing of Environment*, 63(3):233 – 242.
- Frison, P. L. and Mougin, E. (1996). Monitoring global vegetation dynamics with ers-1 wind scatterometer data. *International Journal of Remote Sensing*, 17(16):3201–3218.
- Frolking, S., Milliman, T., McDonald, K., Kimball, J., Zhao, M., and Fahnestock, M. (2006). Evaluation of the SeaWinds scatterometer for regional monitoring of vegetation phenology. *Journal of Geophysical Research: Atmospheres*, 111(D17):n/a–n/a.
- Fung, A., Liu, W., Chen, K., and Tsay, M. (2002). An improved IEM model for bistatic scattering from rough surfaces. *Journal of Electromagnetic Waves and Applications*, 16(5):689–702.
- Gouweleeuw, B. T., van Dijk, A. I. J. M., Guerschman, J. P., Dyce, P., and Owe, M. (2012). Space-based passive microwave soil moisture retrievals and the correction for a dynamic open water fraction. *Hydrology and Earth System Sciences*, 16(6):1635–1645.
- Guan, K. (2013). *Hydrological variability on vegetation seasonality, productivity and composition in tropical ecosystems of Africa*. Princeton, NJ : Princeton University.
- Guan, K., Wood, E. F., Medvigy, D., Kimball, J., Pan, M., Caylor, K. K., Sheffield, J., Xu, X., and Jones, M. O. (2014). Terrestrial hydrological controls on land surface phenology of african savannas and woodlands. *Journal of Geophysical Research: Biogeosciences*, 119(8):1652–1669.
- Hahn, S., Reimer, C., Vreugdenhil, M., Melzer, T., and Wagner, W. (2016). Dynamic characterization of the incidence angle dependency of backscatter using metop ascats. *IEEE JSTARS Scatterometer Special Issue*.
- Hallikainen, M., Ulaby, F. T., Dobson, M. C., and El-Rayes, M. (1984a). Dielectric measurements of soils in the 3 to 37 GHz band between -50 c and 23 c. In *ESA IGARSS 84. Remote Sensing: From Res. Towards Operational Use*, volume 1.

- Hallikainen, M., Ulaby, F. T., Dobson, M. C., and El-Rayes, M. (1984b). Dielectric measurements of soils in the 3 to 37 GHz band between -50 °C and 23 °C. In *ESA IGARSS 84. Remote Sensing: From Res. Towards Operational Use*, volume 1.
- Hansen, M. C., Potapov, P. V., Moore, R., Hancher, M., Turubanova, S. A., Tyukavina, A., Thau, D., Stehman, S. V., Goetz, S. J., Loveland, T. R., Kommareddy, A., Egorov, A., Chini, L., Justice, C. O., and Townshend, J. R. G. (2013). High-resolution global maps of 21st-century forest cover change. *Science*, 342(6160):850–853.
- Hendon, H. H., Lim, E.-P., Arblaster, J. M., and Anderson, D. L. (2014). Causes and predictability of the record wet east Australian spring 2010. *Climate dynamics*, 42(5-6):1155–1174.
- Hirschi, M., Mueller, B., Dorigo, W., and Seneviratne, S. (2014). Using remotely sensed soil moisture for land–atmosphere coupling diagnostics: The role of surface vs. root-zone soil moisture variability. *Remote Sensing of Environment*, 154(0):246 – 252.
- Holmes, T. R. H., De Jeu, R. A. M., Owe, M., and Dolman, A. J. (2009). Land surface temperature from ka band (37 ghz) passive microwave observations. *Journal of Geophysical Research: Atmospheres*, 114(D4):n/a–n/a. D04113.
- Hong, S. H. and Wdowinski, S. (2014). Double-bounce component in cross-polarimetric SAR from a new scattering target decomposition. *IEEE Transactions on Geoscience and Remote Sensing*, 52(6):3039–3051.
- Jackson, T., McNairn, H., Weltz, M., Brisco, B., and Brown, R. (1997). First order surface roughness correction of active microwave observations for estimating soil moisture. *IEEE Transactions on Geoscience and Remote Sensing*, 35(4):1065–1069.
- Jackson, T. J., Schmugge, T. J., and Wang, J. R. (1982). Passive microwave sensing of soil moisture under vegetation canopies. *Water Resources Research*, 18(4):1137–1142.
- Jarlan, L., Mougou, E., Frison, P. L., Mazzega, P., and Hiernaux, P. (2002). Analysis of ERS wind scatterometer time series over sahel (mali). *Remote Sensing of Environment*, 81(2):404–415.
- Jones, L. A., Kimball, J. S., Podest, E., McDonald, K. C., Chan, S. K., and Njoku, E. G. (2009). A method for deriving land surface moisture, vegetation optical depth, and open water fraction from AMSR-E. In *2009 IEEE International Geoscience and Remote Sensing Symposium*, volume 3, pages III–916. IEEE.
- Jones, M. O., Jones, L. A., Kimball, J. S., and McDonald, K. C. (2011). Satellite passive microwave remote sensing for monitoring global land surface phenology. *Remote Sensing of Environment*, 115(4):1102 – 1114.
- Jones, M. O., Kimball, J. S., and Jones, L. A. (2013). Satellite microwave detection of boreal forest recovery from the extreme 2004 wildfires in Alaska and Canada. *Global Change Biology*, 19(10):3111–3122.
- Jones, M. O., Kimball, J. S., Jones, L. A., and McDonald, K. C. (2012). Satellite passive microwave detection of North America start of season. *Remote Sensing of Environment*, 123:324–333.
- Kerr, Y., Waldteufel, P., Richaume, P., Wigneron, J.-P., Ferrazzoli, P., Mahmoodi, A., Al Bitar, A., Cabot, F., Gruhier, C., Juglea, S., Leroux, D., Mialon, A., and Delwart, S. (2012). The SMOS soil moisture retrieval algorithm. *Geoscience and Remote Sensing, IEEE Transactions on*, 50(5):1384–1403.
- Kim, S.-B., Moghaddam, M., Tsang, L., Burgin, M., Xu, X., and Njoku, E. (2014). Models of L-band radar backscattering coefficients over global terrain for soil moisture retrieval. *Geoscience and Remote Sensing, IEEE Transactions on*, 52(2):1381–1396.
- Kim, S.-B., Tsang, L., Johnson, J., Huang, S., van Zyl, J., and Njoku, E. (2012a). Soil moisture retrieval using time-series radar observations over bare surfaces. *Geoscience and Remote Sensing, IEEE Transactions on*, 50(5):1853–1863.

- Kim, Y., Jackson, T., Bindlish, R., Lee, H., and Hong, S. (2012b). Radar vegetation index for estimating the vegetation water content of rice and soybean. *IEEE Geoscience and Remote Sensing Letters*, 9(4):564–568.
- Kirdiashev, K. P., Chukhlantsev, A. A., and Shutko, A. M. (1979). Microwave radiation of the earth's surface in the presence of vegetation cover. *Radiotekhnika I Elektronika*, 24:256–264.
- Kottek, M., Grieser, J., Beck, C., Rudolf, B., and Rubel, F. (2006). World Map of the Koeppen-Geiger climate classification updated. *Meteorologische Zeitschrift*, 15:259–263.
- Kuenzer, C., Schmidt, M., and Wagner, W. (2008). Trend analyses of a global soil moisture time series derived from ERS-1/-2 scatterometer data: floods, droughts and long term changes. *Int. Arch. Photogramm., Remote Sens. Spat. Inf. Sci.*, 37.
- Lievens, H., Vernieuwe, H., Álvarez Mozos, J., De Baets, B., and Verhoest, N. E. C. (2009). Error in Radar-Derived Soil Moisture due to Roughness Parameterization: An Analysis Based on Synthetic Surface Profiles. *Sensors*, 9(2):1067–1093.
- Linderholm, H. W. (2006). Growing season changes in the last century. *Agricultural and Forest Meteorology*, 137(1&2):1–14.
- Liu, Y. Y., de Jeu, R. A. M., McCabe, M. F., Evans, J. P., and van Dijk, A. I. J. M. (2011). Global long-term passive microwave satellite-based retrievals of vegetation optical depth. *Geophysical Research Letters*, 38(18):n/a–n/a.
- Liu, Y. Y., van Dijk, A. I. J. M., McCabe, M. F., Evans, J. P., and de Jeu, R. A. M. (2013). Global vegetation biomass change (1988–2008) and attribution to environmental and human drivers. *Global Ecology and Biogeography*, 22(6):692–705.
- Macelloni, G., Paloscia, S., Pampaloni, P., Marliani, F., and Gai, M. (2001). The relationship between the backscattering coefficient and the biomass of narrow and broad leaf crops. *Geoscience and Remote Sensing, IEEE Transactions on*, 39(4):873–884.
- Magagi, R. and Kerr, Y. (1997). Retrieval of soil moisture and vegetation characteristics by use of ERS-1 wind scatterometer over arid and semi-arid areas. *Journal of Hydrology*, 188–189(0):361 – 384. HAPEX-Sahel.
- Matzler, C. (1998). Microwave permittivity of dry sand. *Geoscience and Remote Sensing, IEEE Transactions on*, 36(1):317–319.
- McColl, K. A., Entekhabi, D., and Piles, M. (2014). Uncertainty analysis of soil moisture and vegetation indices using Aquarius scatterometer observations. *Geoscience and Remote Sensing, IEEE Transactions on*, 52(7):4259–4272.
- McDonald, K., Zimmermann, R., and Kimball, J. (2002). Diurnal and spatial variation of xylem dielectric constant in Norway Spruce (*Picea abies* [L.] Karst.) as related to microclimate, xylem sap flow, and xylem chemistry. *IEEE Transactions on Geoscience and Remote Sensing*, 40(9):2063–2082.
- McNairn, H. and Brisco, B. (2004). The application of c-band polarimetric SAR for agriculture: a review. *Canadian Journal of Remote Sensing*, 30(3):525–542.
- McNairn, H., Hochheim, K., and Rabe, N. (2004). Applying polarimetric radar imagery for mapping the productivity of wheat crops. *Canadian Journal of Remote Sensing*, 30(3):517–524.
- McNairn, H., Van der Sanden, J. J., Brown, R. J., and Ellis, J. (2000). The potential of RADARSAT-2 for crop mapping and assessing crop condition. In *Second International Conference on Geospatial Information in Agriculture and Forestry, Lake Buena Vista, FL*.
- Meesters, A., de Jeu, R., and Owe, M. (2005). Analytical derivation of the vegetation optical depth from the microwave polarization difference index. *Geoscience and Remote Sensing Letters, IEEE*, 2(2):121–123.

- Melzer, T. (2013). Vegetation Modelling in WARP 6.0. In *Proceedings*, Vienna, Austria. EUMETSAT.
- Miralles, D., van den Berg, M., Gash, J., Parinussa, R., De Jeu, R., Beck, H., Holmes, T., Jimenez, C., Verhoest, N., Dorigo, W., Teuling, A. J., and Dolman, H. (2014). El niño-la niña cycle and recent trends in continental evaporation. *Nature Climate Change*, 4(2):122–126.
- Mo, T., Choudhury, B. J., Schmugge, T. J., Wang, J. R., and Jackson, T. J. (1982). A model for microwave emission from vegetation-covered fields. *Journal of Geophysical Research: Oceans*, 87(C13):11229–11237.
- Moran, M. S., Hymer, D. C., Qi, J., and Kerr, Y. (2002). Comparison of ERS-2 SAR and Landsat TM imagery for monitoring agricultural crop and soil conditions. *Remote Sensing of Environment*, 79(2–3):243–252.
- Moulin, S., Kergoat, L., Viovy, N., and Dedieu, G. (1997). Global-scale assessment of vegetation phenology using NOAA/AVHRR satellite measurements. *Journal of Climate*, 10(6):1154–1170.
- Naeimi, V., Scipal, K., Bartalis, Z., Hasenauer, S., and Wagner, W. (2009). An improved soil moisture retrieval algorithm for ers and metop scatterometer observations. *IEEE Transaction on Geoscience and Remote Sensing*, 47(7):1999–2013.
- Nicholls, N. (1989). Sea surface temperatures and Australian winter rainfall. *Journal of Climate*, 2(9):965–973.
- Nichols, G. (2009). *Sedimentology and stratigraphy - second edition*. Wiley-Blackwell.
- Nijs, A. H. A. d., Parinussa, R. M., Jeu, R. A. M. d., Schellekens, J., and Holmes, T. R. H. (2015). A methodology to determine radio-frequency interference in AMSR2 observations. *IEEE Transactions on Geoscience and Remote Sensing*, 53(9):5148–5159.
- Oh, Y., Sarabandi, K., and Ulaby, F. (1992). An empirical model and an inversion technique for radar scattering from bare soil surfaces. *IEEE Transactions on Geoscience and Remote Sensing*, 30(2):370–381.
- Owe, M., de jeu, R., and Holmes, T. (2008). Multisensor historical climatology of satellite-derived global land surface moisture. *Journal of Geophysical Research-Earth Surface*, 113(F1):F01002.
- Owe, M., de Jeu, R., and Walker, J. (2001). A methodology for surface soil moisture and vegetation optical depth retrieval using the microwave polarization difference index. *Geoscience and Remote Sensing, IEEE Transactions on*, 39(8):1643–1654.
- Paloscia, S., Macelloni, G., and Pampaloni, P. (1998). The relations between backscattering coefficient and biomass of narrow and wide leaf crops. In *Geoscience and Remote Sensing Symposium Proceedings, 1998. IGARSS '98. 1998 IEEE International*, volume 1, pages 100–102 vol.1.
- Paloscia, S., Macelloni, G., Pampaloni, P., and Sigismondi, S. (1999). The potential of C- and L-band SAR in estimating vegetation biomass: the ERS-1 and JERS-1 experiments. *IEEE Transactions on Geoscience and Remote Sensing*, 37(4):2107–2110.
- Paloscia, S., Pettinato, S., Santi, E., Notarnicola, C., Pasolli, L., and Reppucci, A. (2013). Soil moisture mapping using Sentinel-1 images: Algorithm and preliminary validation. *Remote Sensing of Environment*, 134:234–248.
- Parinussa, R. M., Holmes, T. R. H., Wanders, N., Dorigo, W. A., and de Jeu, R. A. M. (2014). A Preliminary Study toward Consistent Soil Moisture from AMSR2. *Journal of Hydrometeorology*, 16(2):932–947.
- Pasolli, L., Notarnicola, C., Bruzzone, L., Bertoldi, G., Della Chiesa, S., Hell, V., Niedrist, G., Tappeiner, U., Zebisch, M., Del Frate, F., and Vaglio Laurin, G. (2011). Estimation of Soil Moisture in an Alpine Catchment with RADARSAT2 Images. *Applied and Environmental Soil Science*, 2011:e175473.

- Paulik, C., Dorigo, W., Wagner, W., and Kidd, R. (2014). Validation of the ASCAT Soil Water Index using in situ data from the International Soil Moisture Network. *International journal of applied earth observation and geoinformation*, 30:1–8.
- Peischl, S., Walker, J. P., Rüdiger, C., Ye, N., Kerr, Y. H., Kim, E., Bandara, R., and Allahmoradi, M. (2012). The aaces field experiments: Smos calibration and validation across the murrumbidgee river catchment. *Hydrology and Earth System Sciences*, 16(6):1697–1708.
- Piles, M., McColl, K., Entekhabi, D., Das, N., and Pablos, M. (2015). Sensitivity of aquarius active and passive measurements temporal covariability to land surface characteristics. *IEEE Transactions on Geoscience and Remote Sensing*, PP(99):1–12.
- Prigent, C., Aires, F., Rossow, W., and Matthews, E. (2001). Joint characterization of vegetation by satellite observations from visible to microwave wavelengths: A sensitivity analysis. *Journal of Geophysical Research: Atmospheres*, 106(D18):20665–20685.
- Puckridge, J. T., Sheldon, F., Walker, K. F., and Boulton, A. J. (1998). Flow variability and the ecology of large rivers. *Marine and freshwater research*, 49(1):55–72.
- Pulliaainen, J., Heiska, K., Hyyppä, J., and Hallikainen, M. (1994). Backscattering properties of boreal forests at the C- and X-bands. *Geoscience and Remote Sensing, IEEE Transactions on*, 32(5):1041–1050.
- Pulliaainen, J., Mikhela, P., Hallikainen, M., and Ikonen, J.-P. (1996). Seasonal dynamics of C-band backscatter of boreal forests with applications to biomass and soil moisture estimation. *Geoscience and Remote Sensing, IEEE Transactions on*, 34(3):758–770.
- Pulliaainen, J. T., Manninen, T., and Hallikainen, M. T. (1998). Application of ERS-1 wind scatterometer data to soil frost and soil moisture monitoring in boreal forest zone. *IEEE Transactions on Geoscience and Remote Sensing*, 36(3):849–863.
- Ranson, K. J., Saatchi, S., and Sun, G. (1995). Boreal forest ecosystem characterization with SIR-C/XSAR. *Geoscience and Remote Sensing, IEEE Transactions on*, 33(4):867–876.
- Raymaekers, D., Garcia, A., Bella, C. D., Beget, M. E., Llavallol, C., Oricchio, P., Straschnoy, J., Weiss, M., and Baret, F. (2014). SPOT-VEGETATION GEOV1 biophysical parameters in semi-arid agro-ecosystems. *International Journal of Remote Sensing*, 35(7):2534–2547.
- Richardson, A. D., Keenan, T. F., Migliavacca, M., Ryu, Y., Sonnentag, O., and Toomey, M. (2013). Climate change, phenology, and phenological control of vegetation feedbacks to the climate system. *Agricultural and Forest Meteorology*, 169:156–173.
- Rodell, M., Houser, P. R., Jambor, U., Gottschalck, J., Mitchell, K., Meng, C. J., Arsenault, K., Cosgrove, B., Radakovich, J., Bosilovich, M., Entin, J. K., Walker, J. P., Lohmann, D., and Toll, D. (2004). The Global Land Data Assimilation System. *Bulletin of the American Meteorological Society*, 85(3):381–394.
- Rüdiger, C., Calvet, J.-C., Gruhier, C., Holmes, T. R., De Jeu, R. A., and Wagner, W. (2009). An intercomparison of ERS-Scat and AMSR-E soil moisture observations with model simulations over France. *Journal of Hydrometeorology*, 10(2):431–447.
- Sano, E., Moran, M., Huete, A., and Miura, T. (1998a). C- and multiangle ku-band synthetic aperture radar data for bare soil moisture estimation in agricultural areas. *Remote Sensing of Environment*, 64(1):77 – 90.
- Sano, E. E., Huete, A. R., Troufleau, D., Moran, M. S., and Vidal, A. (1998b). Relation between ERS-1 synthetic aperture radar data and measurements of surface roughness and moisture content of rocky soils in a semiarid rangeland. *Water Resources Research*, 34(6):1491–1498.
- Santi, E., Pettinato, S., Paloscia, S., Pampaloni, P., Macelloni, G., and Brogioni, M. (2012). An algorithm for generating soil moisture and snow depth maps from microwave spaceborne radiometers: HydroAlgo. *Hydrol. Earth Syst. Sci.*, 16(10):3659–3676.

- Schneider, U., Becker, A., Finger, P., Meyer-Christoffer, A., Ziese, M., and Rudolf, B. (2013). GPCP's new land surface precipitation climatology based on quality-controlled in situ data and its role in quantifying the global water cycle. *Theoretical and Applied Climatology*, 115(1-2):15–40.
- Scipal, K., Scheffler, C., and Wagner, W. (2005). Soil moisture-runoff relation at the catchment scale as observed with coarse resolution microwave remote sensing. *Hydrol. Earth Syst. Sci.*, 9(3):173–183.
- Skinner, B., Porter, S., and J., P. (2004). *Dynamic earth - an introduction to physical geology*. J. Wiley & Sons, Inc.
- Su, C.-H., Ryu, D., Young, R. I., Western, A. W., and Wagner, W. (2013). Inter-comparison of microwave satellite soil moisture retrievals over the Murrumbidgee Basin, southeast Australia. *Remote Sensing of Environment*, 134(0):1–11.
- Taylor, C. M., De Jeu, R., Guichard, F., Harris, P. P., and Dorigo, W. (2012). Afternoon rain more likely over drier soils. *Nature*, 489:282–286.
- Tian, F., Brandt, M., Liu, Y. Y., Verger, A., Tagesson, T., Diouf, A. A., Rasmussen, K., Mbow, C., Wang, Y., and Fensholt, R. (2016). Remote sensing of vegetation dynamics in drylands: Evaluating vegetation optical depth (VOD) using AVHRR NDVI and in situ green biomass data over west african sahel. *Remote Sensing of Environment*, 177:265–276.
- Toan, T. L., Beaudoin, A., Riom, J., and Guyon, D. (1992a). Relating forest biomass to SAR data. *IEEE Transactions on Geoscience and Remote Sensing*, 30(2):403–411.
- Toan, T. L., Beaudoin, A., Riom, J., and Guyon, D. (1992b). Relating forest biomass to SAR data. *IEEE Transactions on Geoscience and Remote Sensing*, 30(2):403–411.
- Ulaby, F., Allen, C., Eger, G., and Kanemasu, E. (1984). Relating the microwave backscattering coefficient to Leaf Area Index. *Remote Sensing of Environment*, 14:113–133.
- Ulaby, F. and Batlivala, P. (1976). Optimum radar parameters for mapping soil moisture. *Geoscience Electronics, IEEE Transactions on*, 14(2):81–93.
- Ulaby, F., Batlivala, P., and Dobson, M. (1978). Microwave backscatter dependence on surface roughness, soil moisture, and soil texture: Part i-bare soil. *Geoscience Electronics, IEEE Transactions on*, 16(4):286–295.
- Ulaby, F., Bradley, G., and Dobson, M. (1979). Microwave backscatter dependence on surface roughness, soil moisture, and soil texture: Part ii-vegetation-covered soil. *Geoscience Electronics, IEEE Transactions on*, 17(2):33–40.
- Ulaby, F. T. and El-Rayes, M. (1986). Microwave dielectric spectrum of vegetation material. In *International geoscience and remote sensing symposium*, pages 1103–1106.
- Ulaby, F. T., Moore, R. K., and Fung, A. K. (1982). *Microwave Remote Sensing Active and Passive- Volume II: Radar Remote Sensing and Surface Scattering and Emission Theory*. ARTECH HOUSE.
- Ulaby, F. T., Moore, R. K., and Fung, A. K. (1986). *Microwave remote sensing active and passive-volume III: from theory to applications*. ARTECH HOUSE.
- Ulaby, F. T., Sarabandi, K., McDonald, K., Whitt, M., and Dobson, M. C. (1990). Michigan microwave canopy scattering model. *International Journal of Remote Sensing*, 11(7):1223–1253.
- Ummerhofer, C. C., England, M. H., McIntosh, P. C., Meyers, G. A., Pook, M. J., Risbey, J. S., Gupta, A. S., and Taschetto, A. S. (2009). What causes southeast Australia's worst droughts? *Geophysical Research Letters*, 36(4):n/a–n/a.
- van der Schalie, R., Parinussa, R. M., Renzullo, L. J., van Dijk, A. I. J. M., Su, C. H., and de Jeu, R. A. M. (2015). SMOS soil moisture retrievals using the land parameter retrieval model: Evaluation over the Murrumbidgee Catchment, southeast Australia. *Remote Sensing of Environment*, 163:70–79.

- van Dijk, A. I. J. M., Beck, H. E., Crosbie, R. S., de Jeu, R. A. M., Liu, Y. Y., Podger, G. M., Timbal, B., and Viney, N. R. (2013). The Millennium Drought in southeast Australia (2001–2009): Natural and human causes and implications for water resources, ecosystems, economy, and society. *Water Resources Research*, 49(2):1040–1057.
- van Marle, M. J. E., van der Werf, G. R., de Jeu, R. A. M., and Liu, Y. Y. (2016). Annual South American forest loss estimates based on passive microwave remote sensing (1990–2010). *Biogeosciences*, 13(2):609–624.
- Verhoest, N. E. C., Lievens, H., Wagner, W., Alvarez-Mozos, J., Moran, M. S., and Mattia, F. (2008). On the Soil Roughness Parameterization Problem in Soil Moisture Retrieval of Bare Surfaces from Synthetic Aperture Radar. *Sensors*, 8(7):4213–4248.
- Viglione, A., Parajka, J., Rogger, M., Salinas, J. L., Laaha, G., Sivapalan, M., and Blöschl, G. (2013). Comparative assessment of predictions in ungauged basins—Part 3: Runoff signatures in Austria. *Hydrology and Earth System Sciences*, 17(6):2263–2279.
- Vine, D. M. L., Lagerloef, G. S. E., Colomb, F. R., Yueh, S. H., and Pellerano, F. A. (2007). Aquarius: An Instrument to Monitor Sea Surface Salinity From Space. *IEEE Transactions on Geoscience and Remote Sensing*, 45(7):2040–2050.
- Vreugdenhil, M., Dorigo, W. A., Wagner, W., Jeu, R. A. M. d., Hahn, S., and Marle, M. J. E. v. (2016a). Analyzing the Vegetation Parameterization in the TU-Wien ASCAT Soil Moisture Retrieval. *IEEE Transactions on Geoscience and Remote Sensing*, 54(6):3513–3531.
- Vreugdenhil, M., Hahn, S., Reimer, C., Melzer, T., Dorigo, W., Quast, R., de Jeu, R., van der Schalie, R., Notarnicola, C., Greifeneder, F., Paloscia, S., Santi, E., and Wagner, W. (2016b). Inter-comparison of vegetation variables derived from scatterometers. *IEEE JSTARS*, 104(2):155–170.
- Wagner, W. (1998). Vegetation as observed with AVHRR and ERS scatterometer- The Iberian Peninsula. *EUROPEAN SPACE AGENCY-PUBLICATIONS-ESA SP*, 424:51–56.
- Wagner, W., Brocca, L., Naeimi, V., Reichle, R., Draper, C., de Jeu, R., Ryu, D., Su, C.-H., Western, A., Calvet, J.-C., Kerr, Y., Leroux, D., Drusch, M., Jackson, T., Hahn, S., Dorigo, W., and Paulik, C. (2014). Clarifications on the comparison between smos, vva, ascat, and ecmwf soil moisture products over four watersheds in u.s. *Geoscience and Remote Sensing, IEEE Transactions on*, 52(3):1901–1906.
- Wagner, W., Hahn, S., Kidd, R., Melzer, T., Bartalis, Z., Hasenauer, S., Figa-Saldana, J., de Rosnay, P., Jann, A., Schneider, S., Komma, J., Kubu, G., Brugger, K., Aubrecht, C., Zueger, J., Gangkofner, U., Kienberger, S., Brocca, L., Wang, Y., Boeschl, G., Eitzinger, J., Steinnocher, K., Zeil, P., and Rubel, F. (2013). The ascat soil moisture product: A review of its specifications, validation results, and emerging applications. *Meteorologische Zeitschrift*, 22(1):5–33.
- Wagner, W., Lemoine, G., Borgeaud, M., and Rott, H. (1999a). A study of vegetation cover effects on ERS scatterometer data. *IEEE Transactions on Geoscience and Remote Sensing*, 37(2):938–948.
- Wagner, W., Lemoine, G., and Rott, H. (1999b). A method for estimating soil moisture from ERS scatterometer and soil data. *Remote sensing of environment*, 70(2):191–207.
- Wanders, N., Karssenberg, D., Roo, A. d., De Jong, S. M., and Bierkens, M. F. P. (2014). The suitability of remotely sensed soil moisture for improving operational flood forecasting. *Hydrology and Earth System Sciences*, 18(6):2343–2357.
- Wang, J., O'Neill, P., Jackson, T., and Engman, E. T. (1983). Multifrequency Measurements of the Effects of Soil Moisture, Soil Texture, And Surface Roughness. *IEEE Transactions on Geoscience and Remote Sensing*, GE-21(1):44–51.
- Wang, J. R. and Schmugge, T. J. (1980a). An empirical model for the complex dielectric permittivity of soils as a function of water content. *Geoscience and Remote Sensing, IEEE Transactions on*, GE-18(4):288–295.

- Wang, J. R. and Schmugge, T. J. (1980b). An empirical model for the complex dielectric permittivity of soils as a function of water content. *IEEE Transactions on Geoscience and Remote Sensing*, GE-18(4):288–295.
- Wang, Y., Day, J. L., Davis, F. W., and Melack, J. M. (1993). Modeling L-band radar backscatter of Alaskan boreal forest. *Geoscience and Remote Sensing, IEEE Transactions on*, 31(6):1146–1154.
- Wegmuller, U. and Werner, C. (1997). Retrieval of vegetation parameters with SAR interferometry. *IEEE Transactions on Geoscience and Remote Sensing*, 35(1):18–24.
- White, M. A., Thornton, P. E., and Running, S. W. (1997). A continental phenology model for monitoring vegetation responses to interannual climatic variability. *Global biogeochemical cycles*, 11(2):217–234.
- Woodhouse, I. H. (2005). *Introduction to microwave remote sensing*. CRC press.
- Woodhouse, I. H. and Hoekman, D. H. (2000). A model-based determination of soil moisture trends in Spain with the ERS-scatterometer. *IEEE transactions on geoscience and remote sensing*, 38(4):1783–1793.
- Wright, W. J. (1997). Tropical–extratropical cloudbands and Australian rainfall: I. climatology. *International Journal of Climatology*, 17(8):807–829.
- Yang, F., Yang, J., Wang, J., and Zhu, Y. (2015). Assessment and validation of MODIS and GEOV1 LAI with ground-measured data and an analysis of the effect of residential area in mixed pixel. *IEEE Journal of Selected Topics in Applied Earth Observations and Remote Sensing*, 8(2):763–774.
- Álvarez Mozos, J., Verhoest, N. E., Larranaga, A., Casali, J., and Gonzalez-Audicana, M. (2009). Influence of Surface Roughness Spatial Variability and Temporal Dynamics on the Retrieval of Soil Moisture from SAR Observations. *Sensors (Basel, Switzerland)*, 9(1):463–489.